Algorithms for efficient and quantitative non-destructive testing by pulsed thermography

Dissertation

zur Erlangung des Grades
des Doktors der Ingenieurwissenschaften
der Naturwissenschaftlich-Technischen Fakultät III
der Universität des Saarlandes

von
M.Sc. Sergey Lugin

Saarbrücken 2007

Dekan: Prof. Dr. Uli Müller

Erstgutachter: Prof. Dr. Michael Kröning

Zweitgutachter: Prof. Dr. Wolfgang J. Paul

Tag des Kolloquiums: 30.10.2007

I declare in lieu of an oath that this dissertation was done by myself using only literature cited at the end of this volume.

Sergey Lugin

Kurzzusammenfassung

Das Hauptziel dieser Dissertation ist die Rekonstruktion von Defekten aus thermographischen Daten bei der Pulsthermographie (PT). Das Problem der Datenkomprimierung wird ebenfalls betrachtet.

Die Rekonstruktion der Fehlerform aus Pulsthermographiedaten ist ein schlecht gestelltes inverses Problem. Die existierenden Algorithmen sind nur im Fall idealer Fehler anwendbar. In dieser Arbeit wird ein neuer Rekonstruktionsalgorithmus vorgeschlagen. Das entwickelte Verfahren kombiniert das Prinzip der thermischen Pulsreflektion im eindimensionalen Bereich mit der numerischen Simulation des PT Experiments. Der Algorithmus kann für eine große Klasse von Fehlern eingesetzt werden. Die experimentelle Rekonstruktion eines Fehlerprofils in einer Stahlprobe wird beschrieben.

In dieser Arbeit wird außerdem das Problem der Datenkomprimierung bei der PT betrachtet. Verlustbehaftete und verlustfreie Verfahren werden vorgeschlagen. Beide Methoden basieren auf einer Vorverarbeitung der Daten und Anwendung existierender Komprimierungsalgorithmen. Im Fall der verlustbehafteten Methode wurde JPEG2000 und im verlustfreien Fall ZIP eingesetzt. Die Vorverarbeitung transformiert jeweils die Daten gemäß dem spezifischen Informationsgehalt der PT, so dass die Komprimierungsrate erhöht wird. Ein Vergleich mit anderen Komprimierungs-algorithmen wird durchgeführt.

Short abstract

This dissertation is devoted to pulsed thermography (PT). The main research topic is reconstruction of defect shape from thermographic data. The data compression problem is also considered.

The reconstruction of the defect shape from pulsed thermography data is an ill-posed inverse problem. The existing algorithms are applicable only for ideal defect cases. In this work a new defect shape reconstruction algorithm is proposed. The developed algorithm combines the principle of the thermal pulse reflection in the one-dimensional domain with the numerical simulation of the PT experiment. The algorithm can be applied for wide classes of defects. The experimental reconstruction of the corrosion profile in a steel sample by the developed algorithm is presented.

In this work the problem of data compression in PT is discussed. Lossy and lossless methods are proposed. Both methods are based on pre-processing the data and application of existing compression algorithms, an image compression algorithm (JPEG2000) for the lossy method and a lossless compression algorithm (ZIP) for the lossless method. In each case the pre-processing transforms the data based on the specific information content of PT that, in consequence, increases the compression ratio. A comparison with other compression algorithms is presented.

Zusammenfassung

Das Hauptziel dieser Dissertation ist die Rekonstruktion von Defekten aus thermographischen Daten bei der Pulsthermographie (PT). Das Problem der Datenkomprimierung wird ebenfalls betrachtet.

Die Rekonstruktion der Fehlerform aus Pulsthermographiedaten ist ein schlecht gestelltes inverses Problem. Die existierenden Algorithmen sind nur im Fall idealer Fehler anwendbar. In dieser Arbeit wird ein neuer Rekonstruktionsalgorithmus vorgeschlagen. Dieser kann für eine große Klasse von Fehlern eingesetzt werden. Die experimentelle Rekonstruktion eines Fehlerprofils in einer Stahlprobe wird beschrieben.

Das entwickelte Verfahren kombiniert das Prinzip der thermischen Pulsreflektion im eindimensionalen Bereich mit der numerischen Simulation des PT Experiments. Dazu wird ein Modell der untersuchten Probe mit einem bestimmten (rekonstruierten) Fehler erstellt, so dass dessen Simulation bei Test mit PT die gleiche thermische Antwort ergibt wie die Messung. Es wird angenommen, dass die thermischen Eigenschaften und die geometrischen Größen der untersuchten Probe bekannt sind.

Der Algorithmus funktioniert wie folgt: Zuerst wird die Fehlerform näherungsweise aus der Messung gewonnen, indem eine eindimensionale Methode der Fehlertiefenabschätzung benutzt wird. Dann wird ein PT-Experiment basierend auf dem erstellten Fehlermodell simuliert. Diese Simulation erlaubt es, den Einfluss der lateralen Wärmeflüsse zu bewerten, die durch die Fehlerform induziert werden. Durch Vergleich der simulierten thermischen Fehlerantwort mit der gemessenen thermischen Fehlerantwort korrigiert der Algorithmus den rekonstruierten Fehler und nähert ihn der tatsächlichen Form in der untersuchten Probe an. Dieser Vorgang (Simulation und Korrektur) wird iterativ wiederholt. Nach wenigen Iterationen wird die tatsächliche Fehlerform mit akzeptabler Genauigkeit rekonstruiert. Der Algorithmus wurde in Simulation und im Experiment getestet. Stabile Resultate wurden erreicht.

In dieser Arbeit wird außerdem das Problem der Datenkomprimierung bei der PT betrachtet. Verlustbehaftete und verlustfreie Verfahren werden vorgeschlagen. Beide Methoden basieren auf einer Vorverarbeitung der Daten und Anwendung existierender Komprimierungsalgorithmen. Im Fall der verlustbehafteten Methode wurde JPEG2000 und im verlustfreien Fall ZIP eingesetzt. Die Vorverarbeitung transformiert jeweils die Daten gemäß dem spezifischen Informationsgehalt der PT, so dass die Komprimierungsrate erhöht wird. Ein Vergleich mit anderen Komprimierungs-algorithmen wird durchgeführt.

Abstract

This dissertation is devoted to pulsed thermography (PT). The main research topic is reconstruction of defect shape from thermographic data. The data compression problem is also considered.

The reconstruction of the defect shape from pulsed thermography data is an ill-posed inverse problem. The existing algorithms are applicable only for ideal defect cases. In this work a new defect shape reconstruction algorithm is proposed. The algorithm can be applied for wide classes of defects. The experimental reconstruction of the corrosion profile in a steel sample by the developed algorithm is presented.

The developed algorithm combines the principle of the thermal pulse reflection in the one-dimensional domain with the numerical simulation of the PT experiment. The main idea used in the reconstruction is creating a model of the inspected sample with a certain (reconstructed) defect shape so that its simulation under PT testing will give the thermal response equal to the measurement. It is assumed that thermal properties and geometrical sizes of the inspected sample are known.

The algorithm operates as follows: Initially, the defect shape is extracted approximately from the measurement using a one-dimensional defect depth retrieval technique. Then a pulsed thermography testing experiment is simulated based on the sample model with the extracted defect shape. The simulation allows the evaluation of the influences of lateral thermal flows induced by the extracted shape. By comparing the simulated thermal defect response with the measurement defect response the developed algorithm corrects the reconstructed shape approaching it to the actual defect shape in the inspected sample. This process (simulation and correction) continues iteratively. In a few iterations the algorithm reconstructs the actual defect shape with satisfactory precision. The algorithm was tested in the simulation and experimental mode. Robust reconstruction results were obtained.

In this work the problem of data compression in PT is discussed. Lossy and lossless methods are proposed. Both methods are based on pre-processing the data and application of existing compression algorithms, an image compression algorithm (JPEG2000) for the lossy method and a lossless compression algorithm (ZIP) for the lossless method. In each case the pre-processing transforms the data based on the specific information content of PT that, in consequence, increases the compression ratio. A comparison with other compression algorithms is presented.

Acknowledgments

Contents

Chapter 1

Introduction

Global production of all industrial goods increases from year to year. At the same time there is an ever increasing demand for higher quality products, both from a regulatory stand point and based on the requirements of the consumer. There is a general trend to inspect products at early manufacturing stages reducing costs for replacing poor-quality work later. This trend contributes to the recent growth of non-destructive testing methods. Basically, non-destructive testing (NDT) [1-3] is utilized for two purposes: quality control and maintenance. While more and more complex machineries such as cars, planes and trains are used in the world, maintenance of them becomes an important issue. In many cases, machinery elements operate under extreme mechanical and thermal conditions. Due to this, the elements are prone to damage, cracks, corrosion and defects that can affect their functionality. The functionality of single elements constitutes the reliability and safety of the whole machinery. In some cases, a failure of single elements in turbines, wheels, welded parts, etc., leads to a fatal machinery crash. Since the reliability and safety are primary concerns, these elements are inspected regularly using NDT methods.

1.1 Infrared thermography

Non-destructive testing involves a variety of techniques: ultrasonic testing, radiographic testing, magnetic particle testing, visual testing, dye penetrant testing, acoustic testing, electromagnetic testing, infrared testing and leak testing. The methods have preferable application fields, limitations, advantages and disadvantages. In this work we consider infrared testing also known as *infrared thermography* [4-9]. The name contains the prefix *thermo-* that means the temperature and the suffix *-graphy* that implies writing. The measurement of temperature distribution and its analysis are the main factors involved in infrared thermography.

Infrared thermography involves *passive* and *active* procedures. In the first case, the test object releases heat consumed at the production stage. Observing and analysing the cooling process, it is possible to reveal defective areas which are detectable due to the presence of thermal anomalies. For instance, the passive thermography procedure is used in industry applications that incorporate welded metal joints. In active thermography the test object is heated up by an external source. The presence of a

significant temperature difference pinpoints subsurface anomalies. In general, active thermography includes *pulsed thermography* (PT), *step heating thermography* (SH), *lock-in thermography* (LT) and *vibrothermography* (VT). These are briefly described in the following paragraphs:

In pulsed thermography the test sample is heated up for a short period of time. This heating produces a thermal pulse that propagates into the sample by thermal diffusion. During the pulse propagation an infrared camera is used to record temperature distribution on the sample surface. A subsurface defect, if present, modifies the diffusion heat flow so its location appears as an area with a temperature difference with respect to the surrounding area.

In step heating the sample is constantly heated starting at a certain point of time. During the heating the temperature evolution is observed.

In lock-in thermography the sample is heated up periodically, generating thermal waves inside. For instance, a sine-modulated heating can be used. The resulting temperature response is recorded and is used for computation of phase and magnitude images.

Vibrothermography is based on an effect of direct conversion from mechanical to thermal energy. The inspected sample is subjected to mechanical excitation that causes a friction effect in places where the defects (delamination, cracks, etc.) are located. Due to friction, a certain amount of energy is released, pinpointing the defect location.

Considering these four methods of active thermography one can note that they are similar in some aspects and at the same time they are different and used for specific purposes. This work focuses on methods of defect characterization and data compression for pulsed thermography and proposes new approaches for solving these problems.

1.2 Problem statement

In this work two problems are considered. The first problem is a reconstruction of the shape of a subsurface defect. Figure 1.1 illustrates the given problem schematically in the two-dimensional case.
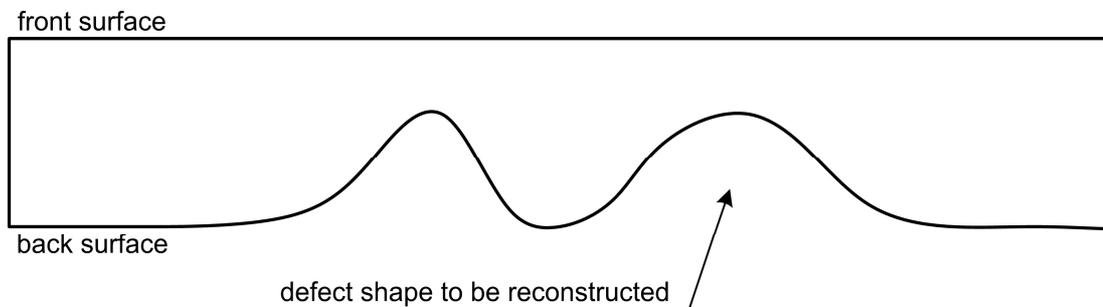
Figure 1.1: Sample with the defect shape to be reconstructed.

According to the methodology of pulsed thermography testing, the front surface of the inspected sample is excited briefly and its cooling process is observed and recorded by an infrared (IR) camera. The first aim of the study in this work is to develop an algorithm which reconstructs the defect shape from the measured cooling thermal image sequence. It is an ill-posed nonlinear inverse problem [10] as the solution (the defect shape to be reconstructed) is not unique in many cases. Note also that this problem is relevant in NDT. For example, in the aerospace industry the algorithm can be used to determine corrosion profiles of the skin of an aircraft [11]. It can be also used to determine the residual thickness of the cooling channel of a turbine rotor blade [12]. In brief, the algorithm is applicable in almost any inspection where the subsurface defect depth or shape is of interest.

The second problem is efficient data compression. As it was mentioned above, during the inspection the infrared camera scans the front surface of the sample, recording an image sequence that represents the thermal distribution of the inspected surface as a function of time. A typical sequence includes 100-400 images (frames) and requires a significant amount of storage space in raw format. On the one hand, the measured sequence should be traceable, on the other hand, excessive data storage volume as it might occur in 24 h process control applications has to be avoided. The second aim in this work is to develop a method that will efficiently compress the data measured by PT.

These two problems lie in the background of the studies carried out in this work.

1.3 Previous and related work

The first problem, namely, the reconstruction of the defect shape, has the aim of determining the depth of a defect in all points where the defect spreads. Note that most of the literature regarding PT concern a particular case where the defect is a flat bottom hole and the target values are the hole depth and the hole diameter. Authors in [13] showed that the time at the point, when the temperature contrast begins to rise, is proportional to the square of the hole depth and is independent of the hole diameter. Authors in [14] suggest to transform the cooling curve to the double-logarithmic domain. The solution for the surface temperature of a one-dimensional heat diffusion equation for a defect-free, surface absorbing half-space sample is a straight line in the log-domain. Any deviations from the straight line give evidence of the presence of the defect. The square of the defect depth is proportional to the time where the deviation begins. To find the hole diameter, the authors in [13,15] suggest to measure a full-width at half maximum (FWHM) contrast measurements of the defect image diameter. Other research work [16] offers a method that permits the elimination of the lateral diffusion scattering effect in the case of planar defects. Another approach uses multi-dimensional linear regression [17] for the flat bottom hole characterization.

The problem of the defect shape extraction for a general defect shape without much a priori information has not been the subject of wide discussion. It is caused by the fact that the thermal diffusion process introduces strong "smearing" and "damping"

which complicate the analysis of the defect temperature response. Only a single research work [10] describes the extraction of the defect shape from the viewpoint of applied mathematics and proposes a solution of the ill-posed problem for a particular case when the test sample has constant thermal diffusivity. Here we present a new solution for this more general problem and show for the first time reconstruction results based on experimental data.

The second problem, namely, compression of the cooling image sequence was originally considered in [18,19]. Basically, the main idea of the proposed time signal reconstruction (TSR) method lies in a transformation of the cooling curve in the logarithmic domain and its approximation by a polynomial. The TSR method has some advantages, but also disadvantages. The main advantage is low storage cost that is independent of the number of images in the sequence. The main disadvantage is that the cooling sequence can have a certain time related behaviour which can not be approximated with satisfactory accuracy by a polynomial. So other approaches for pulsed thermography data compression are proposed.

1.4 Outline of the thesis

The present thesis is organized as follows: In Chapter 2, the fundamentals of pulsed thermography are presented. Chapter 3 covers the main existing defect detection and characterization methods used in PT. Chapter 4 is devoted to basics of heat transfer and gives a review on numerical methods that are utilized for heat transfer simulations. In Chapter 5 we present the developed defect shape reconstruction algorithm. The reconstructions under simulated and experimental conditions are presented and discussed. Chapter 6 describes new approaches for compression of the cooling image sequence. The results of compression by proposed and existing methods are compared. In Chapter 7 we conclude and discuss future work. The bibliographical references that were used are listed in the end of the document. In Appendixes a list of the symbols, abbreviations and photos/sketches of the samples and the measurement setup are given.

Chapter 2

Pulsed thermography

In this chapter, pulsed thermography testing is introduced. Potential variants of the measurement setup for PT are discussed. A typical infrared image sequence measured by PT is presented.

2.1 Testing methodology

Pulsed thermography is a non-destructive thermal stimulation method frequently used in thermal non-destructive testing (TNDT). The method has received recognition and experienced wide application due to the following criteria: contact-free operation, capability to inspect large areas simultaneously and speed of inspection. This kind of testing allows for the detection of subsurface defects, inclusions and delaminations as well as for material characterization [4]. Figure 2.1 shows an experimental setup for PT schematically. The setup consists of heat sources, an infrared (IR) camera and a personal computer (PC).
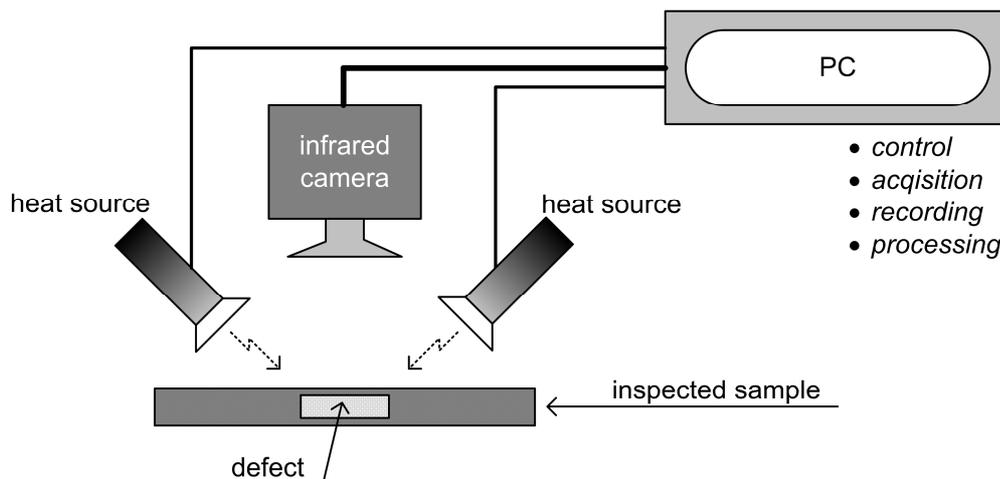
Figure 2.1: Pulsed thermography experimental setup.

As a method of active thermography, pulsed thermography is based on the thermal stimulation of the inspected sample and the analysis of its thermal response. The inspection usually includes three phases:

1) thermal excitation
2) observation of thermal response
3) data analysis

The phases are characterized as follows:

➢ ***Phase: thermal excitation***
The front surface of the inspected sample under test is uniformly heated up for a short period of time. The heating lasts from a few milliseconds for high thermal conductivity material to a few seconds for low conductivity material. A typical heating source is a high-power flashlight.

➢ ***Phase: observation of thermal response***
The thermal pulse, which is delivered in the first phase, propagates into the inspected sample and is reflected by inclusions or material thermal property changes which the sample might contain. During the propagation of the excited pulse, the infrared (IR) camera scans the front surface, recording an image sequence that represents the thermal distribution of the inspected surface as a function of time. A typical sequence includes 100-400 images.

➢ ***Phase: data analysis***
The image sequence is analysed in order to extract defect shapes, defect depths, coating or wall thickness. In brief, the analysis can be explained as follows. Defects, inclusions or delaminations change thermal properties at their locations. While propagating the thermal pulse, the rates of temperature decay in defect and defect-free areas on the sample surface are different. This temperature difference indicates the presence of subsurface defects.

The described setup is the most common variant of a reflective pulsed thermography setup with surface heating. Indeed, pulsed thermography offers a variety of experimental solutions. They are classified by the type of thermal stimulation and by observation methods [4]. To be precise, the thermal stimulation can be heating or cooling. The diversity of the heating methods is presented in Figure 2.2. The major heating methods are: a) point heating (using a laser beam or focused arc lamp), b) line heating (using a line infrared lamp, heated wire), c) surface heating (using flash lamps, cinematographic spots, incandescent bulbs). The latter technique is most popular in PT as it allows the inspection of large areas in a short period of time. The method has the drawback that results in a non-uniform (also called "uneven") heating effect. The choice of the heating method in any PT measurement setup depends on the testing problem. The heating source can operate in pulsed as well as in continuous mode. Continuous heating requires the movement of the sample or the source. As a precaution it should be

noted that during thermal stimulation, the process of excitation and its duration must not damage the inspected sample.
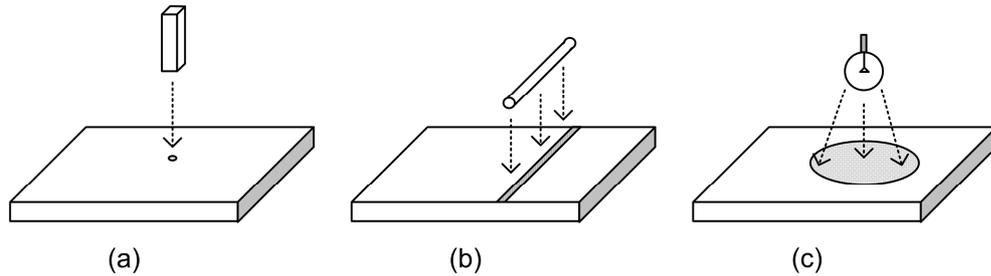
Figure 2.2: Heating methods in PT:
(a) – point heating, (b) – line heating, (c) – surface heating.

PT offers two methods of observation: thermal reflection and thermal transmission. In the thermal reflection method, both the heat source and the infrared camera are placed on the same side, towards the front surface of the inspected sample (Figure 2.3(a)). In the transmission method, the infrared camera is placed on the opposite side to the heat source as shown in Figure 2.3(b).
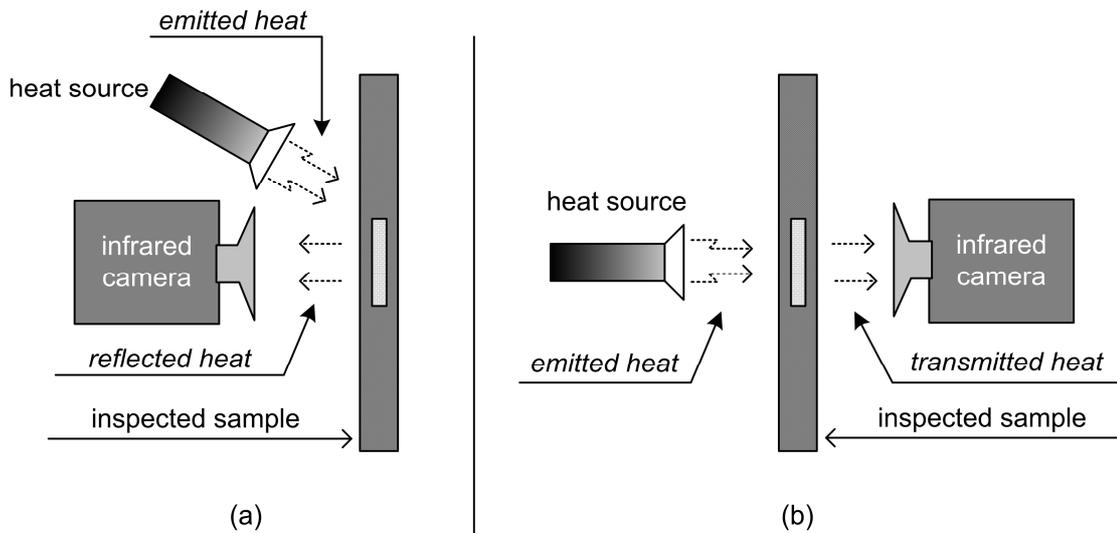
Figure 2.3: Observation methods in PT:
(a) – thermal reflection method, (b) – thermal transmission method.

Each method of observation has its advantages and disadvantages. The reflective observation method is a single-side inspection and provides high resolution but only shallow defects can be revealed. The transmission method needs accessibility to the back surface. It has a lateral resolution lower than the reflection method. The method allows the detection of shallow as well as deep defects but does not provide defect depth information. Since in many cases the back side is inaccessible, the reflective observation method is used more often. In this work we focus on algorithms of defect detection and characterization for the thermal reflection method with surface heating.

2.2 Equipment and laboratory conditions

Some aspects of pulsed thermography experiments need special consideration. First we deal with equipment and then with laboratory conditions.

As it was described before, the equipment used in pulsed thermography consists of a heat source, an infrared camera and a computer controlling the measurement process. In many cases the heat sources are flash lamps. In a short period of time (5-10 milliseconds) the lamps illuminate the sample surface releasing a huge amount of heat energy. If only a single lamp is used in the measurement setup, it causes strong uneven heating, an undesirable effect. This is due to the variable distance from the lamp emitter to the points on the sample surface. Without further normalization steps, this effect makes the analysis of the temperature response more difficult because at the beginning the surface points have different temperatures. According to testing methodology in PT, the inspected sample surface should be heated uniformly. For this purpose, a double or multiple flash lamp system (see Figure 2.4) with lamps arranged symmetrically with respect to the IR camera, is preferable as it permits both an increase and homogenization of the excitation power density over the sample surface.
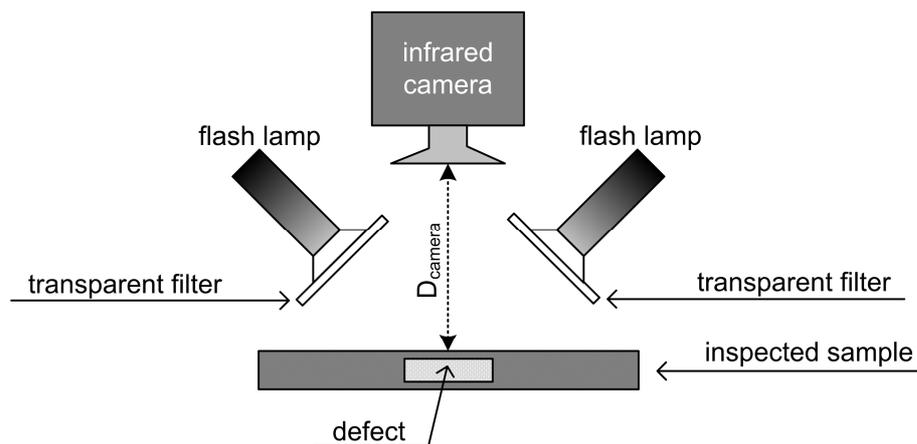
Figure 2.4: Pulsed thermography setup arrangement.

Flash lamps differ concerning their heat radiation elements and their constructions [4]. Lamps with an open air emitter need additional transparent filters mounted as shown in Figure 2.4. The filter is utilized to retain the infrared radiation coming from the hot shell of the lamp emitter after the excitation. This radiation is undesirable as it can be reflected from the sample surface and surrounding objects into the camera lens affecting the thermal image.

As most of the test objects are not transparent to the thermal infrared, in the PT measurement setup the camera captures the infrared image of the front surface of the sample. Independent of its optics and detector type, each camera is characterized by four main parameters: pixel resolution, frame rate, temperature dynamics and sensitivity. The camera resolution is defined as the number of pixels in horizontal and vertical direction used to digitize the observation camera view. Presently, commercially available infrared cameras have resolutions of up to 640x512 pixels. The acquisition

rate specifies the speed at which the infrared image can be taken. This rate is ultimately limited by the camera exposure time, but also by the detector and its read-out technology. In many cases, where highly conductive samples are inspected, the acquisition rate is of great importance as only high speed cameras permit the observation of the fast transient thermal flows. Today, a camera with 5 ms acquisition rate is regarded as a fast camera. The camera primarily measures the radiation power in the infrared spectrum, rather than exact temperature values. Each pixel of the captured infrared image is represented by an unsigned integer value (or "infrared value"). This value can be converted to the exact temperature value using a camera specific temperature calibration curve, which can be obtained using a black emitter device. The range in which the IR value can lie is defined by a digitalization level. Most cameras used in TNDT have the digitalization of the work temperature range from 14 to 16 bits. The lowest/highest IR value corresponds to lowest/highest temperature the camera is capable of measuring. The camera sensitivity is the lowest temperature change detectable by the camera, defined by the noise equivalent temperature difference (NETD). Modern cameras have a sensitivity of about 5-15 mK. The camera sensitivity is different across the temperature range. Usually the camera has the highest sensitivity in the middle of the work temperature range. Atmospheric absorption of radiation is important for longer distances between the camera and test object. Therefore, in the PT measurement setup it is recommended to locate the IR camera at a distance less than 1 m (see D_{camera} in Figure 2.4), as the air absorbs infrared radiation that eventually blurs the infrared image.

In PT testing the state of the inspected sample is also of importance. In many cases the sample to be inspected has to be prepared for testing. This is due to the absorption and emission properties. The perfect absorber and perfect radiator is a black body. In PT the inspected sample absorbs energy during the thermal excitation phase and radiates energy during the observation phase. If the sample is made of ground steel or aluminium, it is a bad absorber and a bad radiator. The common way to overcome both problems is to coat the inspected sample with a thin black paint layer. This problem is discussed in detail in Section 4.5.

2.3 Data acquisition

The main control parameters in any measurement are energy of excitation, total observation time of the cooling process and the number of thermal images to be taken. The excitation energy is a variable parameter of the heat source. The total observation time and the number of images are control settings of the camera. The observation time has to cover the main part of the cooling process. We use the term *main part*, as the cooling process, strictly speaking, continues until the whole sample has reached the ambient temperature, but only the beginning of the cooling is of interest in PT. For example, the cooling process in a polyvinylchloride (PVC) sample is extremely slow, due to the poor thermal conductivity. Typical observation times are about 30 seconds. In the case of an aluminium sample, the cooling process after 1 second is almost over.

Thus the total observation time and the number of images are set individually according to thermal sample properties and initial tasks. As an illustration, some images of the cooling image sequence of a polyethylene sample with 4 flat bottom holes are shown in Figure 2.6. The sketch of the inspected sample is depicted in Figure 2.5.
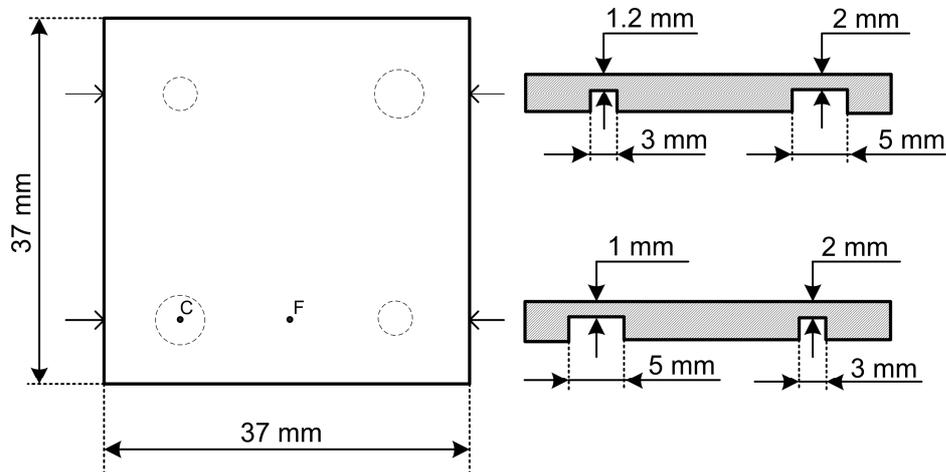
Figure 2.5: Sketch of the inspected sample with 4 flat bottom holes.

As can be seen, the defects, namely, flat bottom holes, appear as hot spots. The temperature above the holes is higher than in the neighbourhood. The shallow holes appear at first and the deep holes become visible later. The unique feature that helps precisely to recognise a defect is the difference of temperature between the defect and defect-free areas. Surface temperature evolution curves over the hole centre (C) and away from it (F) are shown in Figure 2.7. These curves are called cooling curves as they describe the cooling process. As the time passes, due to thermal diffusion in all directions, the temperature on the sample surface trends towards the equilibrium again.
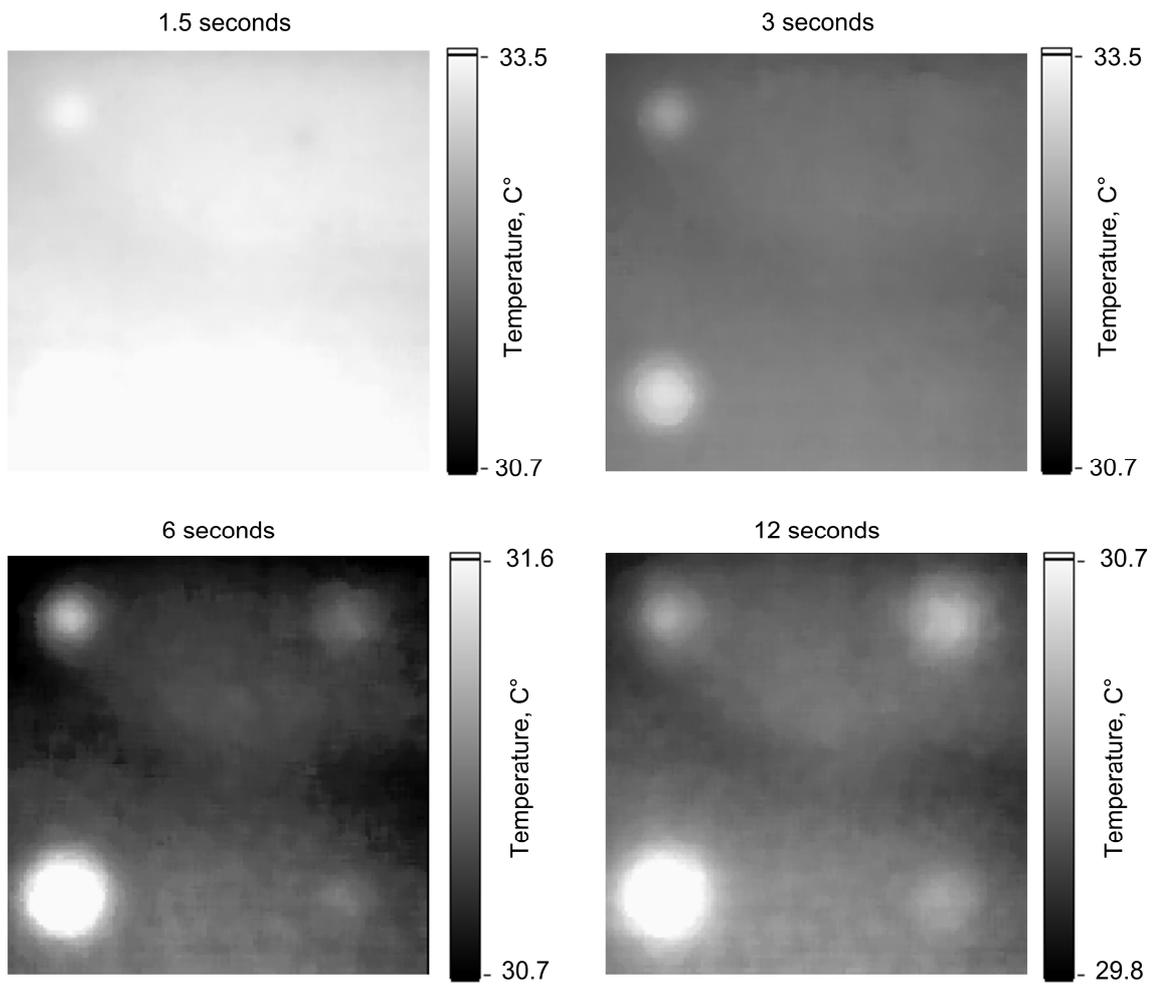
Figure 2.6: Images of the cooling sequence measured by PT.
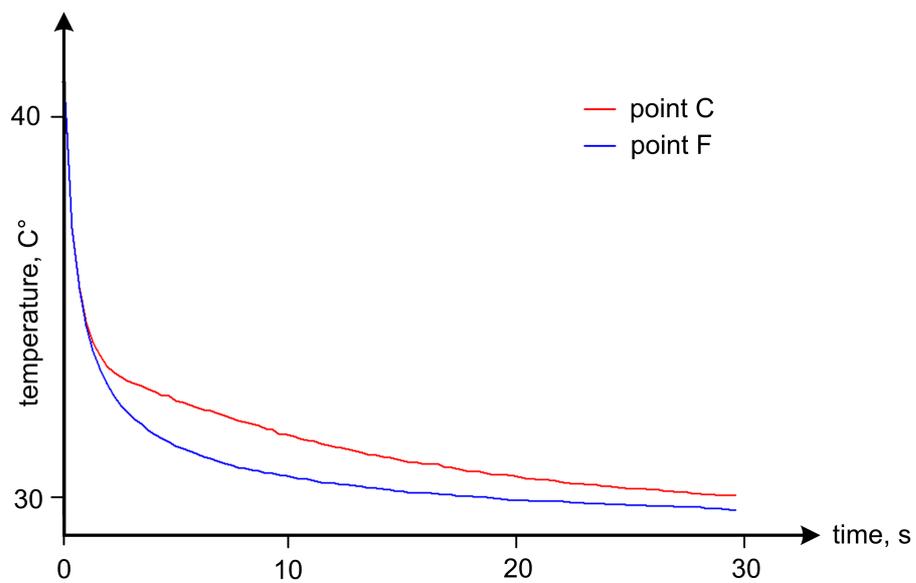
Figure 2.7: Cooling curves at the hole centre and apart from it
(cooling curves are extracted at the points C and F as shown in Figure 2.5).

The noticeable temperature difference indicates the presence of a defect and pinpoints its location. Thus, we can conclude that the qualitative aspect of non-destructive inspection is not a problem in PT. More challenging is a quantitative evaluation of the inspection results: exact shape, depth and thermal properties. In Chapter 3 we present the main existing methods of defect detection and characterization used in PT.

2.4 Application

Like every non-destructive testing method, pulsed thermography has preferable fields of application. A wide survey of applications is presented in [4]. Basically, pulsed thermography is applied for detection and characterization of subsurface defects and anomalies. Particularly, this technique is used for inspection of turbine blades [20-23], corrosion characterization [11,19,24-29], defect detection [13,19,30-41]. Pulsed thermography is applied for revealing delaminations (disbonding) in composite materials [11,32,42-45], coating [46,47] and also in frescos of buildings. This technique is used for inspection of welds, detection of unwanted phases (cementite) in cast iron [48], characterization of the porosity of ceramic coatings. Thanks to advancements in the technology of IR cameras, computers and processing algorithms, new application fields of pulsed thermography in TNDT are constantly emerging.

Chapter 3

Defect detection and characterization

In this chapter a survey on defect detection and characterization methods is presented. The described methods constitute a fundamental basis in PT. The problem of defect detection and characterization in PT is constantly discussed and studied. New methods are constantly emerging.

3.1 Thermal flows

Once the sample has been excited, the generated subsurface thermal pulse begins to propagate in the sample medium due to the thermal gradient. The thermal pulse flows from the front surface to the back surface and causes the temperature to decay on the front surface of the sample. The sketch of the thermal flows in the inspected sample is shown in Figure 3.1. If any defect, inclusion, corrosion or delamination is present, it modifies the thermal properties in its location and acts as a thermal barrier (or a trap). The difference between damages, inclusions, defects and other faults in this case is slight. From the heat propagation point of view the damage, inclusion or corrosion is a medium with thermal properties different from the sample thermal properties. For simplicity of the description in this work we call them *defects* as their influence on the heat propagation is similar.
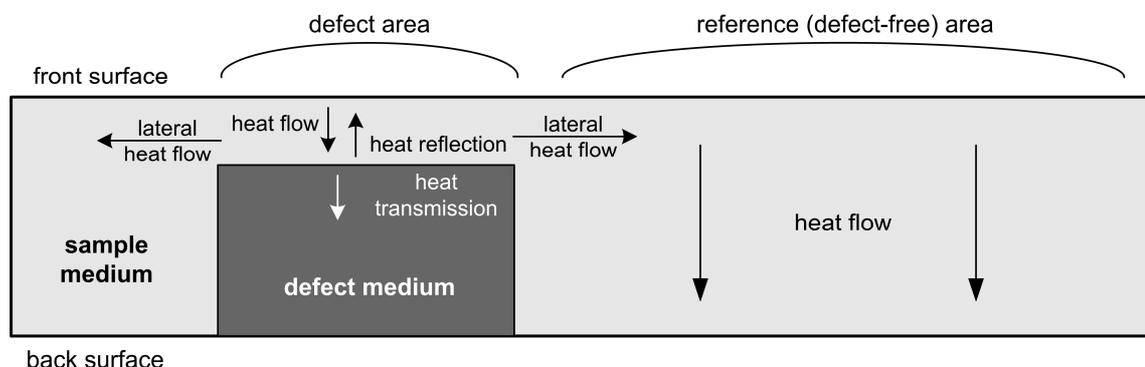
Figure 3.1: Sketch of thermal flows in the inspected sample.

The propagation of the excited pulse is governed by thermal diffusion. When the thermal pulse reaches the defect location, the rate of the diffusion flow is changed because of the discontinuity of the thermal properties, more precisely the effusivity (see Section 3.3.1.2). Some part of heat energy is reflected and goes back to the front surface and the remaining energy is transmitted into the defect medium. The sketch of the thermal distribution on the front surface of the sample when the reflected part of heat energy reaches the sample surface is depicted in Figure 3.2.
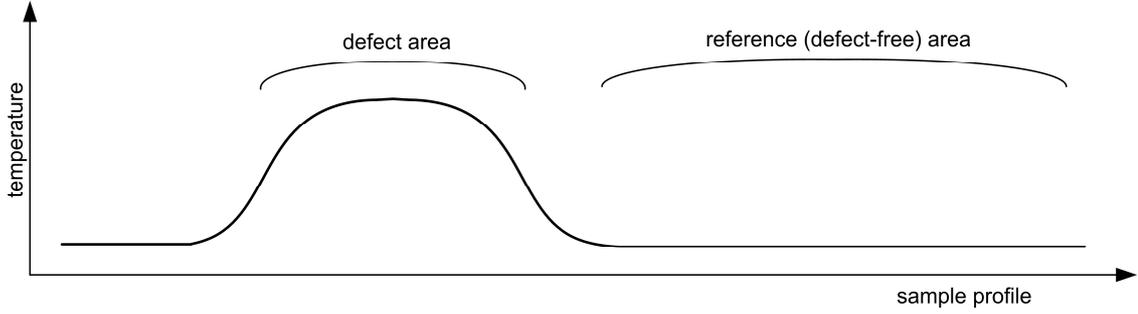
Figure 3.2: Thermal distribution on the front surface of the sample
(the defect causes overheating at its location).

The fractions of heat flow reflected and transmitted at the border between sample and defect are determined by the thermal properties of the sample and the defect media. In case the surface of the defect is parallel to the surface of the inspected sample, the reflection and transmission coefficients can be computed as [4]:

$$K_{ref} = \frac{e_s - e_d}{e_s + e_d}, \qquad K_{trans} = \frac{2e_d}{e_s + e_d}, \qquad (3.1)$$

where K_{ref} is the reflection coefficient, K_{trans} is the transmission coefficient, e_s is the effusivity of the sample medium, e_d is the effusivity of the defect medium. It is worth noting that in most practical cases the defect medium is air. The reflection coefficient from most metals, alloys and polymers to air is close to 1, which means total reflection of the thermal pulse. To be precise, a similar reflection happens later in the defect-free area, but in this case the pulse is reflected from the back surface of the sample. It is a similar reflection process because the environment of the sample is often air. Moreover, when the reflected pulse portion reaches the front surface it is reflected again. The thermal reflections above the defect and the resulting confinement of heat lead to the emergence of thermal gradients in lateral directions which induce additional thermal flows (see Figure 3.1). The propagation of the thermal pulse, even in the case of a flat bottom hole, is a complex process and has not been described analytically so far. Therefore, for studying thermal processes in pulsed thermography experiments we use numerical modeling techniques.

3.2 Thermal contrast

The characterization of the defect in any PT measurement is based on the temperature difference created by the defect on the sample surface. This temperature difference is called a *thermal contrast* (also referred to as a *temperature contrast*). The thermal contrast is the thermal difference in the point to be analyzed with respect to a reference area which is assumed to be pre-selected. The reference area is considered to be the pure area where no subsurface defect is present. The selection of the reference area can be done by an operator or a certain automatic method. In most cases the reference area is a background in the thermal image and, as it is clearly seen in Figure 2.6, can be easily distinguished from the defect area. There are three main definitions of the thermal contrast [4]: *absolute contrast*, *running contrast* and *standard contrast*. They are given as follows.

The *absolute contrast $C_a(t)$* extracts an absolute difference of temperatures between the point of interest and a reference point:

$$C_a(t) = T_s(t) - T_{defect-free}(t) \; , \tag{3.2}$$

where t is the time, $T_s(t)$ is the temperature in the point of interest (suspected to be defective), $T_{defect-free}(t)$ is the temperature in the reference point (reference area). C_a is a simple and efficient measure for defect visualization. The main disadvantage of this measure is a linear dependence on the amount of energy absorbed in the excitation phase. C_a is measured in K.

The *running contrast $C_r(t)$* is the absolute contrast normalized with respect to the cooling process in the reference point:

$$C_r(t) = \frac{T_s(t) - T_{defect-free}(t)}{T_{defect-free}(t)} \; . \tag{3.3}$$

This contrast is more convenient for comparisons of experiments as it is less affected by absorbed energy and partly suppresses the influence of the surface emissivity coefficient [4]. C_r is measured in relative units.

The *standard contrast $C_{std}(t)$* is defined as:

$$C_{std}(t) = \frac{T_s(t) - T_s(t_0)}{T_{defect-free}(t) - T_{defect-free}(t_0)} \; , \tag{3.4}$$

where t_0 is a time before the thermal excitation. Subtracting the initial temperature allows the suppression of the effects of adverse radiation coming from the environment. Contrary to the running contrast, the standard contrast has a unit value in the defect-free area. C_{std} is also measured in relative units.

All thermal contrasts are different in value scales, but all of them have a similar structure which is schematically depicted in Figure 3.3. The curve has three characteristic points: the beginning point (1), the maximum point (2) and the end point (3). Real thermal contrast curves are more complex due to their dependences on lateral defect size, structure and shape of the object under inspection as shown later.
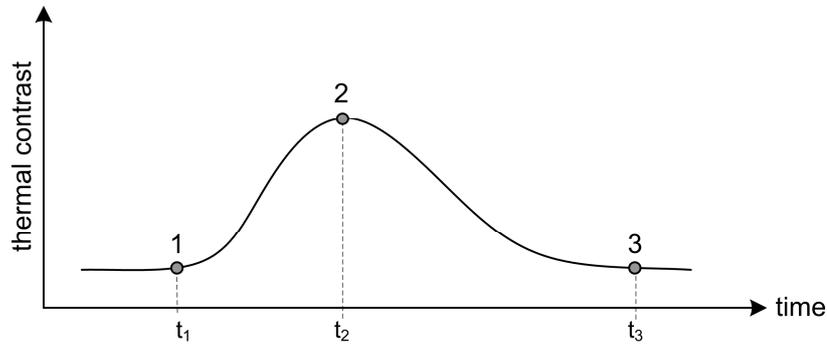
Figure 3.3: Thermal contrast curve.

It is worth pointing out that almost any analysis of the defect characteristics involves the computation of the thermal contrast. Despite the diversity of thermal contrast definitions, the absolute contrast is used more often in published studies.

3.3 Defect characterization

The defect characterization in PT has two aspects: qualitative and quantitative. As seen in Figure 2.6, the qualitative aspect is not a problem in PT. The temperature difference on the inspected sample surface, if present, pinpoints the location of the subsurface defect. The defect depth, size and shape are targets of the quantitative analysis. This section is dedicated to the description of main methods used in PT for the quantitative characterization of defects.

In most of the published literature on PT the discussed reference defect shape is a flat bottom hole [23,37,40,41,49-53 and others]. Figure 3.4 illustrates the cross section of a hole drilled into the sample. The hole diameter v_{hole} and the hole depth d_{hole} are values of interest for the inspection.
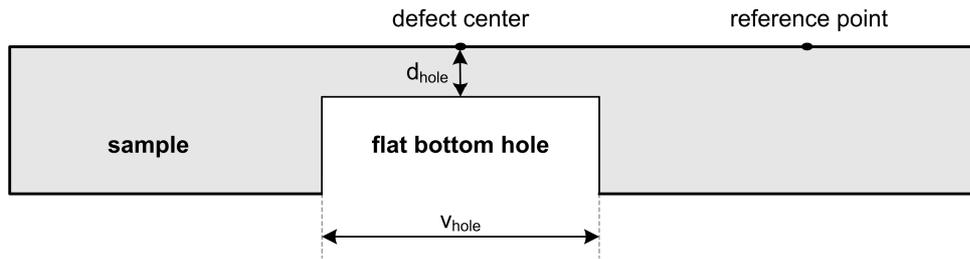
Figure 3.4: Flat bottom hole in the inspected sample.

The following sections present existing methods for extracting the defect depth and diameter from pulsed thermography data. Other methods which are applicable for more general defect classes are also considered.

3.3.1 Defect depth extraction

3.3.1.1 Thermal contrast rise

The first publications on PT proposed the evaluation of thermal contrast only. Initially, flat bottom hole defects with a certain diameter have been simulated to understand the time at which the maximum of thermal contrast appears. This dependence can be used inversely to predict the depth for an unknown hole. Because the hole diameter was assumed to be constant this method suffered significant application limits.

Subsequent investigations [13,53] improved the depth extraction method making it independent of the hole diameter. The unique feature of this method was that the time at which the thermal contrast begins to rise (point 1 in Figure 3.3) is related to the hole depth and is not affected by the hole diameter. To illustrate this, we simulated holes with diameters of 5, 7, 10 mm at depths of 1 and 2 mm in a steel sample by finite element techniques. The thermal contrast curves are depicted in Figure 3.5. They share a remarkable property, namely, the same origin points $t_{b(1)}$ and $t_{b(2)}$ at equal hole depths.
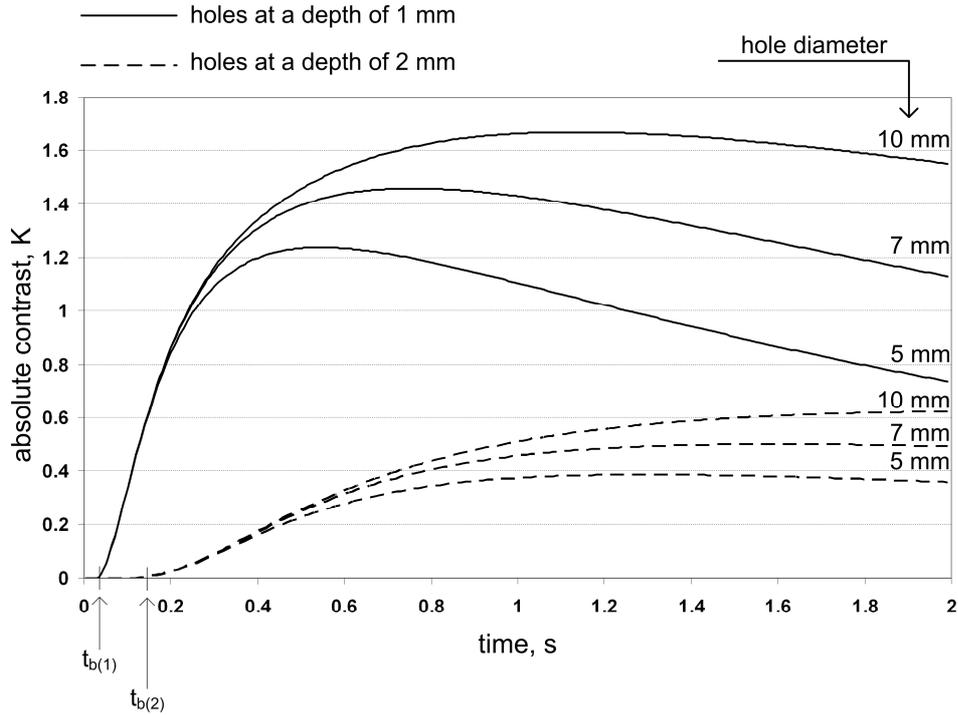
Figure 3.5: Evolution of thermal contrasts of flat bottom holes with diameters of 5, 7, 10 mm at depths of 1 and 2 mm in a steel sample.

According to theory [7,54,55], the depth at which the pulse is reflected is proportional to the square root of the time at which the reflected pulse reaches the front surface:

$$d_{hole} \approx \sqrt{4\alpha t_b} \quad , \tag{3.5}$$

where d_{hole} is the hole depth, α is the thermal diffusivity (see Section 4.2), t_b is the time at which the contrast begins to be detectable. Thus, by extracting the time when the contrast begins to rise, the hole depth can be evaluated by Equation (3.5). In the literature one can find various approaches to extract the time t_b. In [56] the authors define the time of the maximum of the thermal contrast derivative. The time is multiplied with an intermediate coefficient and serves as input in Equation (3.5). Other authors [30] propose to compute the second derivative of the thermal contrast. Then the zero crossing time is extracted from the obtained curve and substituted in Equation (3.5).

3.3.1.2 Transformation into logarithmic domain

The next method for defect depth extraction proposes the transformation of the cooling curve into the logarithmic domain [14,18,19,44]. The method is based on the following: A solution for the surface temperature $T(t)$ of a one-dimensional heat

diffusion equation for a defect-free, surface absorbing half-space sample after the Dirac pulse has the form [55]:

$$T(t) = \frac{Q}{2e_s\sqrt{\pi t}} \quad, \tag{3.6}$$

where T is the temperature on the sample surface, Q is the input energy density (also referred to as absorbed energy density and energy absorption per unit area) and e_s is the thermal effusivity of the sample. The effusivity e of a medium is defined as:

$$e = \sqrt{\lambda\rho c} \quad, \tag{3.7}$$

where λ,ρ,c are thermal conductivity, density and specific heat capacity of a medium. The transformation of Equation (3.6) into the double logarithmic domain is beneficial as the solution in this domain will represent a straight line with a slope -0.5, independently of the sample properties:

$$\ln(T(t)) = \ln\left(\frac{Q}{2e_s}\right) - \frac{1}{2}\ln(\pi t) \quad. \tag{3.8}$$

The presence of any defect causes the curve to deviate from its ideal line. This unique feature allows the detection of the defect easily, as well as the extraction of the reflection time t_b. Figure 3.6 illustrates simulated cooling curves over flat bottom holes with a diameter of 10 mm at depths of 1 and 2 mm in a steel half-space sample transformed into the logarithmic domain. The figure also shows the cooling curve in a hole-free area. It is clearly seen that at the beginning the curves belonging to the flat bottom holes are straight lines and further deviate due to reflection of the thermal pulse. The depth of the holes is evaluated by Equation (3.5).
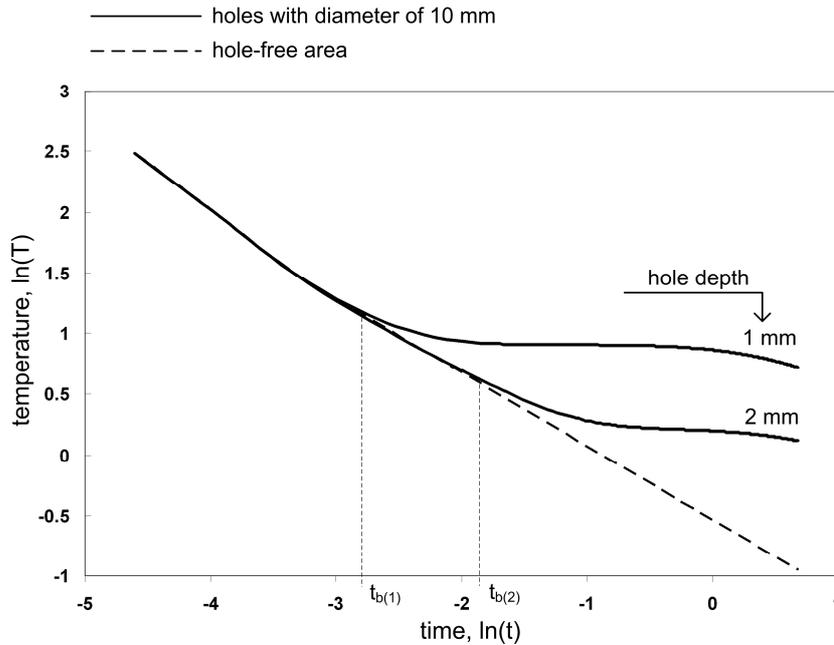
Figure 3.6: Simulated cooling curves of holes with the diameter of 10 mm at depths of 1 and 2 mm transformed into the logarithmic domain.

The representation of the cooling curve in the log-domain puts in the foreground early thermal events, making them easy to catch and analyze.

3.3.2 Defect diameter extraction

To extract the hole diameter in the pulsed thermography measurement, the authors in [13,53] suggest the measurement of the "*full width at half maximum*" (FWHM) of the thermal contrast above the defect. Figure 3.7 depicts this proposed analysis schematically. The profile x is assumed to cross the hole center (the hottest point over the defect).
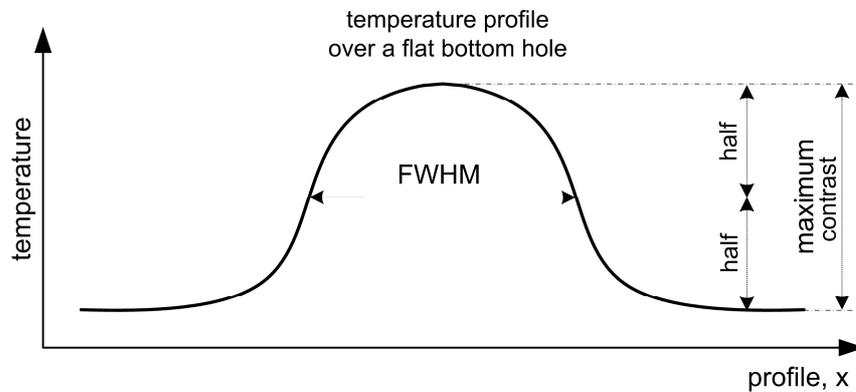
Figure 3.7: Full width at half maximum.

It has been found by many simulations and experiments that this measure is close to the real hole diameter v_{hole}. The perfect correlation is observed at early times. As the time passes, FWHM becomes a bit narrower. This phenomenon is referred to as *the shrinkage effect* [13]. Figure 3.8 illustrates the simulated behaviour of FWHM with time. For this graph we simulated flat bottom holes with the diameter of 5, 7, 10 mm at the depth of 0.5 mm in the steel sample.
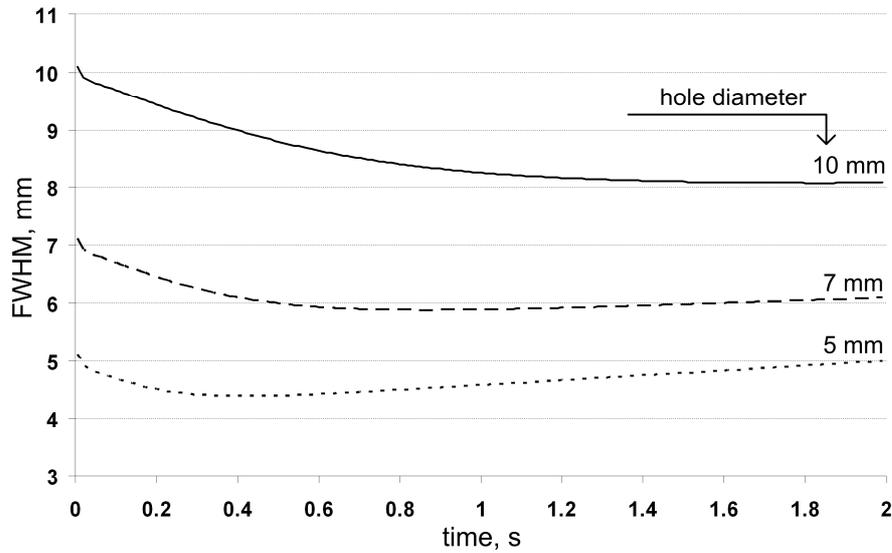
Figure 3.8: FWHM variation as a function of time
(hole defects with the diameters of 5, 7, 10 mm
at the depth of 0.5 mm in the steel sample).

It was also established that the shrinkage in FWHM varies with the hole depth. To demonstrate it, we simulated the hole with the diameter of 10 mm at the depths of 0.5, 1 and 2 mm. Figure 3.9 shows the results obtained.
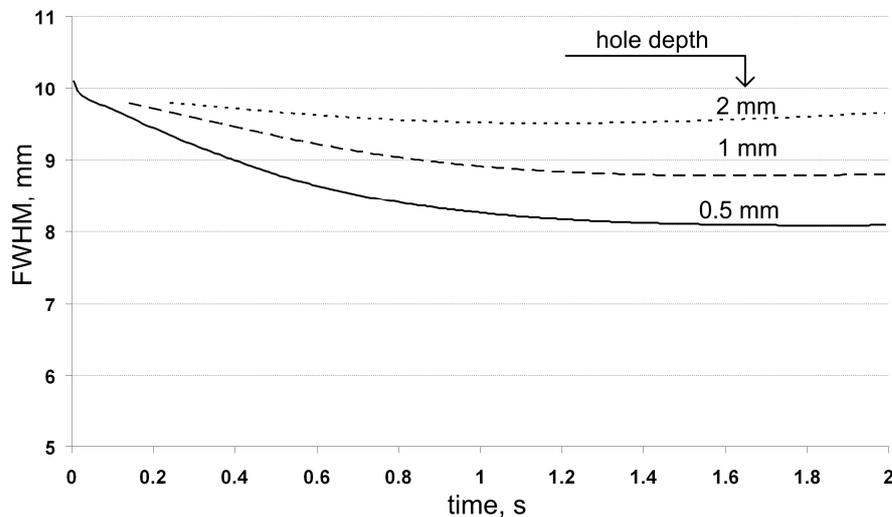
Figure 3.9: FWHM variation as a function of defect depth
(hole defects with the diameter of 10 mm at depths of 0.5, 1 and 2 mm).

Determination of FWHM from the IR image is a simple and efficient tool for extracting the defect diameter. The result varies with time and the hole depth. At early times, when the hole becomes apparent, the best correlation between FWHM and the actual hole diameter is observed (explained in Section 3.1).

3.3.3 Automatic segmentation algorithm

In some inspection cases the depth of a potential defect is known. For example, there can be a flat defect, delamination or disbonding in laminates or coatings. In such cases, it is necessary to define the area which the defect occupies. For this purpose an *automatic segmentation algorithm* [4] can be applied. Basically, the algorithm is an image processing technique adapted for the given problem. The algorithm consists of two stages: *1. defect localization* and *2. defect edge estimation*. It works as follows:

Initially, a moment image *TM* is computed as:

$$TM(i,j) = \sum_t IM(i,j,t) \; , \qquad\qquad\qquad (3.9)$$

where $IM(i,j,t)$ is a pixel of the captured thermal image with coordinates (i,j) at the time t. As seen from the equation, the image *TM* is computed from all images of the measured sequence. This implies that all thermal events which happen during the measurement are put in the single image *TM*. After that, the image is normalized in the unsigned integer range 0-255. As an example we present the image *TM* (see Figure 3.11) for a measured sample containing buried grooves in the form of letters. The sketch of this sample is depicted in Figure 3.10. Photographs are given in Appendix C.
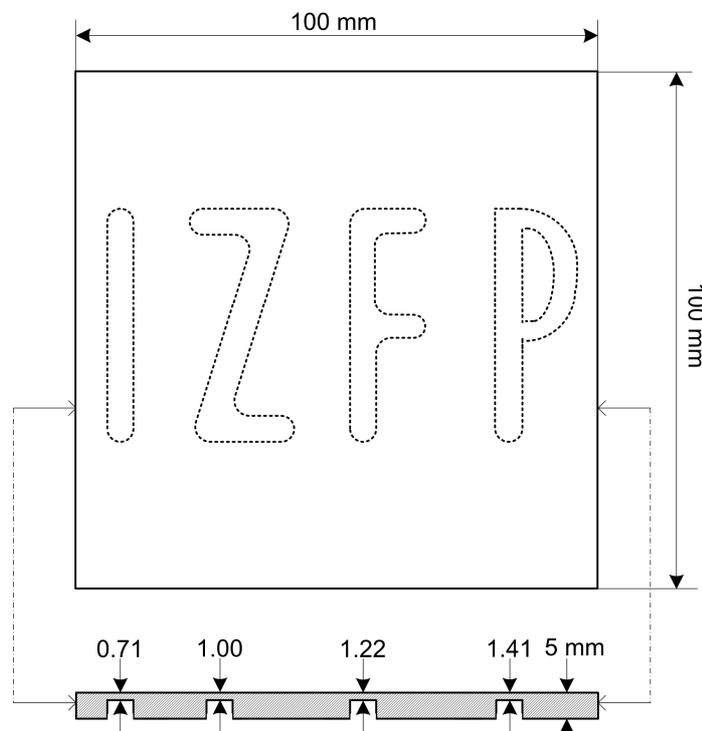
Figure 3.10: Sketch of the inspected sample with 4 buried letter grooves.
At the bottom, a cross section is shown.

Figure 3.11: Moment image *TM* for the sample with buried grooves.

➢ *Stage: Defect Localization*

In the first stage the positions of the hottest points belonging to separate defects are defined. These points are called *seeds*. Seeds are mainly located in defect centers, but in some cases of complex defect geometries, or uneven heating, their positions can vary. The critical point is that seeds should lie above the corresponding defects.

The positions of the seeds are found using a global sorting process. In this sorting a one-dimensional vector *VEC* is initialized and filled with the pixels $TM(i,j)$. Each element r of the vector contains four variables – the grey value of the pixel $TM(i,j)$, x-position, y-position and the label associated with the pixel (*VEC*[*r*].*value*, *VEC*[*r*].*x*, *VEC*[*r*].*y* and *VEC*[*r*].*label*, respectively). The initialization of the vector is performed in the following way:

```
/* Initialization */
// - MxN  is the resolution of the image TM - //
for i=0 to (M-1)
  for j=0 to (N-1)
        r=i*M+j                 // - index variable - //
        VEC[r].value=TM(i,j)    // - grey value of pixel - //
        VEC[r].x= i             // - x-position of pixel - //
        VEC[r].y= j             // - y-position of pixel - //
        VEC[r].label= ""        // - label associated with pixel - //
   end
end
```

Then the global sorting procedure is performed with respect to the index r. The vector *VEC* is sorted in decreasing order by the conditions:

Condition 1: $VEC[r].value \geq VEC[r+1].value$
Condition 2: $VEC[r].x \geq VEC[r+1].x$ (3.10)
Condition 3: $VEC[r].y \geq VEC[r+1].y$

Finally, the pixels in the vector are labeled. The first pixel ($r=0$) is marked with the label "seed" ($VEC[0].label="seed"$). All subsequent pixels ($r=1, r=2,..$) are checked with pixels labeled previously. Pixel r is assigned with the label "seed" if for all pixels k in the range [0,r-1] the following condition is true:

$$\sqrt{\left(VEC[r].x - VEC[k].x\right)^2 + \left(VEC[r].y - VEC[k].y\right)^2} > MND \quad , \qquad (3.11)$$

where the constant *MND* (minimum neighbour distance) is established through trial and error. Basically, the conditions in Equation (3.11) mean that if the distance between the analyzed pixel and all preceding pixels exceeds the distance *MND*, the analyzed pixel r is marked as a "seed":

$$VEC[r].label = "seed" \quad . \qquad (3.12)$$

Figure 3.12 illustrates this searching in the one-dimensional case.
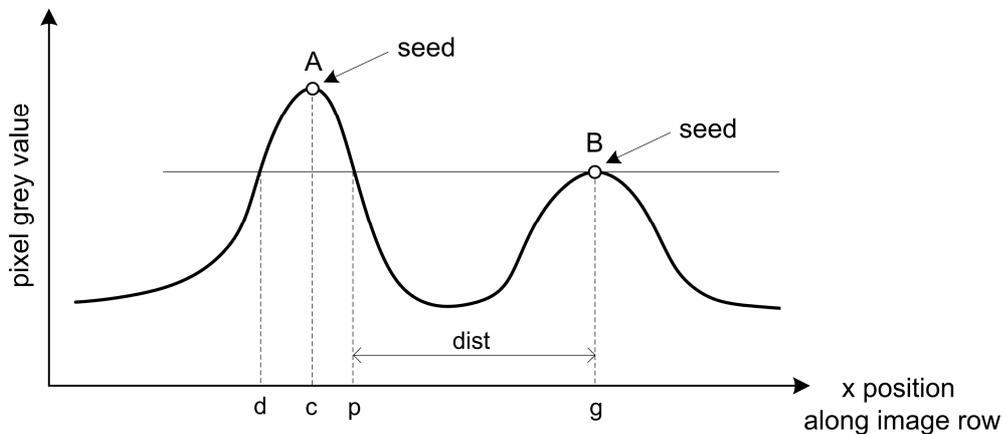
Figure 3.12: Principle used in the algorithm for defect detection.

The search can be explained as follows. Suppose there are two defects: blob "A" and blob "B". After the sorting procedure, the first pixel c belongs to blob "A" and is marked as a "seed". Then the labeling is performed by the criteria described above. The algorithm processes the pixels of blob "A" in the decreasing order of their grey values. The pixel g is processed after the pixels d and p as the vector *VEC* was initially sorted by the gray value. When the pixel g is processed, the distance *dist* even to the closest pixel p exceeds the predefined value *MND*:

$$dist > MND.\tag{3.13}$$

So the pixel is marked with the label "seed".

In practice, while the low grey-level pixels are processed there exists a risk of false labeling. It is caused by thermal noise and possible uneven heating effects. To avoid it, two methods are applicable: searching a predefined number of defects or a validation procedure. The first option requires operator analysis and the second option involves repeated labeling with:

$$MND' = MND + 1\tag{3.14}$$

until the same defect seeds are found in two successive tests.

The found positions of defect seeds are transmitted to the next stage.

> ### ➢ *Stage: Defect Edge Estimation*

In this stage, the algorithm extracts defect shapes. Each defect is processed individually. The defect shape is estimated using a sequential threshold procedure which starts from the defect seed. It works as follows: Assume there is a seed located in (i_d, j_d) having the grey value $TM(i_d, j_d)$. The initial threshold Th is set to:

$$Th = Th_{\max} = TM(i_d, j_d).\tag{3.15}$$

Further, the number of surrounding (neighbouring) pixels whose values are equal or greater than the current threshold Th is computed. The computation is performed applying the recursive procedure with respect to the seed pixel (i_d, j_d) and assuming a connectivity of eight (four edge and four corner pixels). The same search is repeated, decreasing the threshold sequentially:

$$Th' = Th - 1,\tag{3.16}$$

until all image pixels are included. Whenever the search is done the number of agglomerated pixels is put in a vector Nr for all potential thresholds Th. Figure 3.13 shows schematically the content of the vector Nr after such processing.
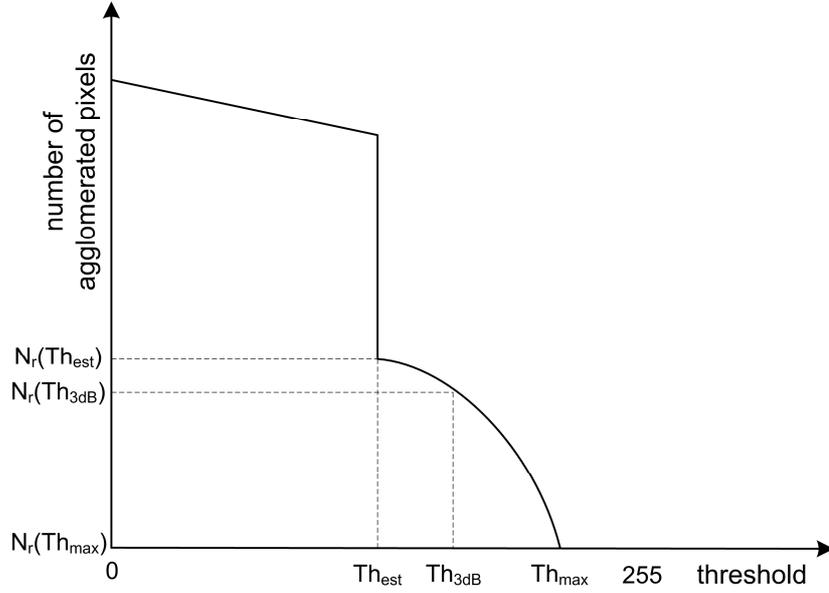
Figure 3.13: Schematic variation of the number of pixels agglomerated around a defect (seed) as a function of the threshold [4].

The following properties are remarkable: The curve starts from the point Th_{max} which is the hottest point of the defect. While decreasing the threshold value the curve rises. All collected pixels lie over the defect. In the point Th_{est} the number of agglomerated points increases dramatically. This is caused by the fact that in this point the threshold is equal to the image background. The result is a large number of collected pixels.

The defect shape estimations at the threshold Th_{est} are a bit wider with respect to manual segmentations considered as references. Better correspondence is achieved applying a corrective 3-dB factor (see Figure 3.13):

$$Nr\left(Th_{3dB}\right) = \frac{1}{\sqrt{2}}\, Nr\left(Th_{est}\right) \tag{3.17}$$

The algorithm presented here demonstrates satisfactory results in estimating the shapes of plain defects. We implemented and applied it for defect shape extractions. Figure 3.11 was utilized as a source image. For the defect localization we preset that the image contains 4 defects. Segmentations shown in Figure 3.14 were obtained.

At the end of the section we note that another method for shape estimations of planar defects is also considered in [4]. It operates on the same moment image *TM* but uses image gradient computations for detecting the defect contours. We do not describe this method here as it provides similar segmentation results.
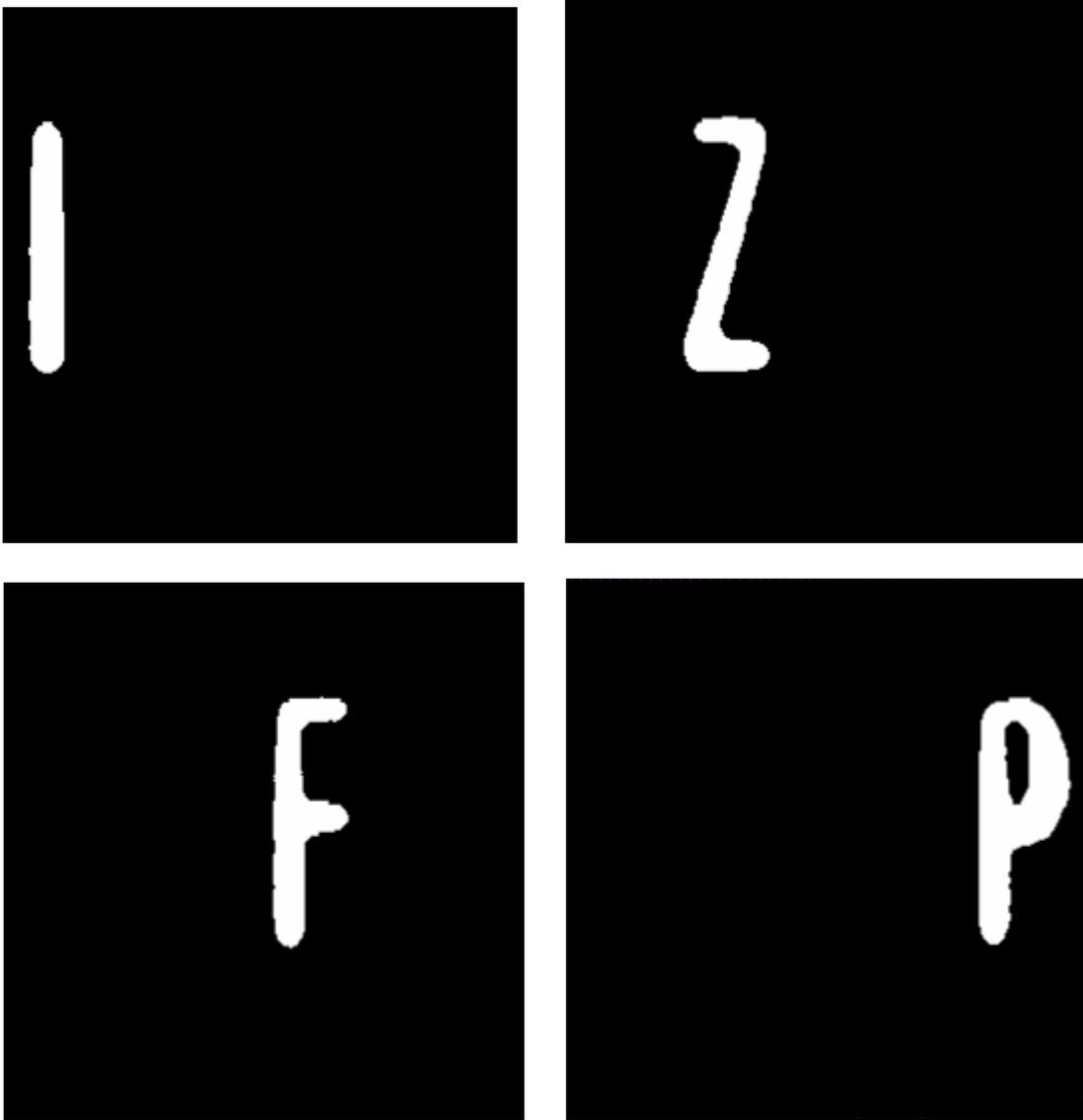
Figure 3.14: Experimental results obtained using
the automatic segmentation algorithm.

3.3.4 Inversion of thermal wave infrared images

The problem of reconstruction of the defect shape in the planar case was also considered in [16]. In this work the authors analyzed the blurring effect caused by lateral thermal diffusion. The proposed solution is based on a deconvolution of the thermal wave contrast image by a function which describes attenuation and dispersion during propagation and reflection of the thermal pulse. The method consists of the following:

In the case of a half-space sample with a planar defect parallel to the surface, located at a distance ℓ beneath the top surface, a Green's function solution to the heat equation derived using the first Born approximation and ignoring multiple scattering is:

$$w(x,y) = -\frac{A_Q}{2\pi}\left(\frac{1}{\pi\alpha t}\right)^{1/2}\frac{\partial}{\partial\ell}\frac{\exp\left(-\frac{\left((x^2+y^2+\ell^2)^{1/2}+\ell\right)^2}{4\alpha t}\right)}{(x^2+y^2+\ell^2)} ,$$
(3.18)

where A_Q is a constant involving the input energy density Q, α is thermal diffusivity of the sample (see Section 4.2), t is the elapsed time after heating, x and y are coordinates. The function $w(x,y)$ represents the thermal wave image formation, namely, propagation and dispersion of the thermal waves.

The planar defect shape is represented by the function:

$$o(x,y) = \begin{cases} 1 & \text{over the defect} \\ 0 & \text{elsewhere} \end{cases}$$
(3.19)

The absolute thermal contrast image $IM^{a.c}$ (image pixels are computed by Equation (3.2)) created on the sample surface at the time t is expressed as:

$$IM^{a.c}(x,y) = \iint w(x-x',y-y')o(x',y')dx'dy' .$$
(3.20)

The main concept constituting the core of the developed method is that the thermal contrast can be represented as a convolution between the shape function and the propagation function:

$$IM^{a.c}(x,y) = w(x,y) \otimes o(x,y) ,$$
(3.21)

where a symbol $\otimes$ denotes a convolution operator. Converting the equation (3.21) into Fourier space gives:

$$IM_F^{a.c}(u,v) = W_F(u,v)O_F(u,v) ,$$
(3.22)

where $IM_F^{a.c}(u,v)$ is the Fourier transform of the absolute contrast image, $W_F(u,v)$ is the Fourier transform of the propagation function, $O_F(u,v)$ is the Fourier transform of the defect shape function. Then the actual defect shape can be found as:

$$o(x,y) = F^{-1}\left(O_F(u,v)\right) = F^{-1}\left(\frac{IM_F^{a.c}(u,v)}{W_F(u,v)}\right),$$
(3.23)

where F^{-1} denotes the inverse Fourier transform. Authors in [16] presented also the experimental results of inversion. Figure 3.15 illustrates the defect shape inversion from the contrast image of a stainless steel plate containing a planar defect. The defect is made in the shape of a cross, its overall length is 25 mm. The defect is located in a depth of 1 mm below the front surface.

(a)   (b)
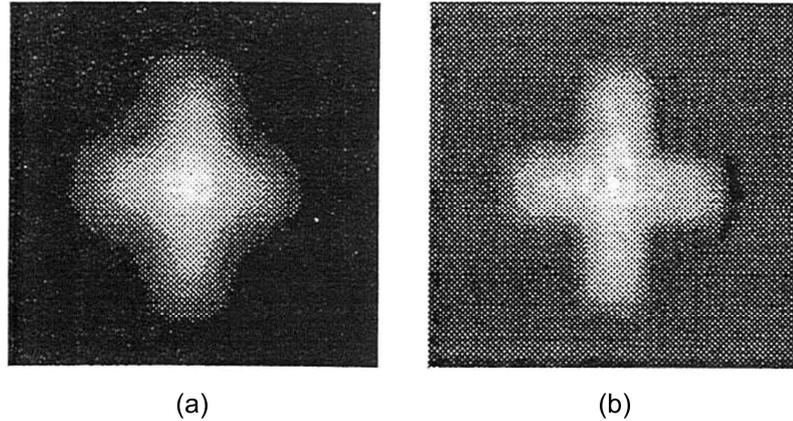
Figure 3.15: (a) Thermographic contrast image of the defect at 1.33 s,
(b) Deconvolution results [16].

As seen, the proposed inversion method reconstructs the original defect shape with satisfactory precision. For this method a priori knowledge of ℓ is necessary.

3.3.5 Defect shape inversion

Recent work [10] is devoted exactly to the problem studied here, namely, to the reconstruction of the defect shape which varies in depth and size. Authors in [10] consider the problem from the viewpoint of applied mathematics and focus on a particular case where the sample has constant thermal diffusivity and the defect surface is a perfect thermal insulator. A reconstruction algorithm based on sequential iterative correction is proposed.

The unique feature of the developed algorithm is that it creates a sample model which in the numerical simulation of the PT experiment produces thermal distribution close to the measurement of the investigated sample (sample with unknown defect shape). The sample geometry (length/width and thickness) and its thermal properties (density, thermal conductivity and specific heat) are considered to be known. Initially, the sample is regarded as defect-free. Further, in each iteration the algorithm simulates the sample numerically under PT testing. It allows the comparison between the thermal responses from the defect shape reconstructed in the previous iteration and the actual (unknown) defect shape. Then the algorithm corrects the reconstructed shape forming the next approach to the actual defect shape. After that, the following iteration can be carried out. The main difference to the algorithm we propose (see Chapter 5) is a more

efficient reconstruction technique applied in our solution. This technique is based on correcting the shape at the initial phase when the temperature contrast begins to be detectable. The technique proposed in [10] is based on computing the square error between the cooling curves of the measurement and the model. Note also that the algorithm described in [10] has a higher computational load:

- Prior to the reconstruction, the algorithm simulates a defect-free sample under PT testing (a forward problem).

- To compare the thermal distributions of the measurement and the model, the algorithm performs 10 sub-simulations. The sub-simulations evaluate the influences of point excitations over the front sample surface. The simulated data are used for computing weighted coefficients which are involved in comparing the thermal distributions from the measurement and the model.

The efficiency of the algorithm was demonstrated by reconstructing two defect shapes in the 2D domain. The first shape was specified as $z_1 = 0.4h(0.2(x+2)) + 0.2h(0.3(x+4))$ and the second shape as $z_2 = 0.6h(0.8(x-0.5)) + 0.5h(0.9(x+1)) + 0.2h(0.3(x+4))$ where $h(k)$ is defined as $h(k) = 16k^2(1-k)^2$ for $0 < k < 1$, and $h(k) \equiv 0$ otherwise. In the test, the sample had a unit thermal diffusivity. The reconstruction results are shown in Figure 3.16. The solid curves are the actual shapes, the dotted curves depict the reconstructions. In each case the reconstruction involved 3 iterations.
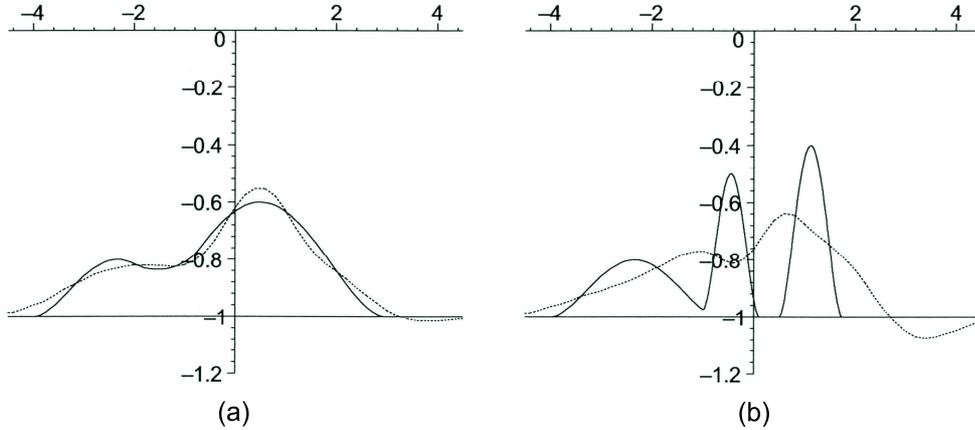
Figure 3.16: Reconstruction of the profile z_1 (left) and z_2 (right) [10].

The presented results demonstrate the following: The first shape is reconstructed with good precision whereas the second shape is still not recovered. Indeed, it is explained by an empirical rule [57,31] which states that the lateral resolution in PT varies with depth. We consider this rule in detail in Chapter 5. The single elements of the second defect shape (Figure 3.16 (b)) lie at the edge of the principal detection limit according to this rule. Therefore, its reconstruction is limited.

It should be also mentioned that there has been significant previous work devoted to the reconstruction of one-dimensional depth profiles of varying optical and thermophysical properties from time dependent thermal surface data [58-60]. The aim is the reconstruction of the energy deposition profile for homogeneous thermal properties (type I problem), the reconstruction of $\lambda(z) \cdot \rho(z) \cdot c(z)$ for surface absorption (type II problem) and the general problem with unknown thermal properties and absorption (type III problem) [59]. Targeted applications are hardness or moisture depth profiling. Among the inversion methods for solution of the type II problem are Chi-square based methods, thermal wave backscattering and Laplace effusivity inversion [61]. Neural networks were also employed. Up to now, transfer to application suffers from signal-to-noise limitations and, more seriously, from disturbing effects due to surface roughness and curvature.

Chapter 4

Heat transfer in pulsed thermography

This chapter introduces the fundamentals of heat conduction. The matter presented here is essential as it gives insight to physical processes involved in PT inspection. It also allows the simulation of the measurement process. This simulation provides insight into the heat propagation process and introduces new capabilities for developing the defect characterization methods.

4.1 Introduction

There are three ways of heat transfer [55,62,63]: conduction, radiation and convection. In heat conduction the energy is transferred by lattice vibrations and, for metals, by conduction electrons. Convection is characterized by a macroscopic motion of gas (or fluid) molecules in contact with the heated surface. For radiation transport, the energy is transferred by electromagnetic waves (photons). All these methods occur naturally in PT experiments. For many materials, the main mechanism for the thermal pulse propagation is solid heat conduction. The thermal influences of radiation and convection are slight, so they are often neglected.

In the following sections, we derive the heat conduction equation and give an overview on numerical methods for solving it. We discuss how a PT experiment is simulated. We also pay attention to the low emissivity problem which is significant in PT.

4.2 Heat conduction

The heat conduction process in a medium can be described using small differential elements or control volumes to which the principle of energy conservation is applied [55]. Figure 4.1 shows the differential control volume element with the dimensions *dx, dy, dz* in the Cartesian coordinate system. q_x, q_y, q_z are heat fluxes entering the element. q_{x+dx}, q_{y+dy}, q_{z+dz} are heat fluxes coming out of the element.
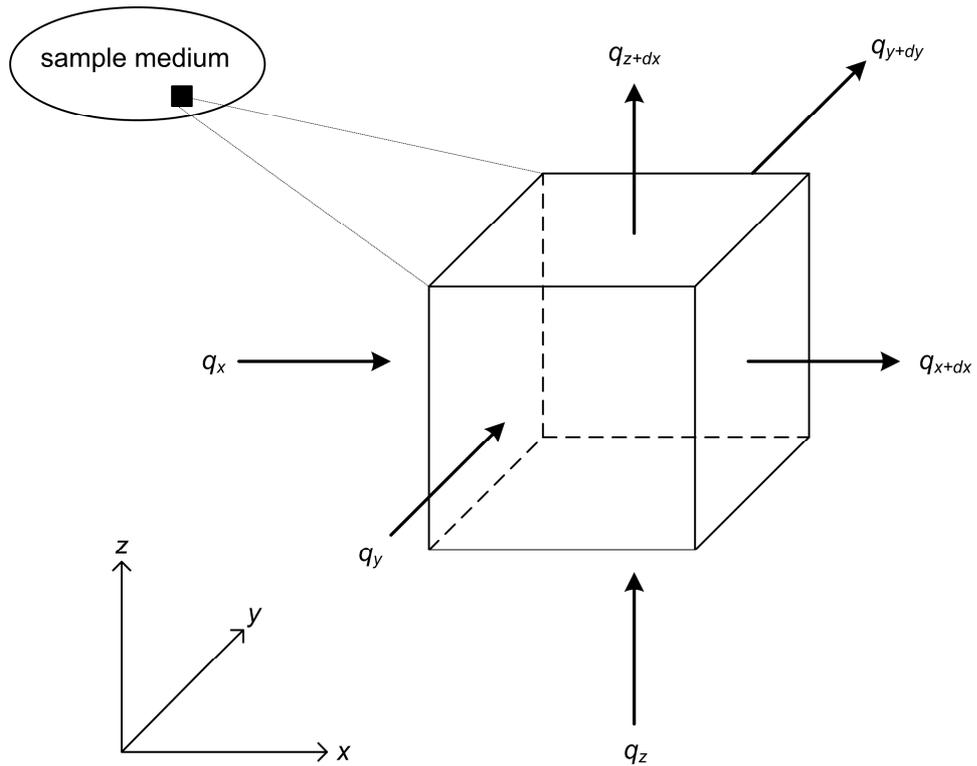
Figure 4.1: Differential control volume element in the Cartesian coordinate system.

The principle of energy conservation for a singular element is expressed as:

$$\dot{Q}_{in} - \dot{Q}_{out} + \dot{Q}_g = \dot{Q}_{str}, \tag{4.1}$$

where $\dot{Q}_{in}$ is the rate of energy flow into the element

$$\dot{Q}_{in} = q_x + q_y + q_z, \tag{4.2}$$

$\dot{Q}_{out}$ is the rate of energy flow out of the element

$$\dot{Q}_{out} = q_{x+dx} + q_{y+dy} + q_{z+dz}, \tag{4.3}$$

$\dot{Q}_g$ is the rate of energy generation within the element

$$\dot{Q}_g = gdxdydz, \tag{4.5}$$

(g is the rate of energy generated per unit volume within the medium)

$\dot{Q}_{str}$ is the rate of energy storage in the element

$$\dot{Q}_{str} = \rho c \frac{\partial T}{\partial t} dxdydz \ , \tag{4.6}$$

ρ and c are the density and specific heat capacity of the medium.
Substituting these variables in Equation (4.1) gives:

$$q_x + q_y + q_z - q_{x+dx} - q_{y+dy} - q_{z+dz} + gdxdydz = \rho c \frac{\partial T}{\partial t} dxdydz \ . \tag{4.7}$$

The heat fluxes coming out of the element can be evaluated by a Taylor expansion neglecting high order terms:

$$q_{x+dx} = q_x + \frac{\partial q_x}{\partial x} dx \ , \quad q_{y+dy} = q_y + \frac{\partial q_y}{\partial y} dy , \quad q_{z+dz} = q_z + \frac{\partial q_z}{\partial z} dz \ . \tag{4.8}$$

Inserting these equations yields:

$$-\frac{\partial q_x}{\partial x} dx - \frac{\partial q_y}{\partial y} dy - \frac{\partial q_z}{\partial z} dz + gdxdydz = \rho c \frac{\partial T}{\partial t} dxdydz \ . \tag{4.9}$$

The heat fluxes q_x, q_y, q_z entering the element can be expressed by Fourier's law:

$$q_x = -\lambda_x dydz \frac{\partial T}{\partial x}\bigg|_x \ , \quad q_y = -\lambda_y dxdz \frac{\partial T}{\partial y}\bigg|_y \ , \quad q_z = -\lambda_z dxdy \frac{\partial T}{\partial z}\bigg|_z , \tag{4.10}$$

λ_x, λ_y, λ_z are the thermal conductivities of the medium in x, y, z-directions.
Substituting these equations leads to:

$$\frac{\partial}{\partial x}\left(\lambda_x dydz \frac{\partial T}{\partial x}\right)dx + \frac{\partial}{\partial y}\left(\lambda_y dxdz \frac{\partial T}{\partial y}\right)dy + \frac{\partial}{\partial z}\left(\lambda_z dxdz \frac{\partial T}{\partial z}\right)dz +$$
$$+ gdxdydz = \rho c \frac{\partial T}{\partial t} dxdydz \tag{4.11}$$

The equation (4.11) is the general form of the heat diffusion equation.

For further consideration, the following conditions are assumed:

1) In most cases the sample medium is isotropic and homogeneous. This means that the thermal conductivities in x, y, z-directions are a constant:

$$\lambda_x = \lambda_y = \lambda_z = \lambda = const \tag{4.12}$$

2) There is no internal heat generation:

$$g = 0 \tag{4.13}$$

The heat diffusion equation (4.11) under these conditions is simplified to the following form:

$$\frac{\partial^2 T}{\partial x^2} + \frac{\partial^2 T}{\partial y^2} + \frac{\partial^2 T}{\partial z^2} = \frac{1}{\alpha}\frac{\partial T}{\partial t}, \tag{4.14}$$

where $\alpha = \dfrac{\lambda}{\rho c}$ is the thermal diffusivity.

Equation (4.14) describes the heat conduction process in the sample medium.

4.3 Numerical methods

The heat equation derived above is a partial differential equation (PDE). Basically, there are two ways of solving it: analytically and numerically. Presently, analytical solutions have been obtained for some particular cases. In practice, numerical solving is used more often as numerical methods do not have limitations on the shape/size and permit the involvement of any boundary conditions in steady as well as in transient state. There are three numerical methods applied for solving PDE:

- Finite Difference Method (FDM)
- Finite Element Method (FEM)
- Boundary Element Method (BEM)

The methods can be seen as a particular version of a more general approach – *method of weighted residuals*. Here we present numerical methods in short form. For a better illustration, the methods are shown for the 2D case. More detailed description is given in [64-71]. Note that simulations in this study were done using FEM-based software tools – ANSYS [72] and FEMLAB [73]. We also implemented and used FDM in MATLAB scripts. Indeed, any tools using any of those methods can be applied.

4.3.1 Finite difference method

This method is based on an approximation of derivatives in the source (heat conduction) equation by finite differences [65,66]. The source domain is partitioned in space, normally using a rectangular mesh (see Figure 4.2) and in time t^0, t^1, …, t^N.
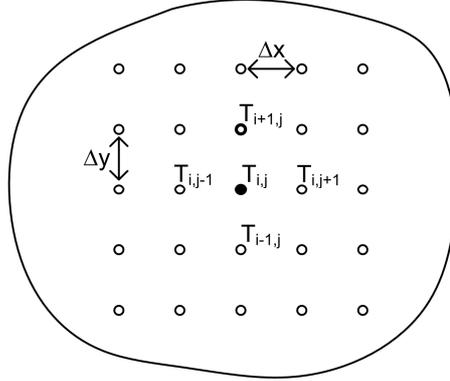
Figure 4.2: Schematic illustration of a finite difference mesh.

The space derivatives are expressed as:

$$\frac{\partial^2 T^n}{\partial x^2} = \frac{T_{i,j-1}^n - 2T_{i,j}^n + T_{i,j+1}^n}{(\Delta x)^2} \quad , \quad \frac{\partial^2 T^n}{\partial y^2} = \frac{T_{i-1,j}^n - 2T_{i,j}^n + T_{i+1,j}^n}{(\Delta y)^2} \quad , \tag{4.15}$$

where the top index n denotes the same time step, Δx and Δy are mesh intervals as shown in Figure 4.2.

The time derivative is approximated as:

$$\frac{\partial T}{\partial t} = \frac{T_{i,j}^{n+1} - T_{i,j}^n}{\Delta t} \quad , \tag{4.16}$$

where Δt is the time step.

Further, the heat conduction equation is represented by *explicit, implicit* or *Crank-Nicolson* methods. They are given as follows.

Explicit method:

$$\frac{1}{\alpha} \frac{T_{i,j}^{n+1} - T_{i,j}^n}{\Delta t} = \frac{T_{i,j-1}^n - 2T_{i,j}^n + T_{i,j+1}^n}{(\Delta x)^2} + \frac{T_{i-1,j}^n - 2T_{i,j}^n + T_{i+1,j}^n}{(\Delta y)^2} \tag{4.17}$$

This method is numerically stable if $\dfrac{\alpha \Delta t}{(\Delta s)^2} \leq \dfrac{1}{2}$ where Δs is the smallest value among Δx and Δy [65].

Implicit method:

$$\frac{1}{\alpha}\frac{T_{i,j}^{n+1}-T_{i,j}^{n}}{\Delta t} = \frac{T_{i,j-1}^{n+1}-2T_{i,j}^{n+1}+T_{i,j+1}^{n+1}}{(\Delta x)^2} + \frac{T_{i-1,j}^{n+1}-2T_{i,j}^{n+1}+T_{i+1,j}^{n+1}}{(\Delta y)^2} \tag{4.18}$$

This method is unconditionally stable.

Crank-Nicolson method:

$$2\left(\frac{1}{\alpha}\frac{T_{i,j}^{n+1}-T_{i,j}^{n}}{\Delta t}\right) = \frac{T_{i,j-1}^{n}-2T_{i,j}^{n}+T_{i,j+1}^{n}}{(\Delta x)^2} + \frac{T_{i-1,j}^{n}-2T_{i,j}^{n}+T_{i+1,j}^{n}}{(\Delta y)^2} +$$
$$+\frac{T_{i,j-1}^{n+1}-2T_{i,j}^{n+1}+T_{i,j+1}^{n+1}}{(\Delta x)^2} + \frac{T_{i-1,j}^{n+1}-2T_{i,j}^{n+1}+T_{i+1,j}^{n+1}}{(\Delta y)^2} \tag{4.19}$$

This method is unconditionally stable.

In transient problems the explicit method allows the computation of the result directly from the previous time step. The implicit and Crank-Nicolson methods form the system of linear equations to be solved.

The advantage of FDM is its easy implementation. The accuracy of FDM depends on the approximation method. The explicit method is the least accurate and can be unstable, the Crank-Nicolson method is considered to be the most accurate, the implicit method is preferable for large time steps.

4.3.2 Finite element method

An other method proposed for solving partial differential equations is the finite element method (FEM). Contrary to FDM, this method is based on integration of the source equation. Here we present only basics of the method as the original description is quite long and in some references takes almost a whole book volume. Detailed description of FEM is given in [67-69].

In FEM the source domain is split into *E* subdomains called *finite elements*. Elements can have different shapes. The most popular shapes in the 2D domain are triangles and quadrangles, in the 3D domain - tetrahedra or hexahedra. The element has control nodes which are connected with other elements or lie on the boundary of the source domain. Figure 4.3 illustrates the splitting (called also meshing) the 2D area into triangle elements.
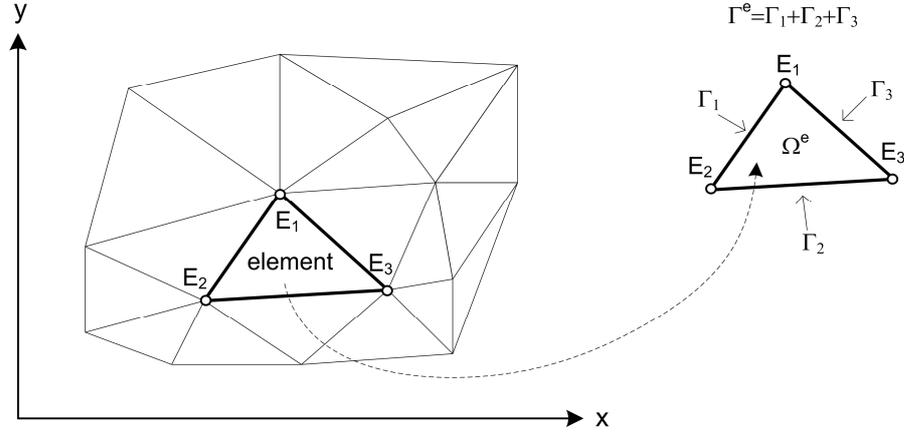
Figure 4.3: Schematic illustration of a finite element mesh.

Within the element the temperature is approximated as:

$$T(x,y) \approx T^e(x,y) = \sum_{j=1}^{n} T_j^e \varphi_j^e(x,y) \ , \tag{4.20}$$

where $T^e(x,y)$ is an approximation of $T(x,y)$ over the element domain Ω^e, T_j^e is the value of $T^e(x,y)$ at the j-th node with coordinates (x_j, y_j) of the element (T_j^e is also referred as the nodal temperature), φ_j^e are interpolation functions which satisfy the following condition:

$$\varphi_i^e(x_j, y_j) = \begin{cases} 1 & if \quad i = j \\ 0 & if \quad i \neq j \end{cases} \tag{4.21}$$

The interpolation functions can be linear and high order polynomials. Here, for better illustration, we consider the linear polynomial. In the case of triangular elements, the linear interpolation functions are expressed as:

$$\varphi_i^e(x,y) = \frac{1}{2A_e}(\eta_i^e + \beta_i^e x + \gamma_i^e y), \ (i=1,2,3) \ , \tag{4.22}$$

where A_e is the area of the triangle, and $\eta_i^e, \beta_i^e, \gamma_i^e$ are geometrical constants which are computed for each *i*-node using coordinates of other nodes *k* and *j*:

$$\eta_i^e = x_j y_k - x_k y_j \ ; \ \beta_i^e = y_j - y_k \ ; \ \gamma_i^e = -(x_j - x_k)$$

Figure 4.4 depicts the interpolation function φ_1^e in the triangle element schematically.
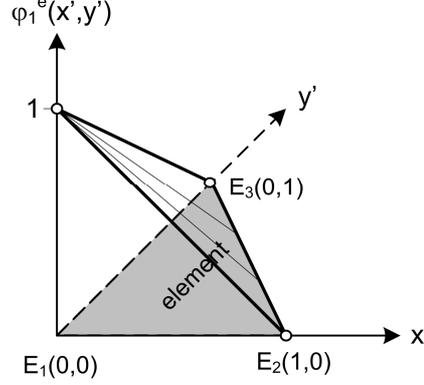
Figure 4.4: Interpolation function φ_1^e in the triangular element
(The element is shown in the unit local coordinate system(x',y')).

Further, FEM equations can be derived in various ways. Prior to it, a weak form of the governing (heat conduction) equation is defined. One of the most popular approaches is a Galerkin approach. It combines residuals of the governing equation and boundary conditions defined particularly in our case as:

$$-\lambda \frac{\partial T}{\partial n} = f_n^q \text{ , where } n \text{ is the unit normal, } f_n^q \text{ is external heat flux density, (4.23)}$$

and demands that the summation of their integrals has to be equal to zero for every weight function in the form of φ_i^e:

$$\int_{\Omega^e} \varphi_i^e \left(\alpha \nabla^2 T^e - \frac{\partial T^e}{\partial t} \right) d\Omega + \oint_{\Gamma^e} \varphi_i^e \left(\lambda \frac{\partial T^e}{\partial n} + f_n^q \right) d\Gamma = 0 \qquad (4.24)$$

The equation above has the following solution (in the matrix form):

$$\left[M^e \right] \left\{ \dot{T}^e \right\} + \left[K^e \right] \left\{ T^e \right\} = \left\{ B^e \right\} \text{ ,} \qquad (4.25)$$

where $\dot{T}^e = \partial T^e / \partial t$ is the time derivative , $\left[M^e \right]$ is the *capacity matrix* (also known as *mass matrix*), $\left[K^e \right]$ is the *conductivity matrix* (also known as *coefficient matrix*), $\left\{ B^e \right\}$ is a vector obtained from applied boundary conditions. These entities of matrices are given as:

$$M_{ij}^e = \int_{\Omega^e} \rho c \varphi_i^e \varphi_j^e d\Omega \qquad (4.26)$$

$$K_{ij}^e = \int_{\Omega^e} \lambda \left(\frac{\partial \varphi_i^e}{\partial x} \frac{\partial \varphi_j^e}{\partial x} + \frac{\partial \varphi_i^e}{\partial y} \frac{\partial \varphi_j^e}{\partial y} \right) d\Omega \tag{4.27}$$

$$B_i = \oint_{\Gamma^e} f_n^q \varphi_i^e \, d\Gamma \tag{4.28}$$

Then, in practice, the time derivative is usually approximated by the finite differences. Any of the methods (*explicit, implicit, Crank-Nicolson*) can be chosen and combined with the obtained equation (4.25). In this way, approximating the heat conduction equation in the time by finite differences and in space by interpolation function, the nodal temperatures T_j^e are computed.

4.3.3 Boundary element method

The boundary element method [70,71] was developed for cases where only values lying on the boundary of the domain are of interest. In this method the solution is obtained by weighting the residuals of the governing equation with a so-called *fundamental solution* and integration twice over space and time. The boundary conditions are also involved. It leads to the following equation:

$$\int_0^t \int_\Omega \left(\alpha \nabla^2 T - \frac{\partial T}{\partial t} \right) T^* d\Omega dt + \int_0^t \oint_\Gamma \left(\lambda \frac{\partial T}{\partial n} + f_n^q \right) T^* d\Gamma dt = 0 \; , \tag{4.29}$$

where T^* is the fundamental solution which in the 2D domain has the form:

$$T^* = \frac{1}{4\pi\alpha(t-\tau)} \exp\left(-\frac{r^2}{4\alpha(t-\tau)} \right) \; , \tag{4.30}$$

T^* determines a temperature field at any point at time t due to a spontaneous heat source acting at point i (see Figure 4.5) and at time τ, r is shown in Figure 4.5.

By transforming and rearranging the terms of the equation (4.29), a form where only boundary integrals are involved can be obtained. Then the solution of the equation can be computed by approximating the temperature using nodal values and interpolation functions (constant, linear, quadratic and so on) in a similar fashion to that described for FEM. But in this method only the boundary of the domain should be discretized (see Figure 4.5) as the approximated integral equation contains only boundary values.
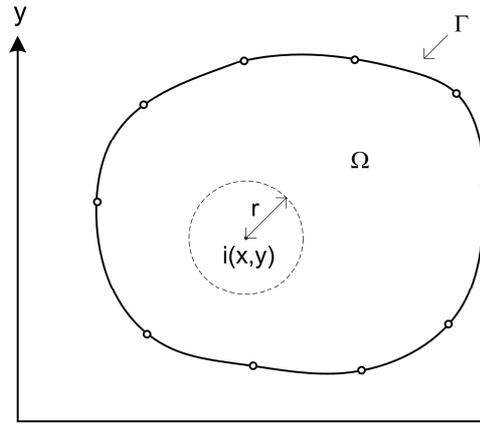
Figure 4.5: Schematic illustration of boundary element mesh.

BEM is referred to as having a more sophisticated implementation in comparison to FEM. One should also note that in some cases where the material is inhomogeneous the boundary element method can not be applied, as the fundamental solution for those cases is not defined.

4.4 Simulation of PT experiments

Today, various software tools that permit the simulation of heat transfer processes are available. The tools differ in user interfaces, applied numerical methods and have their own limitations. Despite the differences the way to build the simulation model is similar. Here we discuss some features in building the simulation model for PT.

Creating the simulation model involves the following steps:

1) *sample geometry specification and meshing*
2) *setting initial conditions*
3) *prescribing boundary conditions*

We consider these steps for a bar shaped sample in a 2D case.

➢ ***Step: sample geometry specification and meshing***

In the first step, the user creates the physical model of the inspected sample. The geometrical sample dimensions (length/width, thickness) are assigned. The geometry of the defect is inserted into the model. Further, the user specifies thermal properties of the sample and the defect medium. In the case of air defects (corrosion or inclusion) the user is free to cut out the defect volume (consider it to be a void volume) or assign thermal properties of air. Our tests demonstrated that the difference in thermal responses

on the front surface of the sample from air and void defects is negligible. This feature was explained in detail in the previous chapter.

Once the model has been created and the thermal properties have been assigned, the model is meshed. Meshing splits the sample into small volume elements or defines positions of nodes for further numerical approximation. To get good agreement with the natural experiments, it is recommended that the front subsurface part of the simulated sample is filled with a fine mesh. It is explained by the fact that in that sample part the largest temperature variation (thermal excitation and cooling) is observed, therefore, fine meshing is preferable.

➢ *Step: setting initial conditions*

The initial sample temperature is set to 0.

Note: Theoretically, it would be reasonable to set the initial temperature equal to the laboratory temperature. In this case the comparison of the absolute temperature between the laboratory experiment and the simulation seems to be possible. But, in fact, variations of the laboratory temperature and other side effects make such comparison difficult. That is why, in practice, the simulation and the experiment is compared by *thermal contrasts* described in the previous chapter. Thermal contrasts extract the difference of the temperature on the sample surface. Due to the linearity of many testing problems, the initial sample temperature in the simulation is not critical except in cases where temperature dependent sample thermal properties are considered.

➢ *Step: prescribing boundary conditions*

The boundary conditions are specified by prescribing heat flux densities on the sample sides (Neumann or second kind boundary condition). Figure 4.6 illustrates it schematically.
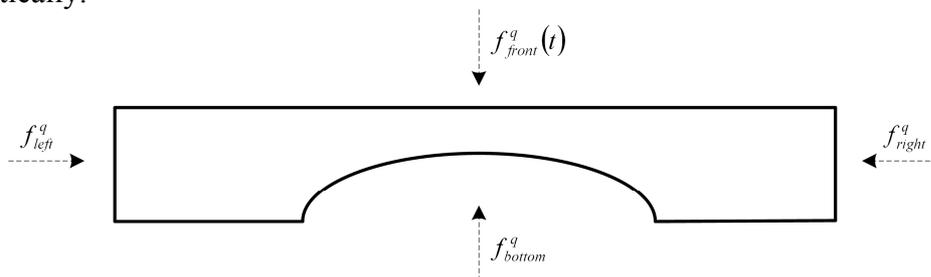
Figure 4.6: External heat flux densities in the simulated sample model.

In the PT testing the sample does not have external thermal impacts on the left, right and bottom sides, therefore, and due to the poor effusivity of the surrounding air, the prescribed heat flux densities ($f_{left}^{q}, f_{right}^{q}$ and f_{bottom}^{q}) are set to 0. The heat flux density on the front side should be specified according to the amount of the energy

density Q absorbed by the sample in the excitation phase. The actual heat flux density f_{front}^{q} coming from flash lamps varies in time over the pulse duration t_{ex}. In the simulation this flux is usually approximated in the rectangular form as shown in Figure 4.7.
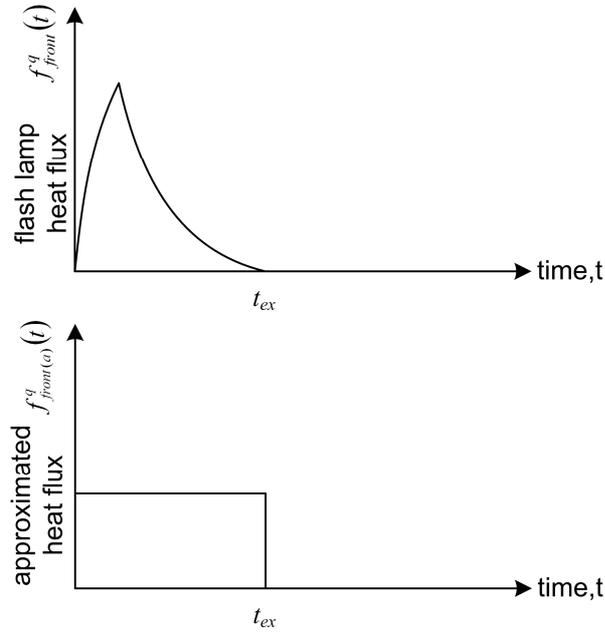
Figure 4.7: Actual and approximated front heat flux densities.

The approximated value $f_{front(a)}^{q}$ is found by simulating the temperature on the front surface of the sample after the thermal excitation:

$$\int_{0}^{t_{ex}} f_{front(a)}^{q}(t)dt = \int_{0}^{t_{ex}} f_{front}^{q}(t)dt = Q \tag{4.31}$$

The absolute temperature increase with respect to the initial temperature (prior to the excitation) in the simulation should be close to the temperature increase in the experiment.

After the model has been built, the simulation is computed in the time interval of interest. Furthermore, to compare the simulation with the experiment, various thermal contrasts are employed.

4.5 Emission and absorption problem in PT

When inspecting a metal sample, the problem of low surface emissivity appears. First, the problem is revealed in the excitation phase. While flash lamps illuminate the

sample, the front surface acts like a mirror reflecting the radiated energy. This results in insufficient thermal stimulation so that the thermal contrast induced by subsurface defects is hardly distinguishable in the thermal noise. Second, the problem is revealed in the observation phase while the sample emits energy. The radiative heat flux density coming from the sample is defined by Stefan-Boltzmann´s law:

$$f_{rd}^q = \varepsilon \sigma_{SB} T_s^{\ 4} \ ,$$ (4.32)

where T_s is the temperature (K) of the front surface of the sample, σ_{SB} is the Stefan-Bolzmann constant (5.67×10^{-8} W m^{-2} K^{-4}) and ε is the emissivity coefficient (lies in the range [0, 1]). The emissivity coefficient ε characterizes radiative properties of the surface. The perfect radiator [55] called a blackbody has a unit emissivity ($\varepsilon=1$). The perfect reflector has zero emissivity ($\varepsilon=0$). If the inspected sample is made of aluminium or steel, the emissivity coefficient is about 0.1. It is very difficult to stimulate such sample as well as to observe quantitatively its cooling. These effects can be explained by Kirchhoff's law [4] which informally states that a good reflector is a poor emitter. An efficient solution to overcome the problem is to coat the front surface of the sample with a thin layer of black paint. It solves the problems associated with both energy absorption in the stimulation and energy radiation in the observation. It is necessary to note that such a coating has a certain impact on the cooling process as thermal properties of the coating are different from the sample thermal properties. In contrast to the sample, the black paint usually has a low effusivity. This discrepancy causes an overheating effect in the early time period after flashing. As time passes, the effect gets weaker and can be ignored. The time when the thermal influence of the coating becomes negligible is related to the coating thickness th_c. To demonstrate this, we simulated a half-space steel sample in the uncoated state and coated with 5 and 10 µm thin black paint. Figure 4.8 (a) illustrates the uncoated sample and (b) shows the sample coated with black paint.
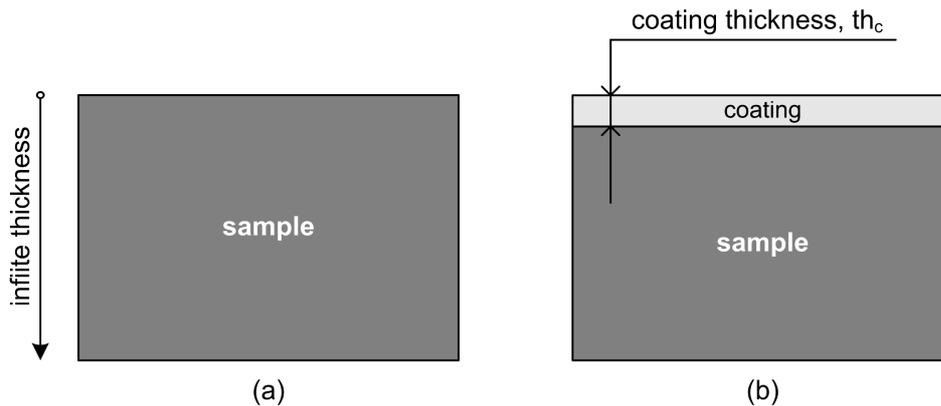
Figure 4.8: An sample of infinite thickness without coating (a) and with coating (b).

In the first case (Figure 4.8 (a)), as it is defined in theory [55], the front surface temperature of the homogeneous sample after a Dirac delta pulse is described as:

$$T(t) = \frac{Q}{2e_s \sqrt{\pi t}} \quad , \tag{4.33}$$

where e_s is the thermal effusivity of the sample. In the second case (Figure 4.8 (b)), the temperature on the front surface is given in [55] as:

$$T(t) = \frac{Q}{2e_c \sqrt{\pi t}} \left(1 + 2 \sum_{n=1}^{\infty} (K_{ref})^n \exp\left(-\frac{n^2 (th_c)^2}{t(\alpha_c)} \right) \right) \quad , \tag{4.34}$$

where th_c, e_c and α_c are the thickness, thermal effusivity and diffusivity of the coating, K_{ref} is the reflection coefficient between two media (see Equation (3.1)). As being said, we simulate the steel sample ($\lambda=15$ W/mK, $\rho=8000$ kg/m^3 and $c=477$ J/kgK) in the pure state and coated by black paint ($\lambda=0.15$ W/mK, $\rho=1100$ kg/m^3 and $c=1200$ J/kgK) with the thickness 5 and 10 μm, $Q=10\ 000$ J/m^2. The computed cooling curves are depicted in Figure 4.9.
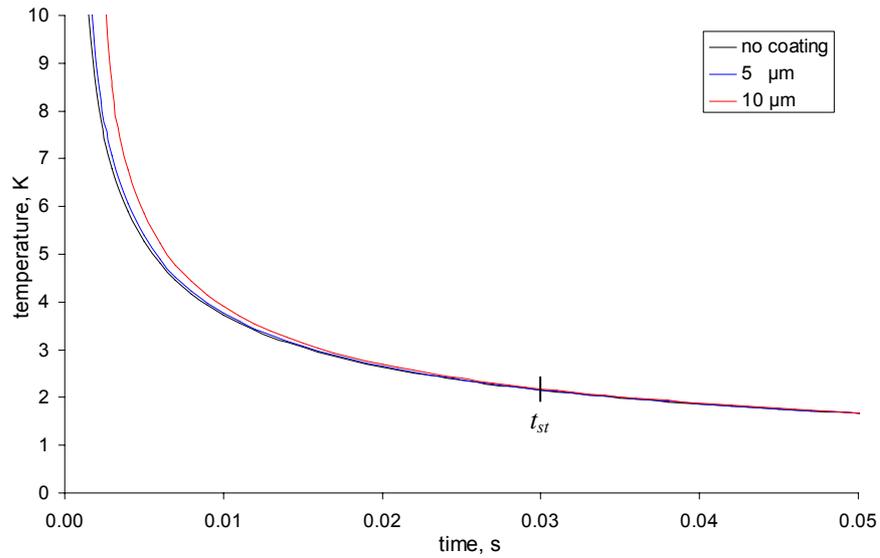
Figure 4.9: Thermal influence of 5 and 10 μm thin black paint coatings on the cooling process.

As seen, after a certain time period t_{st} (for example, 0.03 s for 10 μm thin coating) the coating effect becomes negligible. It was essential to demonstrate this effect as in many practical cases low emissivity materials are inspected and we should apply this technique. The main idea we emphasize is that after a certain time period the thermal influence of the thin paint coating is negligible and the cooling process is determined by the sample thermal properties.

Chapter 5

Defect shape reconstruction

The first problem posed in this work is to reconstruct the defect shape in a test sample with known thermal properties. We assume that the shape varies with depth, as well as with length/width. In this chapter we present an algorithm developed for this purpose. The algorithm combines principles of one-dimensional defect depth retrieval and facilities of thermal modelling. Such a combination introduces new capabilities for the reconstructions.

The proposed algorithm consists of a defect shape correction unit and a simulation unit. The defect shape correction unit is designed to extract the defect shape roughly and refine it sequentially while the simulation unit models the heat conduction process in the inspected sample. The developed iterative algorithm is able to reconstruct 2D as well as 3D defect shapes. The algorithm was tested using simulated and experimental data.

5.1 Defect shape reconstruction algorithm

Prior to the algorithm description, we should make two remarks about PT. The first remark is that in PT defect sensitivity and lateral resolution are parameters that vary with depth. If we consider defects like flat bottom holes, an empirical rule [57] says that *the radius of the smallest detectable defect should be at least one to two times larger than its depth under the surface*. This rule establishes that sensitivity is a variable parameter depending on the defect depth. The second remark is that the problem of defect shape reconstruction is ill-posed. From the mathematical point of view it means that two or more similar defect shapes can produce a practically equal temperature response on the front surface. For example, we simulate two defects: in both cases the defects are the flat bottom holes, but in the second case we slightly round the sharp corners of the top hole part. In both cases the computed temperature distributions on the front surfaces are equal within the present measurement precision. This fact demonstrates the strong scattering effect in PT. These remarks are related to properties of the thermal diffusion process. We describe them in order to show limitations in PT affecting the reconstruction. It is obvious that we can reconstruct the defect shape or parts of it only when they influence the temperature distribution on the front surface during the measurement. To separate PT limitations at the developing stage of the defect shape reconstruction algorithm, we assume that the defect shape satisfies the sensitivity

criteria (the length scale of the defect shape variation is larger than the defect depth) and the defect shape is smooth (does not contain sharp edges).

The algorithm we propose reconstructs the defect shape in the test sample. We assume that thermal properties (thermal conductivity, specific heat, density) and geometry (length, width, thickness) of the test sample are known. The thermal properties of the defect are also assumed to be known. The algorithm is capable of carrying out the reconstruction in the two-dimensional as well as in the three-dimensional domain. In this work we describe the algorithm for the case where the excited thermal wave suffers full reflection from the defect and the back sample surface. We do this in order to put the reconstruction principles in the foreground. Note that the algorithm in the way we describe it here can already be applied to the reconstruction of corrosion shapes or any air containing defects as the reflection coefficient [4] for most metals, alloys and polymers to air is close to 1.

The developed algorithm has a structure that is shown in Figure 5.1. It comprises a defect shape correction unit and a simulation unit. The simulation unit has a model of the test sample (as the thermal properties and geometrical sizes are known) and is able to simulate the PT experiment. The algorithm operates as follows: The pulsed thermography measurement with unknown defect shape is processed by the defect shape correction unit. The unit extracts a first approximate defect shape and transmits it to the simulation unit. The simulation unit inserts the expected defect shape in the test sample model and simulates the pulsed thermography measurement. Then the computed simulation is transmitted to the defect shape correction unit. The unit corrects the defect shape analyzing the difference between the measurement and the simulation. Again, the defect shape is transmitted to the simulation unit. The process is repeated in the same order. The defect shape is corrected iteratively until the simulation converges to the measurement. After some iteration cycles the defect shape correction unit provides the reconstructed defect shape.
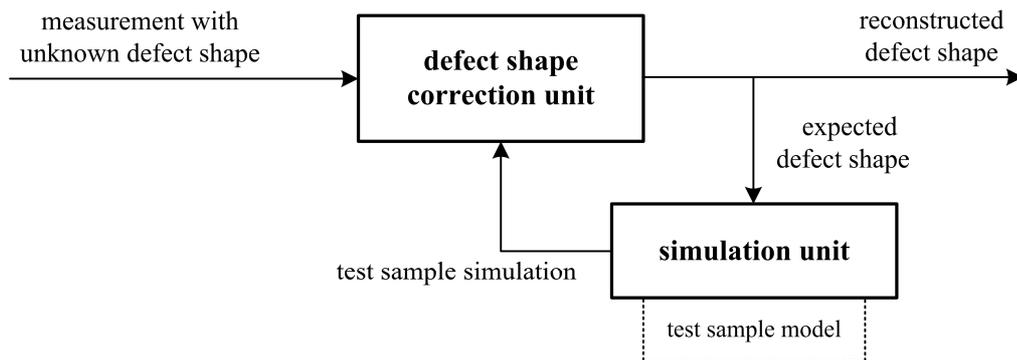
Figure 5.1: The algorithm structure.

A unique aspect in the algorithm is to find a defect shape which produces the same temperature distribution on the front surface close to the real measurement. Even in the 1D case, there is usually no direct analytical solution of this inverse problem [74]. In the 2D case there is no direct analytical solution of the forward problem (the simulation of

the test sample having arbitrary defect shape in the PT measurement). Only numerical methods are able to solve this forward problem. Therefore, we propose an iterative reconstruction algorithm where the simulation unit is used as a forward solver to simulate the internal heat conduction process in the test sample after its thermal excitation.

In the following subsections the defect shape correction unit and the simulation unit are described.

5.1.1 Defect shape correction unit

The defect shape correction unit performs two tasks. It extracts an estimate of the defect shape from the measurement at the initial step and corrects the shape after each simulation. Both tasks are performed applying the principle of extracting and refining the shape at the early time phase when the defect temperature response on the front surface is not blurred much by the thermal diffusion process. We emphasize that the temperature deviations on the front test sample surface detected at the early time phase contain the most valuable information about the defect shape that is possible to get. As time passes, due to the thermal diffusion, the defect temperature response trends toward the temperature equilibrium making the defect shape extraction more difficult.

Prior to the unit description, we introduce a new definition: *echo defect shape*. The echo defect shape is computed for all surface points at which the defect may affect the temperature. It makes sense to detect the defect and define its depth using a one-dimensional technique.

First, some theoretical aspects concerning heat diffusion are considered. A solution for the sample temperature $T(z,t)$ of a one-dimensional diffusion equation for a defect-free surface absorbing sample of infinite-thickness has the following form [55]:

$$T(z,t) = \frac{Q}{2\sqrt{\pi}\sqrt{\lambda\rho c}\sqrt{t}} \exp\left(-\frac{\rho c}{4\lambda t} \cdot z^2\right), \qquad (5.1)$$

where z is the sample depth, t is the elapsed time after delta pulse heating, Q is the input energy density, λ is the thermal conductivity, ρ is the density and c is the specific heat capacity. Figure 5.2 schematically shows the temperature distributions in the sample of infinite-thickness for three times $t_1 < t_2 < t_3$.
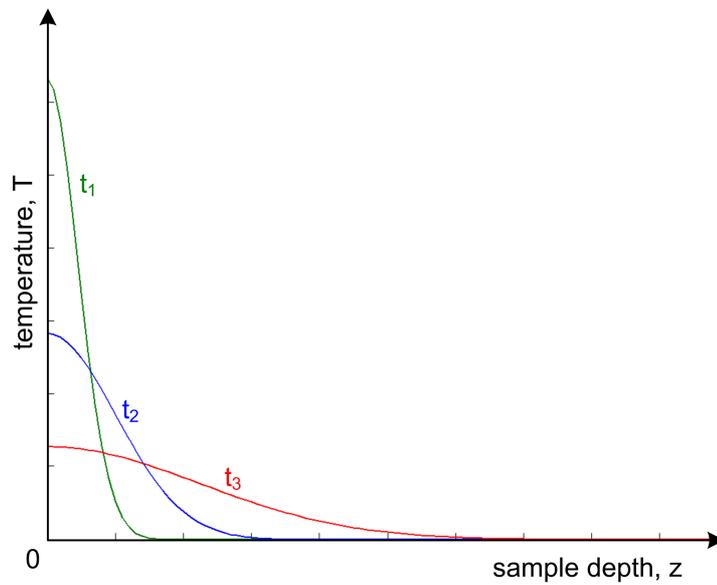
Figure 5.2: Temperature wave shapes in the defect-free
sample of infinite-thickness at the times t_1, t_2, t_3.

Now we consider the case of a plate shape sample with the thickness d assuming that the thermal pulse is fully reflected from the back surface. In this case the reflected thermal pulse comes back to the front surface of the sample increasing the temperature in comparison with the sample of infinite-thickness (see Figure 5.3).
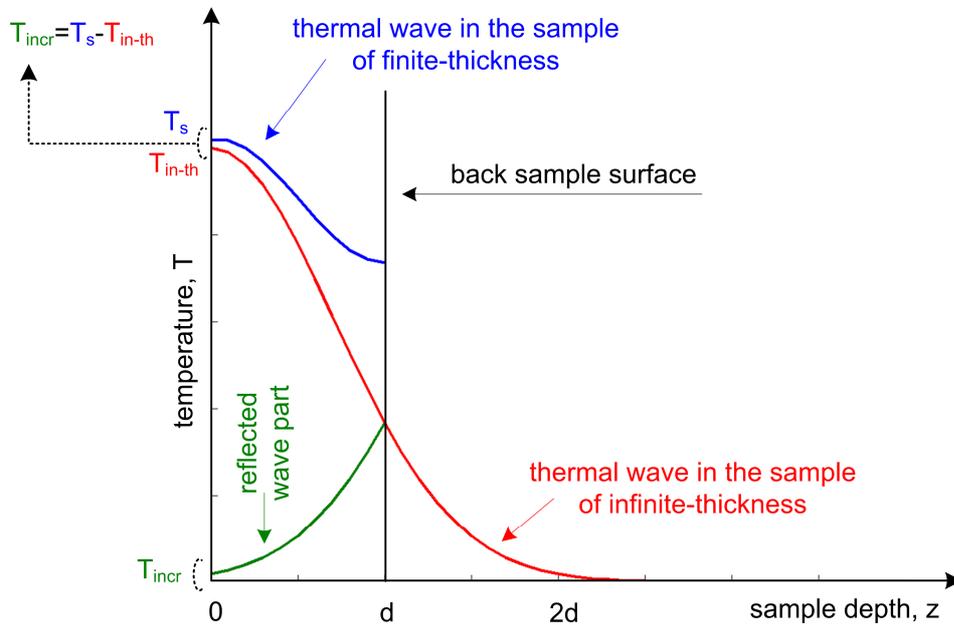
Figure 5.3: Temperature wave in the defect-free sample with thickness d.

This temperature increase T_{incr} at the time t_k corresponds to the temperature at the time t_k of the sample of infinite-thickness in the depth $2d$ as the reflected wave travels two ways: from the front surface to the back surface and from the back surface to the

front surface. According to the accepted assumption, the thermal wave fully reflects from the back sample surface at the depth d and goes back to the front surface. The reflected wave part is represented in the figure by the green curve. This reflected part additionally increases the temperature in the sample over the whole thickness range. Thus, the temperature distribution in the sample of finite-thickness (see the blue curve) is a sum of the original and reflected wave parts. Due to the reflected thermal wave part, the temperature on the front surface of the sample of finite-thickness at the time t_k is about T_{incr} higher than in the case of the sample of infinite-thickness.

Strictly speaking, we simplified the reflection process. In the ideal case, we have to consider the wave part from $2d$ going to the infinite depth (see the red curve). This wave part reflects at the time t_k from the front surface, goes to the back surface and so on (method of images). The multiple reflection process has a complex solution described in [75]. We ignore the higher order reflections of the smallest wave part as they do not significantly change the total temperature distribution in the early time range.

From the temperature increase T_{incr} at the time t_k the thickness of the sample can be found. To derive the equation for it, we consider the following: The front surface temperature $T_{in\text{-}th}(t_k)$ of the defect-free sample of infinite thickness is at $z=0$:

$$T_{in-th}(t_k) = \frac{Q}{2\sqrt{\pi}\sqrt{\lambda\rho c}\sqrt{t_k}} \quad . \tag{5.2}$$

As it was assumed, the temperature increase $T_{incr}(t_k)$ of the surface sample temperature of the thickness d is the temperature of the sample of infinite-thickness in the depth $2d$:

$$T_{incr}(t_k) = \frac{Q}{2\sqrt{\pi}\sqrt{\lambda\rho c}\sqrt{t_k}}\exp\left(-\frac{\rho c}{4\lambda t_k}\cdot(2d)^2\right) . \tag{5.3}$$

Now we introduce the relative temperature increase $T_{rel\text{-}incr}$:

$$T_{rel-incr}(t_k) = \frac{T_{incr}(t_k)}{T_{in-th}(t_k)} = \frac{T_s(t_k)-T_{in-th}(t_k)}{T_{in-th}(t_k)} \quad , \tag{5.4}$$

where $T_s(t_k)$ is the temperature on the front surface of the sample of which the thickness is extracted (see Figure 5.3). Substituting the variables $T_{incr}(t_k)$ and $T_{in\text{-}th}(t_k)$ from the equations above we have:

$$T_{rel-incr}(t_k) = \frac{T_{incr}(t_k)}{T_{in-th}(t_k)} = \frac{\frac{Q}{2\sqrt{\pi}\sqrt{\lambda\rho c}\sqrt{t_k}}\exp\left(-\frac{\rho c}{4\lambda t_k}\cdot(2d)^2\right)}{\frac{Q}{2\sqrt{\pi}\sqrt{\lambda\rho c}\sqrt{t_k}}} = \exp\left(-\frac{\rho c}{\lambda t_k}\cdot d^2\right) . \tag{5.5}$$

Then the sample thickness is:

$$d = \sqrt{-\frac{\lambda t_k}{\rho c} \cdot \ln\left(\left|T_{rel-incr}(t_k)\right|\right)} \ .$$ (5.6)

Thus, knowing the relative temperature increase the sample thickness can be computed.

The described method can be applied to extract the defect depth in different samples. For example, consider the case where the defect is a flat bottom hole. Over the flat bottom, the thermal wave reaches the defect and is reflected in a similar way as the wave reflects from the back side of the sample of finite-thickness. At an early point of time, the temperature increase caused by the back-drilled defect is similar to the temperature increase in the sample of finite-thickness described above. So the hole depth can be computed using the equation (5.6) originally derived for evaluating the thickness. At a later point of time, the lateral diffusion flows suppress this temperature increase on the defect area. The boundary between the early and late time periods is defined by the time when the thermal contrast between the non-defect area temperature and the temperature over the defect area reaches the maximum value. However, the equation (5.6) can be used only in the early time period.

Now we consider in detail how the depth of the flat bottom hole is extracted. First, the *relative thermal contrast curve* $C_{rel}(t)$ is computed:

$$C_{rel}(t) = \frac{T_s(t) - T_{defect-free}(t)}{T_{defect-free}(t)},$$ (5.7)

where $T_s(t)$ is the temperature on the defect area point, $T_{defect-free}(t)$ is the temperature on the defect-free area point (assumed to be pre-selected by an operator). To be precise, the equation (5.7) is known in PT as the running contrast (see Section 3.2). But in this chapter we use the term *relative* as it is better suited to the context and will be further transformed for experimental reconstructions (see Section 5.3).

The relative thermal contrast (5.7) has the same form as the relative temperature increase (Equation (5.4)) except that we use the temperature on the defect-free area instead of the temperature of the sample of infinite-thickness. Actually, it is very convenient and has a logical justification. When the wave in the defect area is reflected, the wave in the defect-free area goes further to the back surface as in the case of the sample of infinite-thickness. This fact allows us to substitute the temperatures. Analyzing the relative thermal contrast, if there is any deviation from 0 (temperature increase), the defect depth is computed by the equation (5.6). Note that in this case we use the value $C_{rel}(t_k)$ instead of $T_{rel-incr}(t_k)$. Theoretically, to get the most precise results of the depth extraction, it is necessary to define the deviation $C_{rel}(t_k)$ as early as possible when the lateral diffusion flows are weak. However, the detector noise (which is present in every measurement) limits the minimum value C_{rel}. To solve this problem, the detection of the deviation is performed by applying a threshold value *THR* which is chosen higher than the noise level. For example, when the thermal noise expressed in

relative thermal contrast is in the range of 0.01-0.015, the recommended value of the threshold *THR* is about 0.025. Figure 5.4 shows the extraction of time t_k in the noise thermal contrast schematically. In this way the depth of the flat bottom hole is extracted.
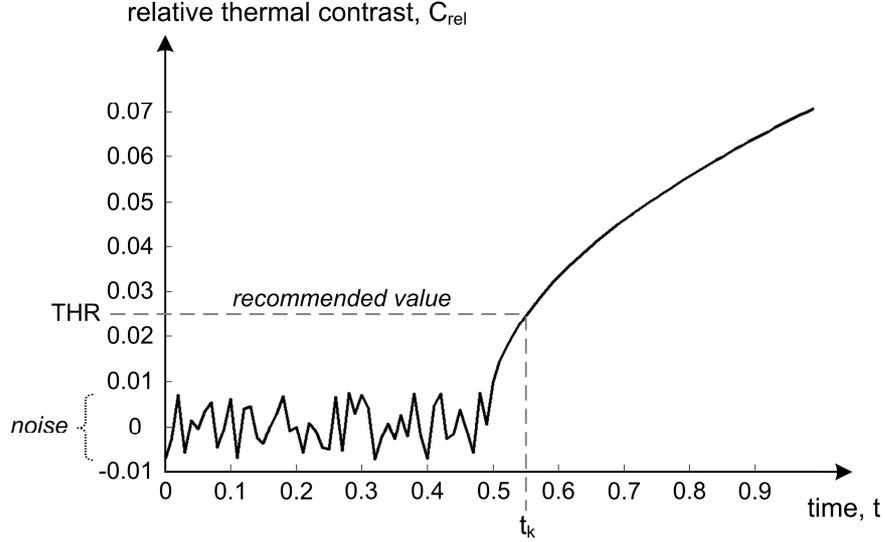
Figure 5.4: Extraction of the time t_k in the noise thermal contrast.

It is necessary to consider the lateral thermal flow effect. Suppose there is a flat bottom hole in a sample with the known thickness th_s. When we compute the depth for all points on the surface, we will notice that in some non-defect area points the extracted depth is greater than the sample thickness. This effect appears due to the lateral thermal flow coming from the defect area where the temperature is higher. In these points, at a certain time moment, the effect of the lateral flow makes a significant contribution to C_{rel} so that the points are marked as defective and the time t_k is extracted. The computed depth is greater than the thickness th_s because the entire temperature increase is caused by the lateral thermal flow instead of the back surface reflected wave. It is obvious that in such a case the defect depth has to be replaced by the sample thickness th_s.

Now we can give the precise definition of the *echo defect shape* (EDS) computed for the measurement *M* or the simulation *S*. We give the definition in the general form for a thermal distribution *TD* as the way of processing stays the same. Further, *TD=M* and *TD=S(i)* denotes the extraction of EDS from the measurement and from the simulation with number *i*, respectively. Note also that, to involve the space dependence, we redefine the relative thermal contrast C_{rel} given in Equation (5.7). The new contrast is denoted as C'_{rel}.

The *echo defect shape EDS(x,TD)* in the point *x* of the sample with the thickness th_s for the threshold value *THR* is computed in the following way:

1) The relative thermal contrast curve is computed by the equation:

$$C'_{rel}(x,t) = \frac{T_s(x,t) - T_{defect-free}(t)}{T_{defect-free}(t)} \quad , \tag{5.8}$$

where $T_s(x,t)$ is the temperature of the point x to be analyzed, $T_{defect\text{-}free}(t)$ is the temperature in the defect-free area. Both temperatures belong to the thermal distribution TD.

2) If a deviation exists in the computed relative contrast curve that is higher than the value THR then its time t_k is extracted (see Figure 5.4):

$$t_k(x) = \min\left\{ t \mid C_{rel}'(x,t) \geq THR \right\} \quad, \tag{5.9}$$

and the echo defect shape $EDS(x,TD)$ is computed as:

$$EDS(x,TD) = \sqrt{-\frac{\lambda t_k(x)}{\rho c} \cdot \ln\left(\left|THR\right|\right)} \quad, \tag{5.10}$$

where λ, ρ, c are thermal conductivity, density and specific heat capacity of the sample.

3) If there is no deviation higher than THR, or the computed defect shape in the previous step is higher than the sample thickness th_s, then the echo defect shape $EDS(x,TD)$ in this point equals th_s.

The defect shape correction unit uses the computed echo defect shape as the initial defect shape for the first simulation. Then, once the simulation has been computed, the unit analyzes and compares the temperature distribution from the source measurement with the unknown defect shape to that of the simulation with the known defect shape. Further, to refine the reconstructed defect geometry, the unit computes the difference between the echo defect shape of the measurement and the echo defect shape of the simulation, and adds the difference to the defect shape used in the last simulation. The correction criterion for an iteration i can be written as:

$$DS(x,S(i)) = \begin{cases} EDS(x,M) & for\ i=1 \\ DS(x,S(i-1)) + \left(EDS(x,M) - EDS(x,S(i-1))\right) & for\ i \geq 2 \end{cases} \quad, \tag{5.11}$$

where $DS(x,S(i))$ is the corrected defect shape which will be used for the simulation $S(i)$, $DS(x,S(i\text{-}1))$ is the defect shape used in the simulation $S(i\text{-}1)$, $EDS(x,M)$ and $EDS(x,S(i\text{-}1))$ are the echo defect shapes extracted from the measurement M and the simulation $S(i\text{-}1)$. The depth of some points in the refined shape $DS(x,S(i))$ can exceed the sample thickness th_s. Actually, this is caused by the fact that the echo shape contains accumulated thermal contrast due to both back sample reflection and lateral heat flow components. The defect shape correction unit checks all points in the refined shape $DS(x,S(i))$ replacing the depths with the sample thickness value th_s if they exceed it. The main reconstruction principle used in the algorithm is comparing the echo defect shapes of measurement and simulation. The echo defect shape, as was mentioned above,

contains accumulated information including back as well as lateral reflections. In this way, if we find the echo defect shape of a certain simulation which is equal to the echo defect shape of the inspected sample, it means that all internal back and lateral reflections in the simulation are also equal to reflections in the inspected sample. Consequently, the simulation has the same defect shape as the inspected sample. This concept constitutes a basis of the developed defect shape reconstruction algorithm. Notice that if the computed echo defect shapes of the measurement and the simulation are equal, the proposed correction criterion does not change the reconstructed defect shape. Now we show that the difference in echo defect shapes is an appropriate correction criterion.

The proposed correction criterion, namely, the difference of the echo defect shapes is explained as follows: Consider a sample having the corrosion shape shown in Figure 5.5. In this case the corrosion serves as the defect. We simulate a steel sample with a thickness of 5 mm in the 2D domain under PT conditions. After the simulation we computed its echo defect shape. It is shown in Figure 5.5 as a blue solid curve. Further, we simulate the sample with the corrosion shape represented by the blue solid curve. Again, the echo defect shape is extracted (see the blue dashed curve). We regard the first simulation as the measurement with unknown defect shape. The black solid curve is the actual defect shape and the blue solid curve is its echo defect shape. We regard the second simulation as the first iteration in the reconstruction. The blue solid curve is the simulated defect shape and the blue dashed curve is its echo defect shape.
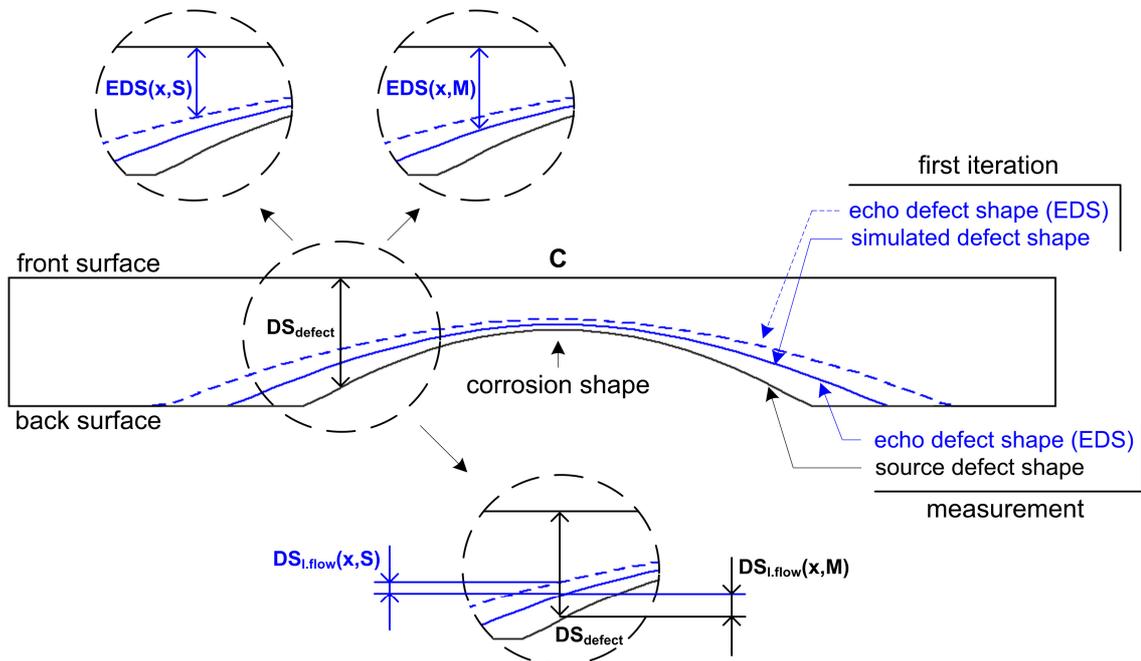
Figure 5.5: Scheme of a source defect shape and echo defect shapes.

The analysis of these results shows the following: The depth in the point C (the defect centre) on the front surface is extracted with good precision by using the echo defect shape method. But the evaluations of the depths in surrounding points are smaller than the actual depths. This is caused by a lateral thermal diffusion flow from the defect

centre to the sample corners. This flow additionally increases the temperature on the sample surface. At a certain point in time in a certain defect point the total temperature due to this lateral flow and due to the wave reflected from the defect (or the back sample surface) is higher than the threshold value *THR* so the echo defect shape method detects the defect and extracts its probable depth. We propose to approximate the lateral flow influence in linear form. For example, in the point *x* the echo defect depth $EDS(x,M)$ in the first simulation (regarded as the measurement) is:

$$EDS(x,M) = DS_{defect}(x,M) - DS_{l.flow}(x,M) \; , \qquad (5.12)$$

where $DS_{defect}(x,M)$ is the actual defect depth, $DS_{l.flow}(x,M)$ is the reduced depth value due to the lateral flow.

In the iterative reconstruction process, the echo defect depth $EDS(x,S)$ of a certain simulation *S* is:

$$EDS(x,S) = DS(x,S) - DS_{l.flow}(x,S) \; , \qquad (5.13)$$

where $DS(x,S)$ is the defect depth used in the simulation *S* (in the first iteration $DS(x,S) = EDS(x,M)$), $DS_{l.flow}(x,S)$ is the reduced depth value due to the lateral flow. Further, we assume that the original defect shape and the defect shape used in the simulation are close, consequently, the lateral flow influences are also close: $DS_{l.flow}(x,M) \approx DS_{l.flow}(x,S)$. Taking this into account one can combine the equations (5.12) and (5.13):

$$DS_{defect}(x,M) - EDS(x,M) \approx DS(x,S) - EDS(x,S) \; . \qquad (5.14)$$

Then, to approach the actual defect depth, we compute the depth as:

$$DS_{defect}(x,M) \approx DS(x,S) + (EDS(x,M) - EDS(x,S)) \; . \qquad (5.15)$$

The closer the lateral flow influences are $DS_{l.flow}(x,M) \approx DS_{l.flow}(x,S)$, the closer to 0 is the difference of echo defect shapes ($EDS(x,M) - EDS(x,S)$). Applying this concept to the iterative reconstruction principle, the equation is transformed into the following form:

$$DS(x,S(i)) = DS(x,S(i-1)) + (EDS(x,M) - EDS(x,S(i-1))) \; , \qquad (5.16)$$

where $DS(x,S(i))$ is the defect depth that will be used in the simulation *S(i)*, $DS(x,S(i-1))$ is the defect shape used in the simulation *S(i-1)*, $EDS(x,M)$ and $EDS(x,S(i-1))$ are the echo defect shapes extracted from the measurement *M* and the simulation *S(i-1)*. In this way, converging the echo shape of the simulation to the echo shape of the measurement, the simulated defect shape *DS* is approaching the real defect shape DS_{defect}. We tested the reconstruction approach in many cases using the forward solver for generating the source measurement data as well as for its reconstructions. Some test

cases are considered in Section 5.2. The proposed approach demonstrated robust reconstruction results. Summarizing the described background, the defect shape correction criterion proposed in the equation (5.11) is proven.

In the end of this section we emphasize that the reconstruction is carried out iteratively. As the initial defect shape the algorithm uses the echo defect shape of the measurement. In the iterative reconstruction process, the algorithm corrects the reconstructed shape using the echo defect shapes. The necessary number of iterations depends on the defect shape and lies in the range from 2 to 9. As a particular example, a sample with simulated corrosion shown in Figure 5.5 can be reconstructed in two iterations with satisfactory precision.

Note: The presented approach allows the time range in which the test sample model is simulated to be defined precisely. The time boundary is derived from equation (5.6) substituting the known non-defect sample parameters (thermal properties, sample thickness) and the reconstruction parameter *THR*. The time boundary t_{end} of the simulation is expressed as:

$$t_{end} = -\frac{(th_s)^2 \rho c}{\lambda \ln(|THR|)} \,, \qquad\qquad (5.17)$$

where th_s is the sample thickness; λ, ρ, c are thermal conductivity, density and specific heat capacity of the sample, respectively; *THR* is the threshold value used in the reconstruction. Actually, this is very convenient as redundant computations are avoided, decreasing the computation time for the simulations. For example, if *THR* is equal to 0.018 then the time boundary t_{end} for an aluminium sample with a thickness of 5 mm is 0.064 seconds and for a PVC sample 54.961 seconds. As seen, the time difference is significant. This should be taken into account when the simulation model is created.

5.1.2 Simulation unit

The unit simulates the thermal conduction process during the pulsed thermography experiment. Ideally, we can also simulate radiation and convection processes in PT experiments but their influences are too small so they are neglected. Simulating the thermal conduction process the unit uses any of the numerical methods (FEM, FDM or BEM). A short review of these was given in the previous chapter (as stated in this chapter, for this work, a commercial FEM solver has been used). Here we only pay attention to the main parameters in such simulations. These are: *heat excitation time and energy, thermal properties of the inspected sample and the defect, sample geometry.* Prior to any reconstruction, it is recommended that the sample simulation model is verified against the PT experiment. For this purpose, a sample with known defect shape can be used. One can compare its measurement and its simulation results using the relative thermal contrast. If there is any discrepancy, it is necessary to find the sources

and correct them (for example, deviations in thermal properties or poor meshing). The developed algorithm provides precise reconstruction results only if there is qualitative and quantitative correspondence of the measurement and its simulation.

5.1.3 Sequence of actions in the reconstruction algorithm

In order to summarize the algorithm description and show the structure in clear form, we present a diagram containing the sequence of actions during the reconstruction. In this diagram the following abbreviations are used: *RDS* is the reconstructed defect shape, *Echo_Defect_Shape(X)* is the function which extracts the echo defect shape from *X*, *M* is the measurement with unknown defect shape, *S* is the computed simulation, *Simulation(X)* is the function which computes the sample simulation with the defect shape *X*, *Correction(X)* is the function which corrects the shape *X* where the depths exceed the sample thickness, *I* is a counter of iterations, *N* is the number of iterations in the reconstruction. The algorithm performs commands in the order shown in Figure 5.6.
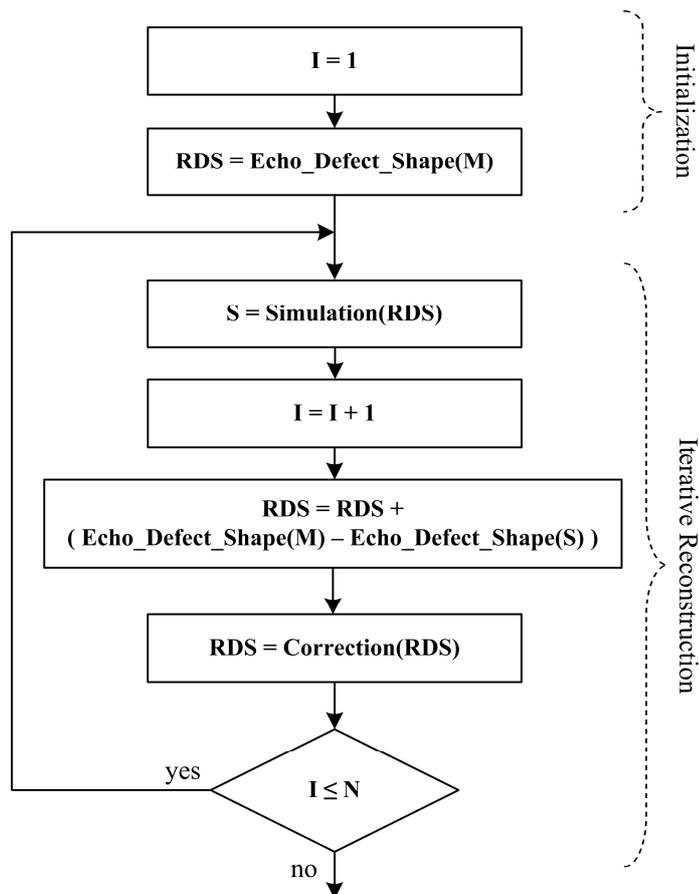
Figure 5.6: Sequence of actions during the reconstruction.

5.2 Reconstructions of simulated defects

As being said above, the developed algorithm was initially tested in the simulation mode when thermal response from the source defect shape and its reconstructions are computed by simulations. It allowed the reconstruction core to be examined. The results obtained proved the robustness of the defect shape correction criteria used in the algorithm.

First, we illustrate the reconstruction of the corrosion shape in the steel sample (λ=14.2 W/mK, ρ=7978 kg/m^3, c=480 J/kgK) shown in Figure 5.5. The sample has a thickness of 5 mm and length of 100 mm. The thermal excitation of the sample is performed with the heat flux density $f_{front(a)}^{q}$ =945 10^3 W/m^2 acting for t_{ex}=0.01 s. The threshold value *THR* was set to 0.018. In the following Figures (5.7.1-5.7.3) we use black colour to depict the source sample profile and blue colour for current reconstructions. The solid curves show defect shapes and the dashed curve shows echo defect shapes. The red curve depicts the reconstructed profile which is passed to the next iteration.
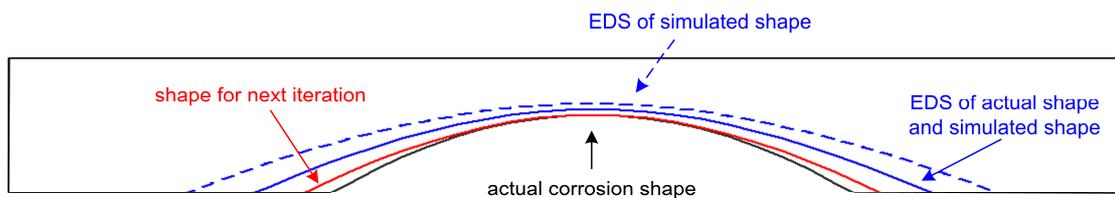
Figure 5.7.1: Reconstruction in the first iteration.
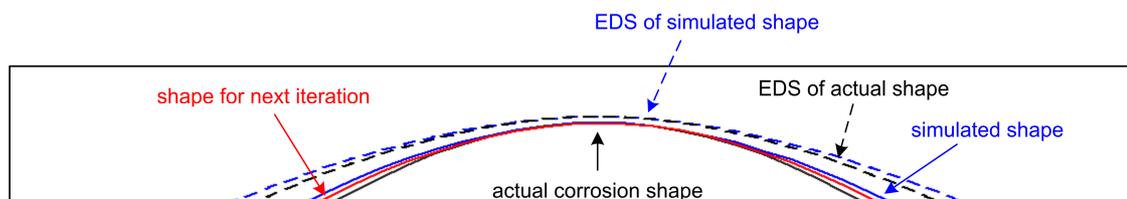
Figure 5.7.2: Reconstruction in the second iteration.
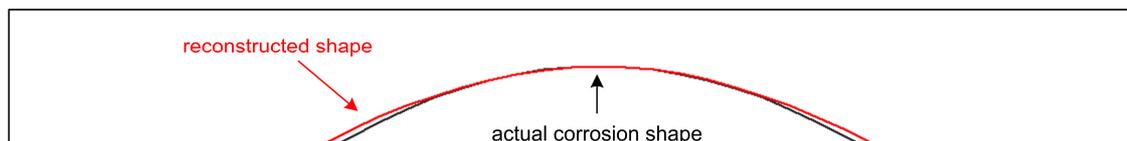
Figure 5.7.3: Reconstruction results.

As seen from the figures above, the reconstructed defect shape approached closely the actual defect shape.

In the second case, we reconstructed the corrosion shape z_1 (see Section 3.6) that was considered in [10]. Note that the analysed sample has a unit thermal diffusivity (α=1 m^2/s). The two iteration reconstruction process is shown in Figures (5.8.1-5.8.3). Since the source shape is stretched for better visualisation, the auxiliary coordinate axes are given.
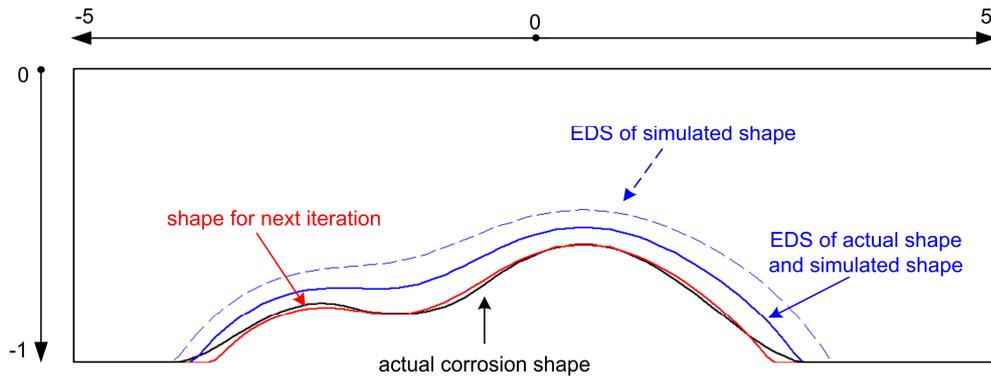
Figure 5.8.1: Reconstruction in the first iteration.
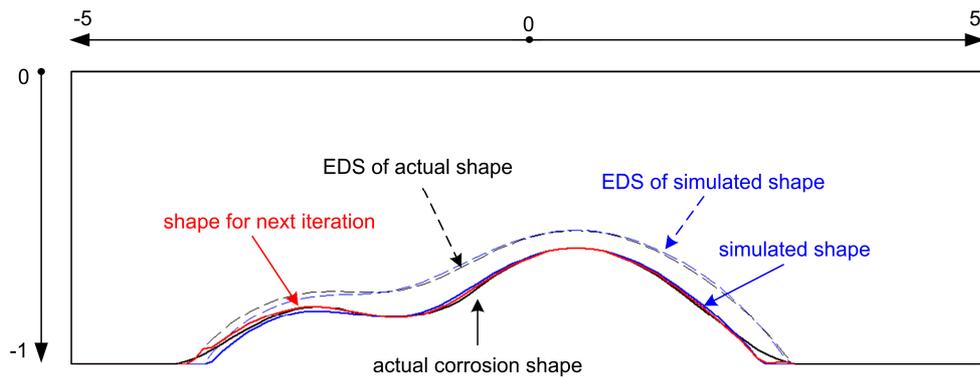
Figure 5.8.2: Reconstruction in the second iteration.
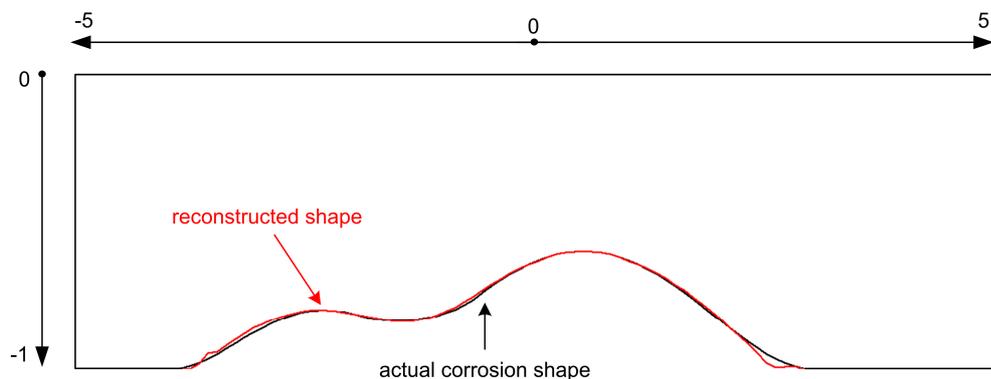
Figure 5.8.3: Reconstruction results.

Again, the developed algorithm reconstructed the source profile with satisfactory precision.

In the third case, the corrosion shape z_2 (see Section 3.6) analysed also in [10] was reconstructed. The five iteration reconstruction is shown below (Figures 5.9.1-5.9.3).
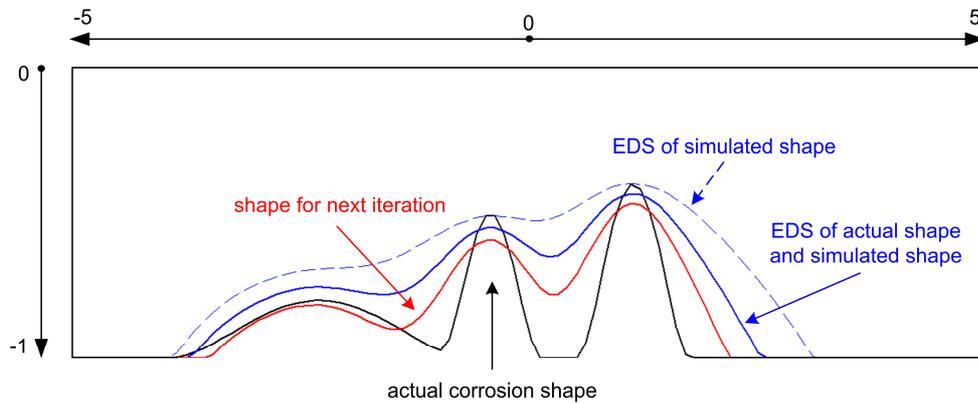
Figure 5.9.1: Reconstruction in the first iteration.
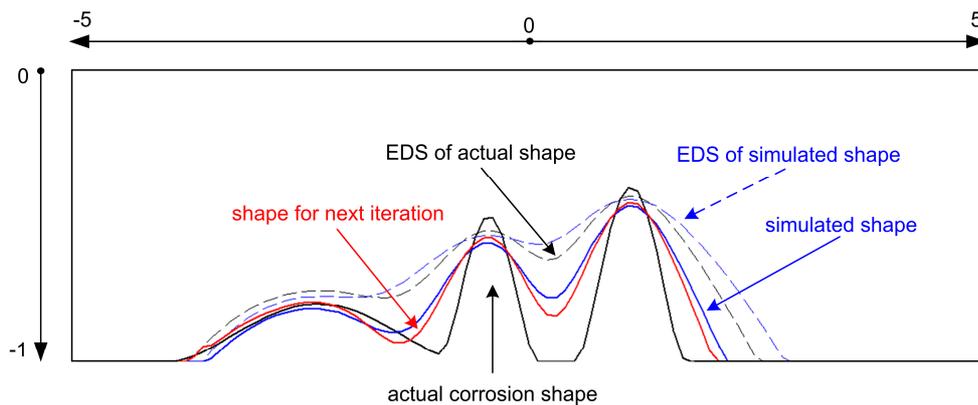
Figure 5.9.2: Reconstruction in the second iteration.
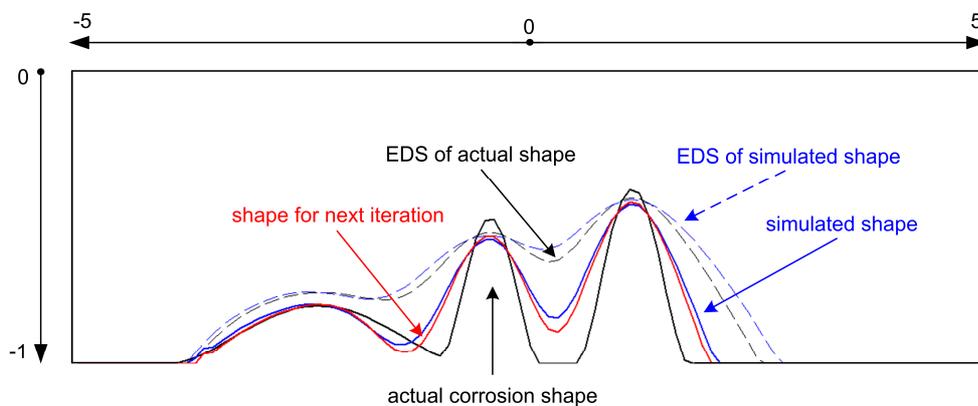
Figure 5.9.3: Reconstruction in the third iteration.
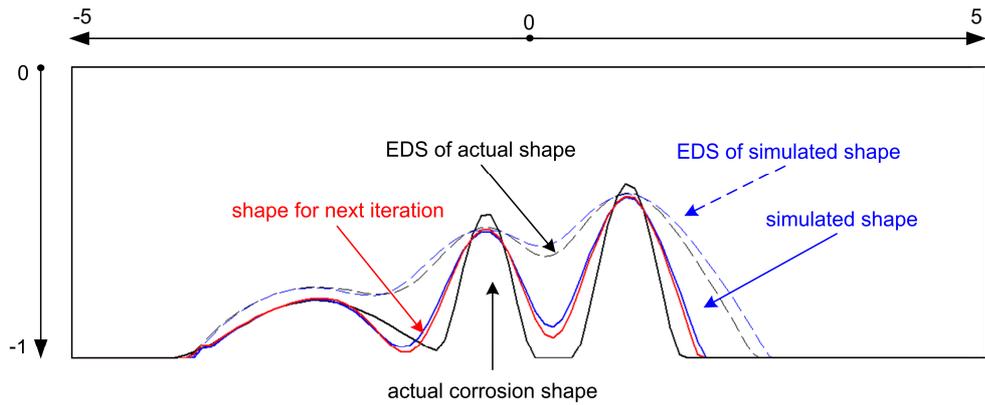
Figure 5.9.4: Reconstruction in the fourth iteration.
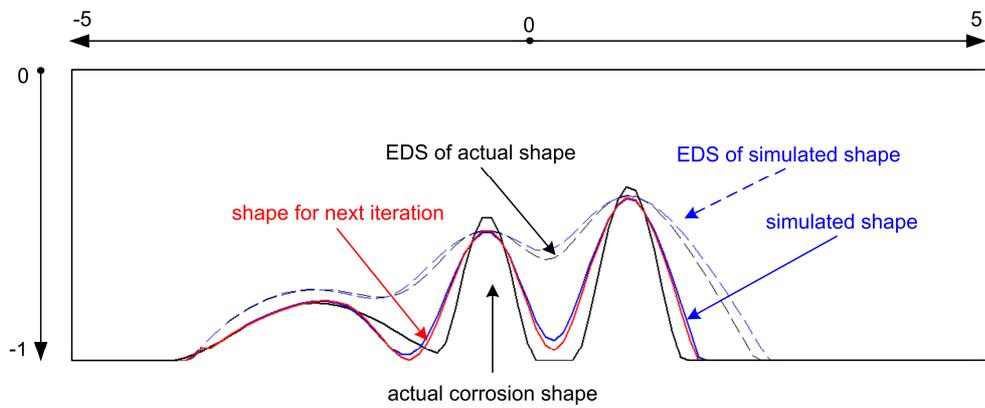
Figure 5.9.5: Reconstruction in the fifth iteration.
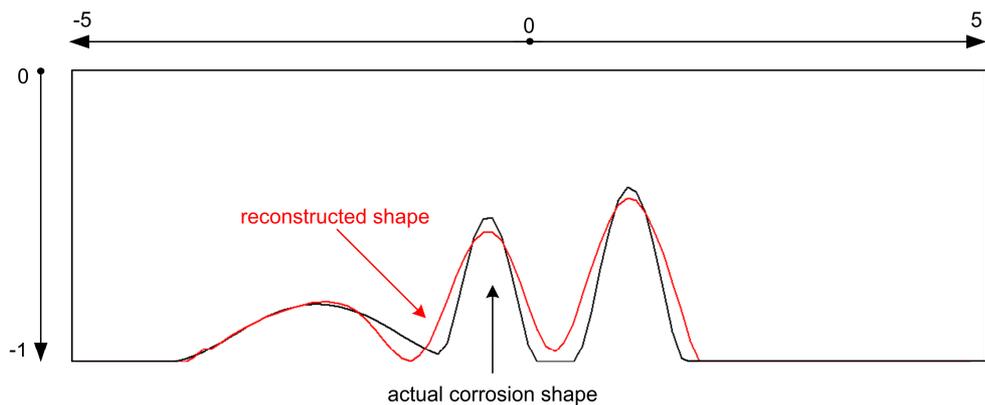
Figure 5.9.6: Reconstruction results.

The presented case is remarkable. The shape lies on the boundary of detectability in PT [57] and, consequently, it causes the low rate of convergence. We demonstrated this case in order to differentiate between the claims to the reconstruction algorithm and the PT limits. Of course, no reconstruction method can go beyond the physical limitations.

In this section we tested the developed algorithm in the simulation mode. The reconstructed defect shapes are close to their actual forms. Further we discuss the reconstruction under practical conditions.

5.3 Defect shape reconstruction based on experimental data

The reconstruction of the defect shape under real experimental conditions involves some unfavourable effects due to factors such as strong thermal noise, uneven heating and defect camera pixels. In this section we describe their sources and propose methods to suppress these effects.

Thermal noise: The thermal noise is inherent to any measurement. When a single image is considered, one can notice abrupt value changes of the temperature between neighbouring pixels. This noise is effectively suppressed by a smoothing filter [76,77]. The recommended filter sizes are 3 and 5 pixels.

Uneven heating: Uneven heating is a common problem in pulsed thermography. It happens when the sample surface is not illuminated uniformly by a heat source. This non-uniform heating is caused by the radiation pattern of the heat source and by the variable distance from the sample surface points to the heating source. Furthermore, for example, when testing curved turbine blades, inhomogeneous illumination due to the shape of the test object will be unavoidable. We propose a solution that involves the measurement of an additional defect-free sample: After the measurement of the sample with an unknown defect shape the IR camera and the heat source remain in the same positions. Then a reference sample without defect, made of the same material and having the same geometry sizes, is measured. The relative thermal contrast defined in the equation (5.8) above is transformed into the following equation:

$$C'_{rel}(x,y,t) = \frac{\left(T_s(x,y,t) - T_s(x,y,t_0)\right) - \left(T_{ref.s}(x,y,t) - T_{ref.s}(x,y,t_0)\right)}{T_{ref.s}(x,y,t) - T_{ref.s}(x,y,t_0)}, \qquad (5.18)$$

where x,y are pixel coordinates, t is the time, $T_s(x,y,t)$ is the temperature of the sample with unknown defect shape in the point x,y at the time t, $T_s(x,y,t_0)$ is the temperature of the sample with unknown defect shape in the point x,y before thermal excitation, $T_{ref.s}(x,y,t)$ is the temperature of the reference (defect-free) sample in the point x,y at the time t, $T_{ref.s}(x,y,t_0)$ is the temperature of the reference sample in the point x,y before thermal excitation. This method allows undesirable uneven heating to be suppressed with high precision.

Defect camera pixels: Defect pixels (e.g. occurring during ageing of some IR detector types) provide false temperature values in the observation area. It is obvious that such pixels have negative influence on the reconstruction process so they have to be eliminated. A simple and effective solution is a median signal filtering [76,77]. Every grabbed IR camera image is filtered by a median filter that eliminates the defect camera

pixels and suppresses the impulse noise. Recommended median filter sizes are also 3 and 5 pixels.

In summary, every measurement is prepared in the following order: 1) median filtering; 2) smoothing filtering; 3) relative thermal contrast computation with uneven heating compensation. Once the measurement has been processed in this way, the reconstruction algorithm can be applied.

5.4 Experimental defect shape reconstruction results

The developed reconstruction algorithm was tested under laboratory conditions. For this purpose, a sample having a known, well defined 2D corrosion shape was made of stainless steel (V2A, λ=15 W/mK, ρ=8000 kg/m^3, c=477 J/kgK) (see Figure 5.10). A corrosion-free reference sample was produced in the same way. Both samples had the following parameters: *length* – 100 mm*, width* – 100 mm*, thickness* – 5 mm. Their photographs appear in Appendix E. Like most metals and alloys the steel reflects a significant amount of light energy if it is excited by flash lamps. In order to increase the optical absorption coefficient, the front surface of the sample was coated with a thin black layer of paint. We discussed this technique and its properties in Section 4.5. In the reconstruction algorithm we ignore the information in the time range from 0 to 15 ms after the excitation, only the information after 15 ms is analyzed. There are two reasons for doing this. The first one is that our sample simulation model does not contain any thin coating on the front surface. Theoretically, it is possible to simulate the thin coating too, but it will be a time consuming simulation as the coating is extremely thin (about 5-9 µm) and, consequently, a very fine mesh has to be used in the sample model. The second reason is that we coated both samples in our laboratory manually using a typical spray can. If it is done manually, even with precise hand movement, the discrepancies of the coating thickness between the corroded and non-corroded sample can amount to 4 µm. Because of that, the relative thermal contrast (see Equation (5.18)) can show oscillations in the time range from 0 to 15 ms. The easiest way to overcome the problem is to analyse the data after that time, which is what we did.
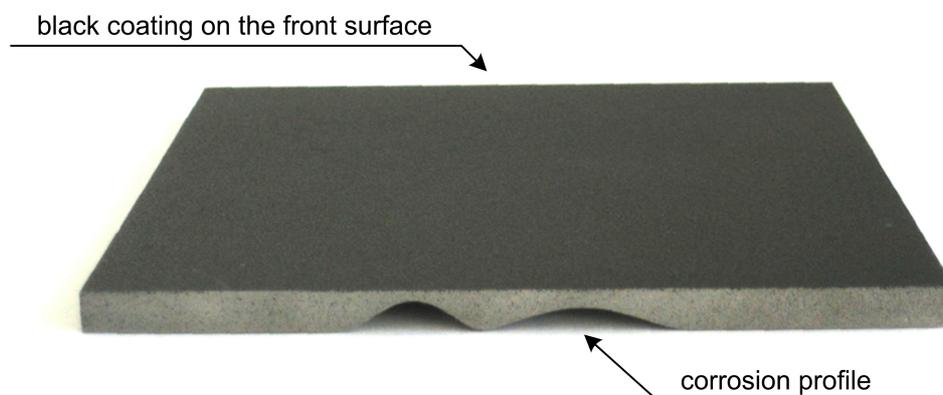
Figure 5.10: Photograph of the steel sample with artificially machined corrosion shape.

After the sample preparations, the PT measurements were carried out with the following parameters: the image acquisition rate was 10 ms, the number of images was 300, the approximated heating time was 10 ms. Then the measurements were filtered by the median filter and the smoothing filter. The filter sizes were 5 pixels in both cases. Further, the relative thermal contrast was computed for all points. Note that our measurement setup had only a single flash lamp placed on one side of the IR camera (see Appendix D) with the result of strong uneven heating. The developed method successfully suppressed the effects of uneven heating. Then data for a single line across the corrosion shape were extracted and used for the reconstruction. The threshold *THR* applied in the reconstruction was 0.05. The developed algorithm reconstructed the defect shape with satisfactory precision. The three iterations of the reconstruction process are shown in Figure 5.11. The solid curves show the actual shape, the dotted curves are the reconstructed shapes.

(a) – before the iterative reconstruction

(b) – after the first iteration

(c) – after the second iteration

(d) – after the third iteration
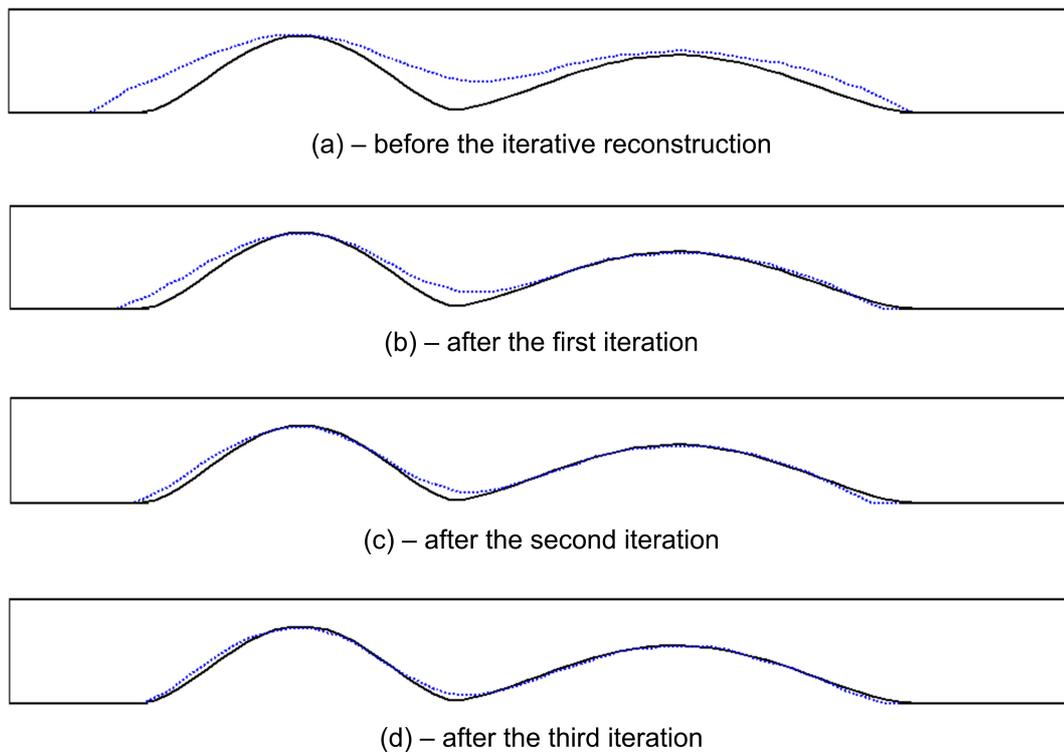
Figure 5.11: The corrosion shape reconstruction process in the steel sample.

The source shape consisted of two rounded grooves with different slopes at the edges modelling corrosion. The right groove was less slanted and induced weak lateral thermal flows. Its reconstruction took one iteration. During second and third iteration the shape did not change significantly. The left groove was more slanted and, consequently, induced stronger lateral flows. The reconstruction took three iterations to approach the actual groove shape. The presented reconstruction was carried out using a commercial finite element solver installed on a state-of-art PC (Pentium 3.06 GHz, 512

MB RAM). The mesh model included about 5500 finite elements. The reconstruction with three iterations took 3 minutes.

The algorithm turned out to provide robust reconstruction results from experimental data. This fact proves the correctness of the used defect shape refining criterion.

Note: In addition, we point out that the reconstruction algorithm can even be applied in cases where some assumptions for the defect shape (smoothness) are not fulfilled. For example, reconstructions of simulated rectangular grooves demonstrated that the upper-width of the reconstructed defect shape is close to the actual defect width and the reconstructed depth in the defect centre equals to the actual groove depth. In particular, Figure 5.12 shows the reconstructed shape of the simulated rectangular groove in the steel sample (*sample thickness* – 5 mm*, groove width* – 10 mm*, groove depth* – 3 mm), the black solid curve is the actual groove shape and the blue dotted curve is the reconstruction.

Figure 5.12: Reconstruction of a rectangular groove.

5.5 Algorithm extensions

In some practical cases, where the inspected samples are coated by black paint, the thermal pulse reflected from the defect can reach the front surface of the sample influenced significantly by the coating. It happens in samples made of aluminium or any high conductive materials that are of practical meaning. Thus, the echo defect shape should be computed in these circumstances. Theoretically, the coating can be added in the sample model. However, as it was mentioned above, the coating thickness can vary across the sample and may be different in the reference sample. One can also increase the value *THR* used for the reconstruction but it leads to a risk that deep defects, that induce only slight thermal perturbations, will not be detected. To solve the problem, we propose the followings technique:

- The measured data are not processed until the time t_{st} when the thermal coating influences become negligible everywhere on the sample surface. Let $IM(t_{st})$ be the thermal image measured at the time t_{st}.

- The relative thermal contrast for the image $IM(t_{st})$ is computed. Then, the points in which the temperature is higher than the predefined threshold value

THR (applied for the reconstruction) are processed by equation (5.10). Instead of the constant *THR* the current relative thermal contrast value is used. This principle is shown in Figure 5.13.

Basically, we extract the echo defect shape partly only for points with temperatures higher than the threshold value *THR* used for the reconstruction.

- Other points (which are lower than the threshold value *THR* in the image $IM(t_{st})$) should be processed in the standard way (see the definition EDS).

image IM(t_{st})

$$D_1 = \sqrt{-\frac{\lambda t_{st}}{\rho c} \ln(|T_1|)}$$

$$D_2 = \sqrt{-\frac{\lambda t_{st}}{\rho c} \ln(|T_2|)}$$
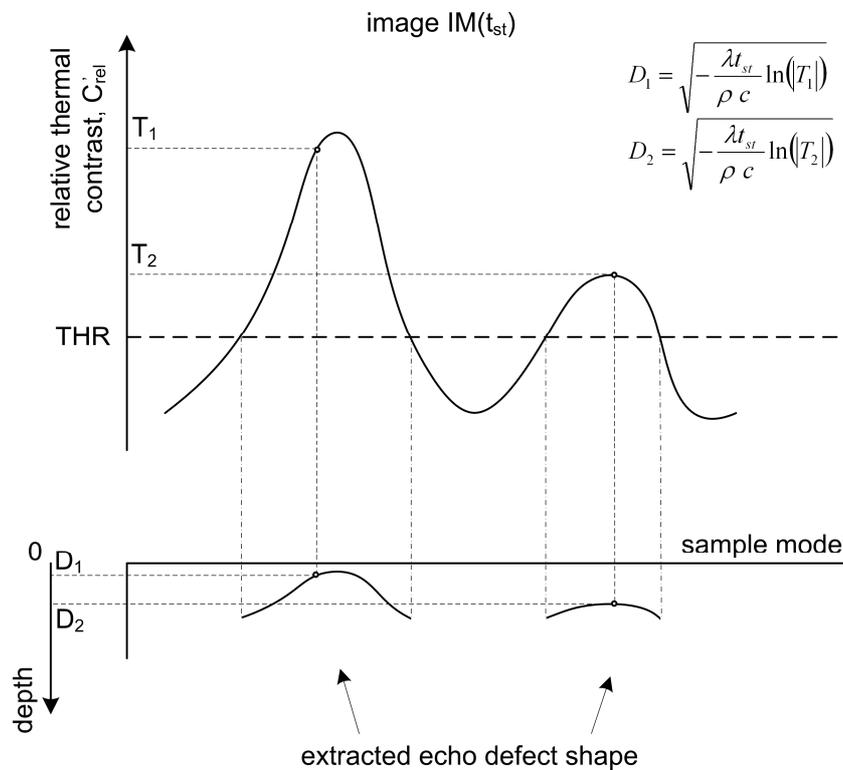
Figure 5.13: Extraction of the echo defect shape from the image $IM(t_{st})$.

The measurement and its simulation are processed in this way. The time t_{st} in the simulation should be equal to t_{st} when processing the measurement. This method allows echo defect shapes to be obtained, preserving sensitivity where it is possible. Note that sensitivity affects the reconstruction precision. The rest of the developed algorithm stays the same.

We tested the algorithm in the simulation mode. The proposed technique demonstrated robust results.

5.6 Conclusion

A new algorithm for defect shape reconstruction was developed. As a unique feature of the algorithm we combined the approach of one-dimensional defect depth extraction with 2D (or 3D) simulations of a pulsed thermography measurement. This combination allows the reconstruction of complex defect shapes in samples thus extending application opportunities for PT. The developed algorithm was tested using experimental data with robust results of the reconstruction of a 2D reference corrosion steel sample.

Chapter 6

Data compression in pulsed thermography

The second problem posed in this work is the development of methods for effective PT data compression. The original PT data stored in raw format consumes a significant amount of storage space. However, PT data can be efficiently compressed. Basically, this problem is similar to video data compression that was studied and numerous solutions have been proposed [78,79]. The best known video codecs nowadays are DivX (MPEG-4) and H.263. It will be reasonable to apply them for compression of PT data too. However, free available versions are designed for the conventional colour (24 bits per pixel) and grey (8 bits per pixel) formats. As noted in Chapter 2, the IR camera provides 16 bits pixel digitalization. That is why direct compression is impossible. At the same time, the codecs include additional elements like a motion compensator which are unnecessary for PT data.

We present lossy and lossless compression approaches to this problem and compare results with an existing method known in PT. Here, we point out that our aims are to analyse and to transform data based on features characteristic to pulsed thermography as an extension to existing algorithms in order to get high compression ratios. For a lossy approach, we decided to apply a pure image compression algorithm (JPEG2000) for compression of the PT image sequence in a specific way. We chose this algorithm only because of its high compression ratio and high quality in data reconstruction. Note also that we critically compared our proposed method with DivX (in grey format mode). Our method demonstrated better quality in reconstruction at equal compression ratio. For the lossless method, we propose to combine a conventional compression algorithm (ZIP) with a particular data transformation, which increases the compression ratio. Both methods were tested on typical experimental thermography data. The achieved compression ratios are significantly higher than those of existing algorithms.

6.1 Introduction

First, we briefly mention the raw format in which the equipment stores information. An IR camera that is used for PT has a certain temperature range (for example, from -10 °C up to 100 °C). The range is digitized with 16 bits accuracy (digital discretization), the image size is 256 x 256 pixels. According to these

characteristics the size FS_{raw} of the image sequence comprising S images (in raw format) is computed as:

$$FS_{raw} = N \cdot (256 \cdot 256) \cdot 2\,bytes$$

(for example, if N=200 then FS_{raw}= 25 MB)

Due to the signal characteristics of the image sequence, the raw data contain a significant amount of redundant information. As the thermal response of the inspected sample may be described as a diffusion process, the whole sequence will always change smoothly over time, i.e., the temperature of any chosen location will not change to a significant amount between adjacent frames. Based on this property, we propose two compression methods for PT data. Note that, in general, there are two types of data compression: lossless compression and compression with slight losses (the latter being frequently used for the storage of images as well as audio and video data). Both paths are pursued in this work.

6.2 Raw measurement data format

Prior to the description of the methods, the raw data format (Figure 6.1), as provided by the PT equipment, is considered. During the measurement the IR camera generates a sequence of N images, each image having the same size (LxK pixels), where each image pixel is represented by a word of 16 bits. The whole sequence is stored on a media device as a single file. Further, in this chapter we use the abbreviation $IM_{raw}(i,j,t)$ to refer to the IR value at the point i,j ($1 \leq i \leq K$, $1 \leq j \leq L$) at the time t ($1 \leq t \leq N$). To avoid misunderstanding, we should point out that the symbol IM used previously represents the same data set but converted into the temperature scale by the calibration curve (see Section 2.2). As in most cases the measurement is stored in the raw data format, the compression algorithms are described for the raw data.
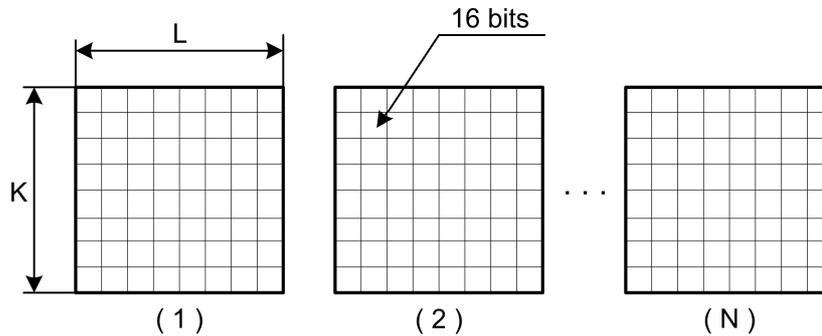
Figure 6.1: Raw data format.

6.3 Lossy data compression

In this section we briefly describe an existing lossy compression method (TSR) and emphasize its advantages and disadvantages. Then we present our own solution of the problem and compare them. At the end of the section we also make some critical remarks related to the proposed method.

6.3.1 Time signal reconstruction (TSR) method

To estimate the efficiency of the method proposed in the following, its results will be compared with the results of the time signal reconstruction (TSR) method [18,19,23,43,49,80] that was especially developed for pulsed thermography. The method is briefly described in the following paragraphs.

Prior to the method description, we consider some theoretical aspects concerning heat diffusion. A solution for the surface temperature $T(t)$ of a one-dimensional heat diffusion equation for a defect-free, surface absorbing half-space sample after delta pulse heating has the following form (see Equation (3.6)):

$$T(t) = \frac{Q}{2e_s \sqrt{\pi t}} \; , \tag{6.1}$$

where T is the temperature on the sample surface, Q is the input energy density and e_s is the thermal effusivity of the sample. The transformation of Equation (6.1) into the logarithmic domain is beneficial as the solution in this domain will represent a straight line with a slope of -0.5, independently of the sample properties:

$$\ln(T(t)) = \ln\left(\frac{Q}{2e_s}\right) - \frac{1}{2}\ln(\pi t) \; . \tag{6.2}$$

It is necessary to note that, in practice, the cooling curve in the logarithmic domain will not be a perfectly straight line. It is illustrated in Figure 3.6. The curve deviates from its ideal performance due to thermal wave reflections originating from the back side of the inspected sample or from any inclusion contained in the sample. The main idea proposed by the authors in [18] lies in a transformation of the cooling curve into the logarithmic domain and its approximation by a polynomial:

$$\ln(T(t)) = a_0 + a_1(\ln(t)) + a_2(\ln(t))^2 + a_3(\ln(t))^3 + a_4(\ln(t))^4 \; , \tag{6.3}$$

where $T(t)$ is the temperature at a point on the sample surface at the time t.

The polynomial (6.3) contains low-order coefficients a_0, a_1 to reflect changes that are inherent to defect-free, infinite samples (Equation (6.2)) as well as high-order

coefficients a_2, a_3, a_4 that are used to describe smooth non-linear changes caused by thermal reflections (from any inclusions or from the back side).

The TSR method has some advantages, but also some disadvantages. One of the advantages is low storage cost that is independent of the number of images in the sequence. To store single pixel data, we need at least 20 bytes (5 coefficients, each coefficient takes 4 bytes for *single precision* or 8 bytes for *double precision*). Due to the fact that the temperature evolution in a single pixel is kept in the polynomial form the method allows analytical manipulations, straightforward data reconstruction and derivative computations. It is also worth pointing out that the TSR method suppresses the noise significantly. The main disadvantage is that the cooling curve can exhibit a certain time related behaviour which can not be approximated with satisfactory accuracy by the polynomial (6.3). In consequence, the polynomial approximation will distort the real data.

The TSR method serves as a reference for the algorithm proposed in the following section.

6.3.2 Space/time mapping JPEG-based data compression

The world-wide spreading of digital devices causes a fast evolution of the numerical algorithms they use. The best known data storage algorithms which have gained world-wide popularity are MP3 (audio), JPEG (image) and MPEG (video). Those algorithms transform data into the frequency domain, extract the most relevant coefficients and store them in a compact form. This similarity, in consequence, involves the disadvantage of higher losses when information changes abruptly with time (MPEG) or with space (MPEG, JPEG). That being said, we chose to apply the JPEG2000 compression algorithm in a special manner, such that it compresses data changing in time as well as in space. However, note that this approach requires a specific space/time representation of dynamically changing data as a single image to be further compressed.

In order to compress the raw data, the algorithm performs three steps:

1) *Extraction of the dynamically changing part of the data*
   In this step the algorithm reduces redundancy in the raw data.

2) *Space/time mapping*
   The dynamically changing sequence of images is represented as a single image with smooth local changes.

3) *JPEG compression*
   The algorithm JPEG2000 compresses the obtained smooth image.

These steps will be described in detail now.

6.3.2.1 Dynamic part extraction

In the first step the algorithm reduces redundancy in the raw data. This redundancy lies within the number of bits used to represent temperature values (in the following discussion, for simplification, we speak of "temperature" instead of the IR radiance captured by the camera).

A typical focal plane array camera offers a 14 or 16 bit digital output signal, where the discretization steps are well adapted to the noise equivalent temperature difference (NETD) of the camera. In many practical testing situations, 256 levels are sufficient to cover the contrast in any frame of the sequence. Based on this, to extract the dynamically changing data portion, the algorithm performs the following steps:

1) For each image t in the sequence the maximum and minimum IR values (denoted $IM_{MAX}(t)$ and $IM_{MIN}(t)$ respectively, where $1 \leq t \leq N$) are extracted and stored separately. This couple of values identifies the range of all temperatures which occur in the respective image.

2) Using $IM_{MAX}(t)$ and $IM_{MIN}(t)$, the temperature variations IM_{raw} of each image are coded by values IM_{tr} in the range 0-255 as shown in Figure 6.2. There exists a simple linear relation between the range $IM_{MIN}(t)$ - $IM_{MAX}(t)$ and the range 0-255. The integer value IM_{tr} is computed as:

$$IM_{tr}(i,j,t) = \frac{255}{\left(IM_{MAX}(t) - IM_{MIN}(t)\right)} \cdot \left(IM_{raw}(i,j,t) - IM_{MIN}(t)\right) \qquad (6.4)$$
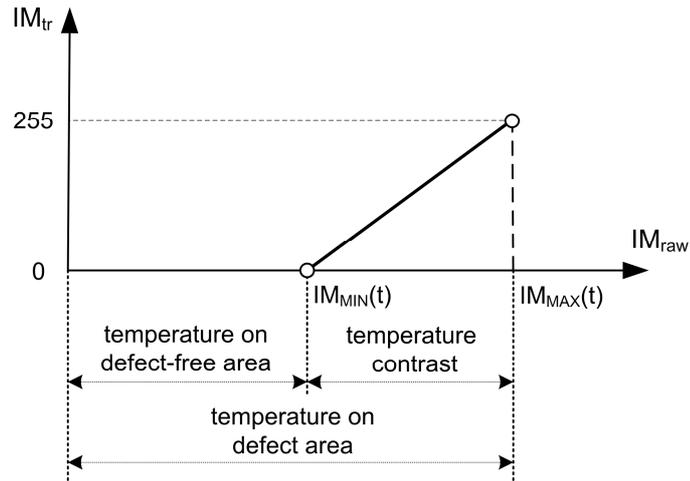
Figure 6.2: Extraction of dynamic data portion.

This transformation effectively reduces redundancy in the raw data. Strictly speaking, small temperature variations may be lost. The couple $IM_{MIN}(t)$, $IM_{MAX}(t)$ represents the entire temperature range in the image t while the computed values IM_{tr} describe the dynamic changes.

After these steps the raw data is represented by a set of 8-bit images and their corresponding maximum/minimum values (Figure 6.3). Further, we use the abbreviation $IM_{tr}(i,j,t)$ to refer to a pixel (i,j) of the image number t.
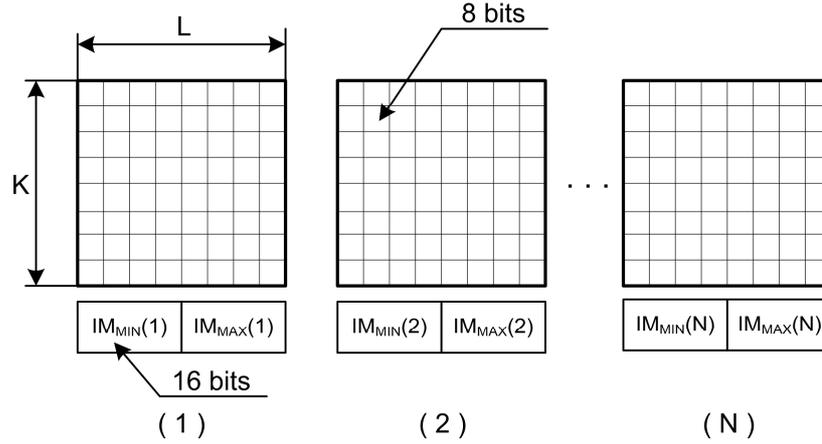
Figure 6.3: Reduced redundancy data format.

6.3.2.2 Space/time mapping (STM) method

After the redundancy reduction is performed, the method transforms a set of images as shown in Figure 6.3 into a single image to be further compressed. Taking into account that most media compressors achieve better results for smoothly changing data, we use space and time continuities to provide smoothness for any image point.

First, we consider a curve $IM_{tr}(i,j,t)$ at $1 \leq t \leq N$. It is evident that this curve is a temperature contrast, as it is computed as the difference between the lowest temperature (usually defect-free point) and the temperature at any given point (i,j). Consequently the curve has smooth behaviour which is explained by the characteristics of thermal diffusion processes.

Second, we note that each image of the input set is also relatively smooth in its space continuity, which is a consequent property of the thermal diffusion process. We now introduce a sequence SP_{tr} of $L \cdot K$ elements. The sequence SP_{tr} describes each single image as a one-dimensional array, resulting from data gathered as shown in Figure 6.4. Note also that all points in the sequence SP_{tr} are space neighbours. This fact provides the desired result – smooth changes across any space neighbours in the sequence.
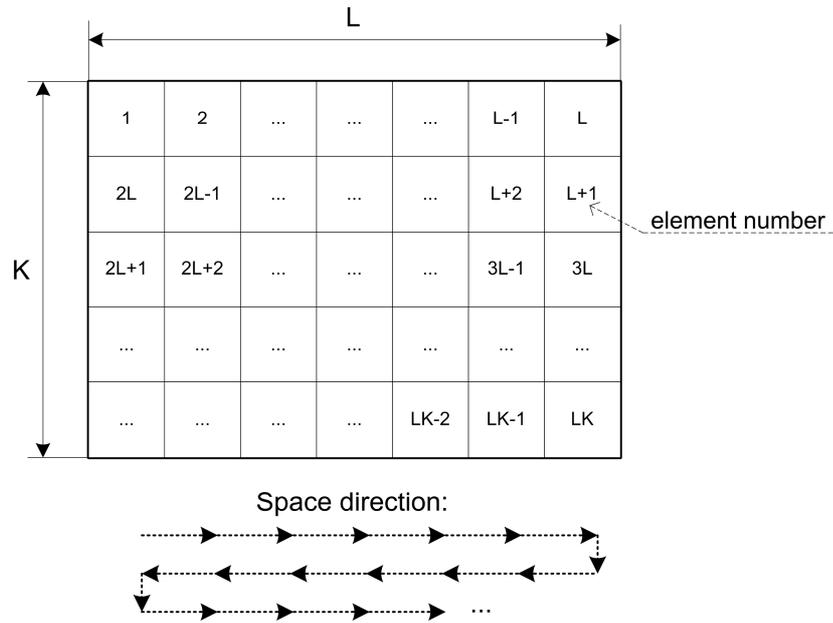
Figure 6.4: Data gathering procedure for generation of space image sequence SP_{tr}.

To further introduce time dependency, an image *STM* (space time map) with the resolution N by X axis and ($L \cdot K$) by Y axis is initialized. After that, one fills the image pixels in the following way: $pixel_{STM}(x_{pos}, y_{pos}) = IM_{tr}(i, j, x_{pos})$ where the point (i,j) is the element in the sequence SP_{tr} with the number y_{pos}. This filling process is shown schematically in Figure 6.5. To reduce abbreviations, each pixel is denoted in the form *u.t*. For example, if the pixel is marked as *u.t*, it means that the pixel equals the pixel of the image *t* with space coordinate (i,j) that corresponds to the element number *u* in the sequence SP_{tr}.
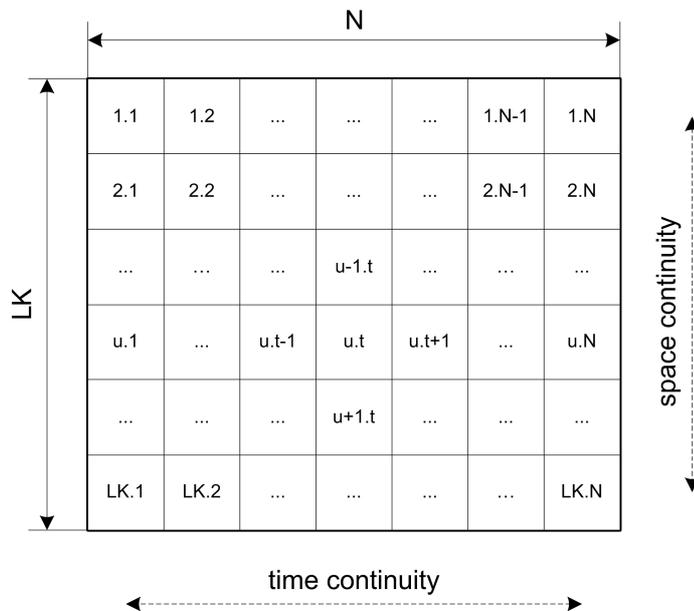
Figure 6.5: Space/time mapping.

This mapping method allows one to generate a smooth image that contains only the dynamic portion of the raw data. It can be noted that every pixel has a time neighbour in x direction and a space neighbour in y direction, and this combination provides the desired smooth space/time image. The resulting smooth image can be further compressed by any image compression algorithm.

6.3.2.3 JPEG compression

In the last step the prepared image *STM* is compressed by use of the common JPEG2000 algorithm [81], which was chosen for its high compression ratio, high reconstruction quality and high speed. The algorithm accepts the *quality/size* ratio as an input parameter for the compression procedure. The range of this parameter and its influence depends on the particular implementation of the algorithm.

In our implementation of the algorithm we used the programming language LabVIEW [82] to produce the image *STM* as a BMP file and the image processing package Corel PHOTO-PAINT (Version 12) [83] to compress it. The package provides JPEG2000 compression as a function of exporting that requires an input parameter *CMP* (compression) in the range 1-100 for varying the *quality/size* ratio. The value 1 corresponds to high quality at low compression, and the value 100 corresponds to low quality at high compression.

In Section 6.3.3 we present the results of pulsed thermography data compression for several values of *CMP*.

6.3.2.4 Data storage and expansion

The proposed algorithm stores three blocks of information: the JPEG compressed image *STM*, the sequence of the couples (maximum/minimum IR values) and the image resolution.

Once the raw data sequence has been compressed, it can be reproduced in inverse order: 1. JPEG decompression; 2. inverse transformation into reduced redundancy data format (Figure 6.3); 3. transformation into raw data format (Figure 6.1). These steps are not considered in detail as they are described above in forward order.

6.3.3 Compression results

The developed algorithm was implemented as described and applied to pulsed thermography data measured by the testing system of Fraunhofer-IZFP. In most cases the STM-JPEG algorithm compressed data tightly and provided high reproduction

quality. In the following, we present results of two IR image sequences compressed with different values of *CMP*. The quality and compressed file size are compared to those obtained by use of the TSR method. A parameter *RL* is used as a measure for reproduction loss estimation:

$$RL = \frac{1}{LK} \sum_i^K \sum_j^L RMSE_{ij} \, , \qquad (6.5)$$

where $RMSE_{ij}$ is the root mean square error computed against the actual cooling curve at the point *i,j* of the image sequence:

$$RMSE_{ij} = \sqrt{\frac{1}{N} \sum_t^N \left(IM_{raw}(i,j,t) - IM_{rep}(i,j,t) \right)^2} \, , \qquad (6.6)$$

where $IM_{rep}(i,j,t)$ is a pixel with the coordinates (*i,j*) in the image number *t* of the decompressed image sequence.

Note: In order to suppress image noise that is inevitable under practical circumstances, a 3 x 3 median filtering was applied to the measured data before storing them in raw format.

In the first example, a polyvinylchloride (PVC) plate (thickness: 5 mm) containing two grooves simulating sub-surface defects (depths: 0.7 mm and 1 mm) was tested. The sketch of the sample and its photos are given in Appendix C. The measured image sequence included 188 images with a size of 256 x 256 pixels. The data in the centre region of interest (128 x 128 pixels) were extracted and stored in raw format, which required 5.9 MB of storage space. Further the data were compressed by TSR and the STM-JPEG algorithm and their reproduction losses were estimated by Equation (6.5). Table 6.1 shown below summarizes the result of compression at different values *CMP* of the JPEG compression. The compression ratio *CR* is computed as:

$$CR = \frac{FS_{raw}}{FS_{com}} \, , \qquad (6.7)$$

where FS_{raw} is the size of the file in the raw format (uncompressed), FS_{com} is the size of the compressed file.

Table 6.1: Compression results on a PVC plate with buried grooves.

Factor	TSR method	STM-JPEG algorithm				
		CMP=1	*CMP*=20	*CMP*=40	*CMP*=60	*CMP*=80
Compression ratio (*CR*)	18.8	19.1	24.9	43.2	78.1	188
File size (FS_{com}), KB	320	314	241	139	77	32
Reproduction losses (*RL*)	5.95	2.79	3.14	3.84	4.55	5.50

Note: We also tested the codec DivX 6.2.5 [84] in the multi-pass mode for compression of the data after the redundancy reduction. The compression to the size 33 KB gave *RL* equal to 10.32 . This fact emphasizes the preference of compression by the STM-JPEG compression.

The STM-JPEG compressed file size can be one tenth of that of the TSR method, or can achieve a total compression factor of 188 at *CMP*=80. At the same *CMP*, the reproduction losses are still at a lower level than for TSR. In a trade-off with file size, *RL* can be made significantly smaller. This may be helpful, if defect reconstruction algorithms will be applied on the IR data.

In the second example, the object under test was a sample made from polyethylene with 4 circular defects of different diameters at different depths (diameter/depth: 3/1.2 mm, 5/1 mm, 3/2 mm and 5/2 mm) as depicted in Figure 2.5. The results are similar to that of the first example. Figure 6.6 shows a thermographic image of the test specimen from the cooling sequence. The entire sequence contained 98 images with a frame spacing of 0.35 s.
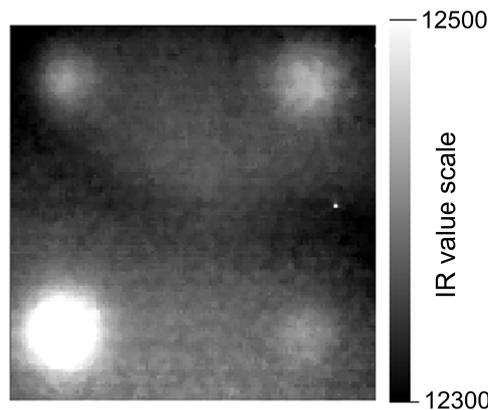
Figure 6.6: Thermographic image (frame 40) from the cooling sequence. The four sub-surface defects are visible close to the corners (image size 37 mm x 37 mm).

Again, the centre region of 128 x 128 pixels was extracted and stored in raw data format (3 MB). The compression results are shown in Table 6.2.

Table 6.2: Compression results on a polyethylene sample with flat bottom holes.

Factor	TSR method	STM-JPEG algorithm				
		$CMP=1$	$CMP=20$	$CMP=40$	$CMP=60$	$CMP=70$
Compression ratio (CR)	9.8	13.8	17.1	23.4	38.2	53.2
File size (FS_{com}), KB	320	226	183	134	82	59
Reproduction losses (RL)	5.02	2.49	2.81	3.29	4.03	4.55

The reproduction losses are shown in Figure 6.7 for the reference algorithm (TSR) and the STM-JPEG algorithm proposed here. The grey values represent the $RMSE_{ij}$ as defined in Equation (6.6). A perfect reconstruction would produce a black image. It is obvious that the proposed algorithm reduces the reproduction error significantly, in particular at the defect positions.
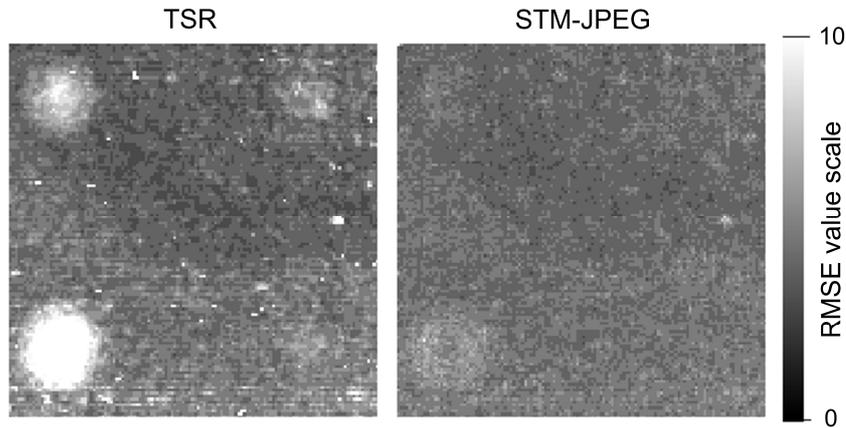
Figure 6.7: Images of the reproduction loss obtained by both algorithms (on the left - TSR method, on the right - STM-JPEG compression at $CMP=70$), the grey values represent the $RMSE_{ij}$ as defined in Equation (6.6).

Note: This case was also critically considered. The data block after the data redundancy reduction was compressed by the codec DivX 6.2.5. The data compressed to the size 59 KB gave RL equal to 5.50. The $RMSE$ images of the codec DivX and the STM-JPEG method are shown in Figure 6.8. Benefits of STM-JPEG compression are visible.
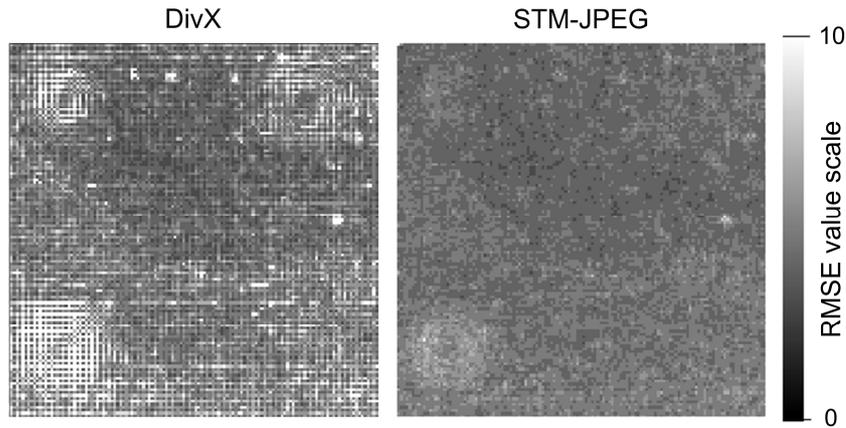
Figure 6.8: Images of the reproduction loss obtained by both algorithms (on the left – DivX comression, on the right - STM-JPEG compression at *CMP=*70), the grey values represent the $RMSE_{ij}$ as defined in Equation (6.6).

Note: After the developed method has been described, we should make some critical remarks to our own solution. The source image sequence is a three-dimensional data block. It is well known that JPEG2000 is based on the two-dimensional wavelet transformation. We apply the space/time mapping only in order to transform a 3D data block into 2D preserving local smoothness. We do this because in our tests other available video codecs (even if they are based on a certain 3D wavelet transformation according to their specification) do not give such high compression ratio at equal losses. Ideally, we need a 16-bit level codec with the 3D wavelet transformation similar to JPEG2000. Then, it will only be necessary to separate the average cooling process from the source image sequence (which is described in the following section). After that, the 3D wavelet codec should be applied to compress the obtained data.

6.4 Lossless data compression

The problem of lossless data compression has been widely discussed. The best known algorithms developed for solving this problem, and commonly used today, are Huffman coding, LZW coding and arithmetic coding [85-87]. These algorithms are based on different approaches but all exhibit a dependence of the compression ratio on the data to be compressed. A data block having a high number of repetitions (probability of a letter) can be compressed tighter than a data block having a low repetition number. In some cases the transformation of a source data block based on the information context allows the number of repetitions to be intentionally increased. This, in consequence, increases the compression ratio. Considering pulsed thermography data in the raw format one can note that there are few repetitions, so this does not allow a high compression ratio to be achieved using existing algorithms. As an approach to this problem, it is necessary to transform the data into a form suitable for compression. In

this work we propose a method that consists of a dynamically changing data transformation (DCDT) of measurement data and a compression package (ZIP) chosen as a widespread lossless compression package.

To compress pulsed thermography data, the algorithm performs two steps:

1) *Transformation of dynamically changing data (DCDT)*
   The method separates dynamical and static information, stores the data in the form suitable for compression.

2) *Lossless compression*
   The transformed data is compressed by the ZIP algorithm.

These steps are described in detail below.

6.4.1 Transformation of dynamically changing data

In this step the algorithm separates dynamic and static information contained in the data. As static information, the average cooling process is considered. All image IR values $IM_{raw}(i,j,t)$ at $1 \le t \le N$ decrease with more or less similar speed that is explained by a transient cooling process after thermal excitation [55]. To separate the cooling process and dynamic changes (dc), the algorithm computes average image temperatures $AV(t)$:

$$AV(t) = \left[\frac{\sum_i \sum_j IM_{raw}(i,j,t)}{LK} \right],\tag{6.8}$$

and subtracts the computed temperatures from source images:

$$IM_{dc}(i,j,t) = IM_{raw}(i,j,t) - AV(t).\tag{6.9}$$

The row $AV(t)$ represents the average temperature in each image while the values $IM_{dc}(i,j,t)$ describe the deviations from it. Further, the algorithm extracts dynamic changes of single image pixels (sip) computing the difference of pixel values between adjacent images:

$$IM_{dc-sip}(i,j,t) = IM_{dc}(i,j,t) - IM_{dc}(i,j,t+1).\tag{6.10}$$

Note that the difference $IM_{dc-sip}(i,j,t)$ is computed for all pixel values except the last image N. The performed computations significantly increase the number of repetitions

in the data $IM_{dc\text{-}sip}(i,j,t)$. If the probability histogram of $IM_{dc\text{-}sip}(i,j,t)$ values is considered, the maximal probability will be close to the pixel value 0 and rapidly decrease from 0 to $+\infty$ and from 0 to $-\infty$. Figure 6.9 shows the probability histogram of $IM_{raw}(i,j,t)$ values (raw data format) for the sample with four flat bottom holes. Figure 6.10 depicts the probability histogram of $IM_{dc\text{-}sip}(i,j,t)$ values (data after processing by the equations (6.8-6.10)). It is clearly seen that the histogram has been changed to the desired form.
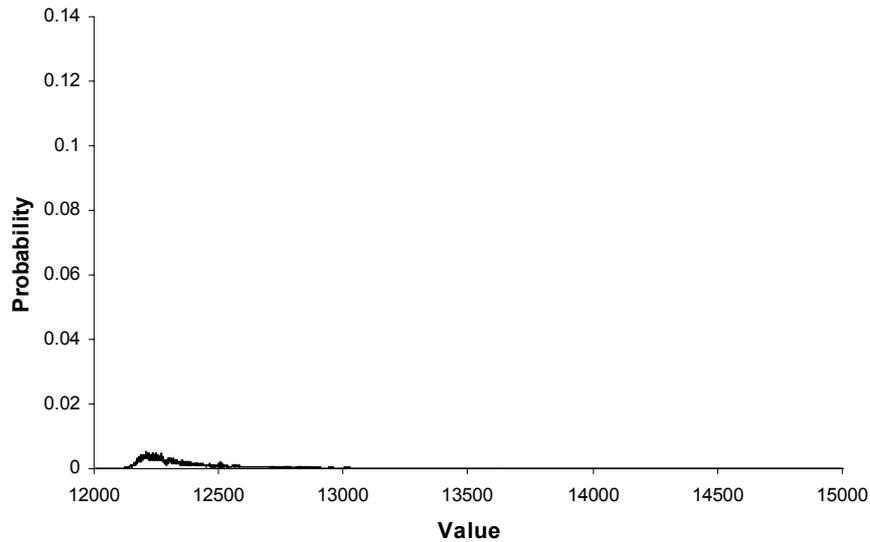
Figure 6.9: Probability histogram of the measurement data
(sample with four flat bottom holes which is schematically shown in Figure 2.5).
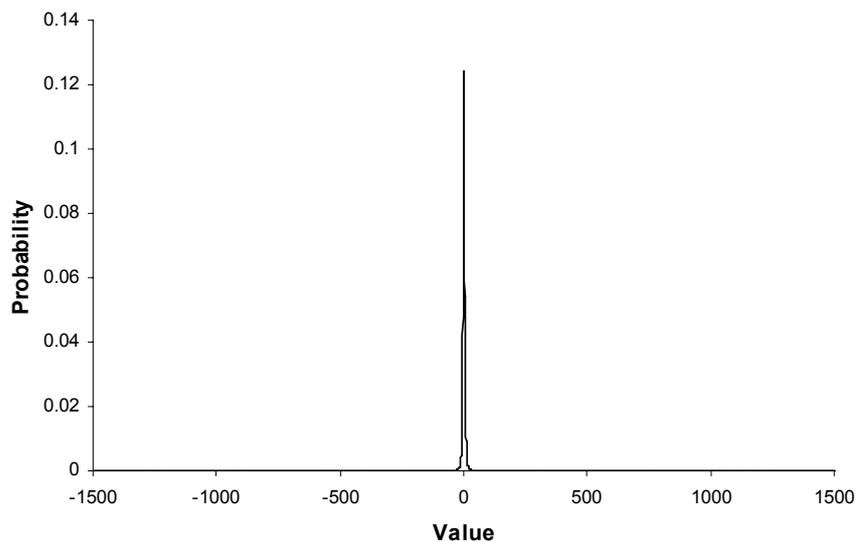
Figure 6.10: The probability histogram of the measurement data
(sample with four flat bottom holes) after processing using equations (6.8)-(6.10).

In binary form it has the feature that bits of low order contain most of the changes while bits of high order are almost always equal to zero. In order to effectively use this feature, the algorithm carries out a bit separation by bit order. Note, that we choose the 16-bit integer form to store values $IM_{dc\text{-}sip}(i,j,t)$ where the highest bit is used for a sign and 15 bits are used for the number coding. The algorithm forms 16 single data chains by the following equation:

$$DC(n) = \perp_t \perp_i \perp_j \left(IM_{dc-sip}(i,j,t)_{[n]} \right) \qquad for\ n=0{:}15 \qquad (6.11)$$

where the abbreviation $IM_{dc\text{-}sip}(i,j,t)_{[n]}$ denotes an extraction of the n-th bit from the value $IM_{dc\text{-}sip}(i,j,t)$ and the abbreviation $\perp_k a(k)$ denotes a bit-concatenation of elements a in forward order: $a(1),a(2),a(3)...$. This transformation is schematically shown in Figure 6.11. To store data chains, they are converted into the byte form.
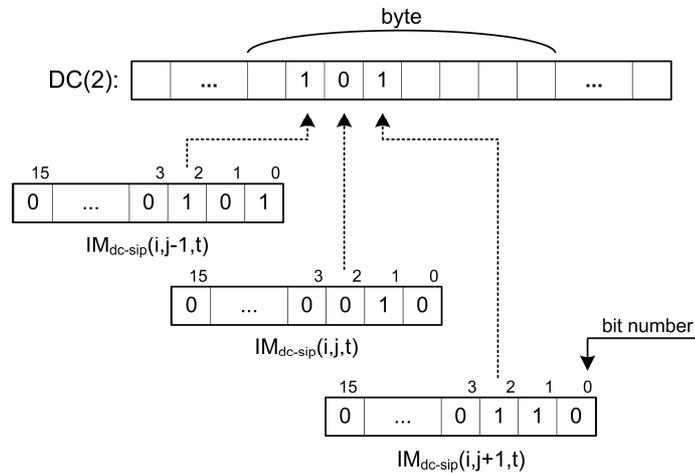
Figure 6.11: Example of the formation of the data chain DC(2).

After these steps have been completed, the algorithm stores a data structure that includes the raw $AV(t)$, the last image $IM_{dc}(i,j,N)$, and 16 data chains $DC(n)$. For simplicity of description we will assume that they are stored as single files to be compressed: a file *av-t.raw* for raw $AV(t)$, a file *im-dc-n.img* for the last image $IM_{dc}(i,j,N)$, files *dc-0.dat*, *dc-2.dat … dc-15.dat* for data chains $DC(n)$, a file *descr.txt* that contains supplemental information – the number of images, image resolution, etc.

6.4.2 Lossless compression

There are a lot of software packages we can use for file compression. ZIP, TAR, RAR, UHA are the best known. They differ from each other in the internal compression algorithms and their implementations. To compress data obtained in the previous step of our algorithm, we chose to apply the package ZIP (WinZip, Version 9 [88]) due to its

popularity, availability and high speed. Note that any lossless compression package can be used instead of ZIP. The results of data compression are presented in Section 6.4.4.

6.4.3 Data storage and expansion

All obtained files *av-t.raw*, *im-dc-n.img*, *descr.txt*, *dc-0.dat … dc-15.dat* are compressed by the package ZIP to a single file.

The decompression procedure is carried out in inverse order: First, ZIP decompression, then inverse DCDT transformation. We will not consider them again as they were presented above in forward order.

6.4.4 Compression results

The developed method was also applied to pulsed thermography data measured by the testing system of Fraunhofer-IZFP. The algorithm shows better compression ratio than pure ZIP compression of the data in raw format. Table 6.3 summarizes the result of compression of the two image sequences described in Section 6.3.3 (PVC plate with buried grooves, polyethylene sample with flat bottom holes). As seen, the algorithm, namely the DCDT transformation, allows the compression ratio to be increased significantly.

Table 6.3: Compression results on PVC and polyethylene sample.

Sample and Factor		data in raw format (uncompressed)	ZIP compression	DCDT-ZIP compression
PVC plate with buried grooves	Compression ratio (*CR*)	1	1.86	3.79
	File size, MB	5.88	3.15	1.55
polyethylene sample with flat bottom holes	Compression ratio (*CR*)	1	2.23	3.64
	File size, MB	3.06	1.37	0.84

To complete the method description, we note that the transformation DCDT should be adjusted to the compression package we apply in the last step (Equation (6.11)) when the data chains $DC(n)$ are formed from $IM_{dc\text{-}sip}(i,j,t)$. Our tests have shown that, if ZIP is used, the transformation (Equation (6.11)) is useful, as it increases the compression ratio. But some packages (e. g. RAR in maximal compression mode (WinRAR, Version 3 [89])) compress the data $IM_{dc\text{-}sip}(i,j,t)$ and $DC(n)$ with almost the

same ratios. So, the transformation (Equation (6.11)) can be skipped. Nevertheless, we emphasize that the DCDT transformation in the form we described is the most suitable and universal for any data or text compressor.

6.5 Conclusion

In this chapter, new lossy and lossless compression methods for pulsed thermography data were proposed and tested using experimental data. The STM-JPEG method combines the specific space/time representation of dynamically changing data and a well established static image compression algorithm. This combination achieves a high compression ratio while preserving high reconstruction quality. The DCDT-ZIP algorithm involves the specific transformation of dynamically changing data and a well established lossless data compression algorithm. The developed algorithms have demonstrated good results when applied to various experimental data sets measured by pulsed thermography.

Chapter 7

7.1 Summary

In this work a new defect shape reconstruction algorithm for pulsed thermography (PT) was developed. The reconstruction principle used in the algorithm is based on a one-dimensional defect depth retrieval technique combined with the numerical simulation of the PT experiment. This combination significantly extends capabilities of PT as a quantitative characterization tool. Contrary to the recently proposed reconstruction algorithm [10], the algorithm presented here can be applied for wide classes of defects. There is no restriction on thermal properties of the sample and defect media, nor on the geometrical sample shape. It is worth noting that the developed algorithm reconstructs the defect shape faster (by up to 10 times) than the recently proposed solution.

The reconstruction is carried out by extracting an echo defect shape from the measurement of the inspected sample. The echo defect shape is a thermal defect response evaluated by the one-dimensional defect depth retrieval technique in early time range. The echo defect shape contains unique accumulated information of backward and lateral thermal pulse reflections caused by the actual defect shape in the inspected sample. The developed algorithm uses a simulated model of the inspected sample (thermal properties of the sample and defect media and the sample geometrical sizes are assumed to be known). The algorithm takes the echo defect shape of the measurement as the initial defect shape in the sample model. Simulating the PT experiment iteratively the algorithm sequentially corrects the defect shape in the sample model. The corrections are computed converging the echo defect shapes of the measurement and the model simulation. The reconstruction principle implies that if the echo defect shapes from the measurement and the simulation are equal, then all internal backward and lateral reflections are also equal and, consequently, the inspected sample and the model have identical defect shapes. Many tests demonstrate that the algorithm reconstructs the defect shape with satisfactory precision in two/three iterations if the defect shape satisfies the resolution criteria in PT.

The developed algorithm consists of a defect shape correction unit and a simulation unit. The defect shape correction unit is designed to extract the echo defect shape and correct the reconstructed defect shape while the simulation unit simulates the heat conduction process in the inspected sample model.

The algorithm was tested under experimental conditions. It is proposed for experimental application that a reference (defect-free) sample is measured in addition. It allows the uneven heating effects to be suppressed. An experimental reconstruction of an artificial corrosion profile in a steel sample was presented.

The most time consuming part of the reconstruction algorithm is the simulation of the pulsed thermography experiment. For industrial applications this part of the algorithm can be accelerated by parallelizing the computations (for example, in computer clusters) [90,91] and optimizing the experiment model (space and time mesh).

In this work the problem of data compression in PT was also considered. Lossy and lossless methods for measurement compression were proposed. For the lossy approach the cooling process was separated in the source image sequence and a wavelet-based data compression was applied. Particularly, in this work the method was implemented using a special combination with an image compression algorithm (JPEG2000) that was chosen for its high compression ratio. This combination provides better quality in data decompression in comparison to the latest developed video codec (DivX 6.2.5) at the equal compression ratio. For the lossless approach we propose to extract dynamic changes of the source image sequence and compress them by using existing algorithms (particularly, in this work the algorithm (ZIP) was applied). The extraction of dynamic changes is performed in two steps: first, the average cooling process is separated and, second, dynamic changes between adjacent images are computed. Such pre-processing modifies the probability histogram of the source data that, as a result, increases the compression ratio for any lossless compressor applied afterwards. The achieved compression ratios for both methods are higher than that provided by existing compression algorithms on raw measurement data.

As an example of a quantitative and efficient PT Experiment the test sample with IZFP-logo is again presented showing also the depth information for the different letters.
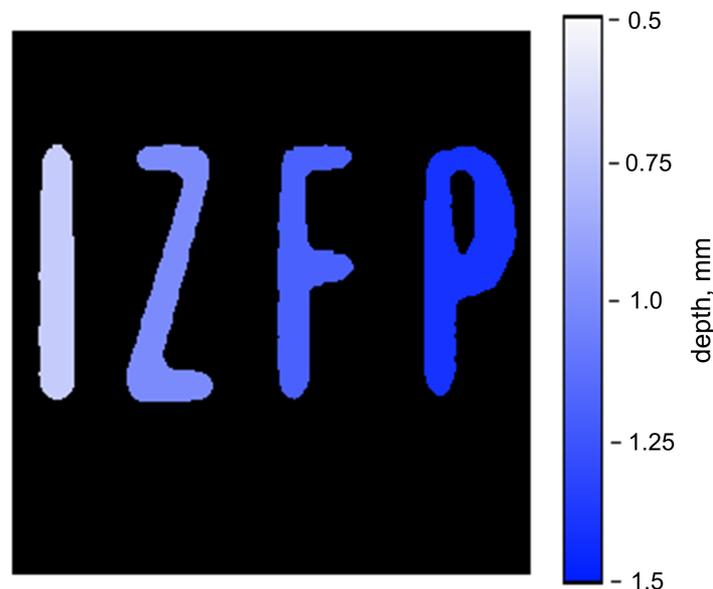
Figure 7.1: Quantitative representation of the depth information of the test sample with IZFP-logo.

7.2 Future work

The defect shape reconstruction algorithm developed in this work operates under the assumption that thermal properties of the defective medium are known. We suppose that the algorithm can be extended and adopted to cases where the defect thermal properties are unknown. Here we point out that the new algorithm will additionally analyze and change the defect thermal properties affecting the reflection coefficient K_{ref} between the sample and defect medium. The time range in which the data are analyzed should be extended approximately up to the instant when the temperature contrast for the deepest defect point reaches a maximum value. This is schematically shown in Figure 7.2. The extension is necessary as the temperature contrast curve (the amplitude and time evolution) contains information about the reflection coefficient.
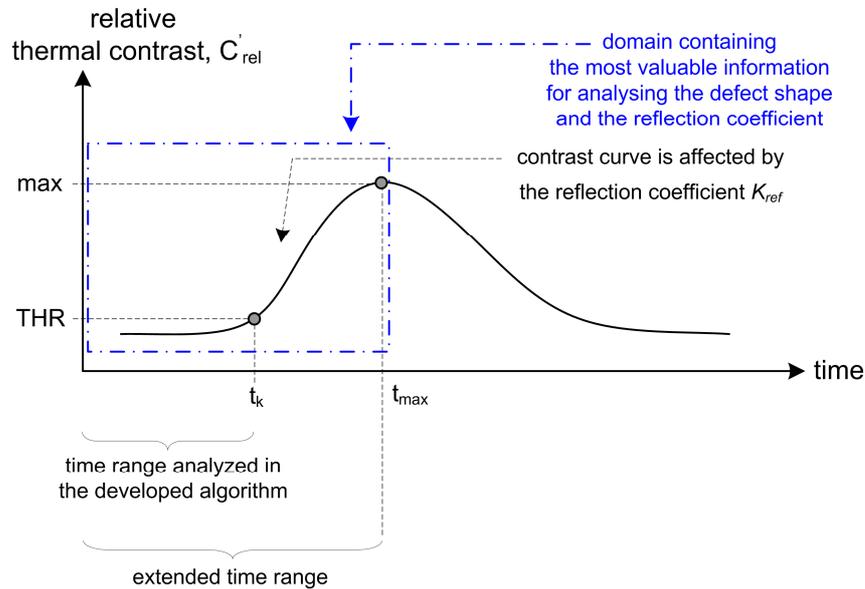
Figure 7.2: Analysis of the temperature contrast.

The easiest solution is to reconstruct the sample with unknown defect properties using a set of the predefined reflection coefficients K_{ref}, for example, 0.1, 0.2 … 0.8, 0.9, 1. Then one can find a sample model which produces the closest relative thermal contrasts C'_{rel} everywhere on the sample surface with respect to the analyzed sample. But this is a very time consuming solution. We expect that after detailed investigation of the problem an intelligent solution can be found.

For data compression the lossy method can be improved. One can suggest the implementation of a 16-bit 3D wavelet codec and apply it after the average cooling process will be separated from the source data. It will allow the initial camera sensitivity to be preserved (avoiding 256-level discretization) and an increase in the compression ratio.

Appendix A

List of Most Important Symbols

Symbol	Units	Description
T	K	temperature
t	s	time
ρ	kg/m^3	density
λ	W/(mK)	thermal conductivity
c	J/(kgK)	thermal heat capacity
α	m^2/s	thermal diffusivity
e	Ws$^{1/2}$/(Km^2)	thermal effusivity
Q	J/m^2	input (or absorbed) energy density
$f^q_{front(a)}$	W/m^2	approximated heat flux density on the front sample side
t_{ex}	s	excitation time (heat pulse duration)
K_{ref}		reflection coefficient
K_{trans}		transmission coefficient
th	m	thickness
IM	K	measured (recorded) image sequence
d	m	defect depth
T_s	K	temperature on the point to be analysed
$T_{in\text{-}th}$	K	temperature of the defect-free sample with infinite thickness
T_{incr}	K	temperature increase due to pulse reflection
t_k	s	time at which the temperature increase is analysed
$T_{rel\text{-}incr}$	K	relative temperature increase at t_k
$T_{defect\text{-}free}$	K	temperature on the defect-free area
C'_{rel}		relative thermal contrast
$T_{ref.s}$	K	temperature of the reference (defect-free) sample
THR		threshold value used for computation of the echo defect shape from the relative thermal contrast
TD		thermal distribution ($TD=M$ denotes the measurement M, $TD=S$ denotes the simulation S)

List of Most Important Symbols (Continued)

Symbol	Units	Description
$EDS(x,TD)$	m	echo defect shape in the point x extracted from the thermal distribution TD
$DS(x,S(i))$	m	defect shape in the point x used in the simulation $S(i)$
$DS_{defect}(x,M)$	m	actual defect depth in the point x in the measurement M
$DS_{l.flow}(x,TD)$	m	reduced defect depth value in the point x due to the lateral thermal flow ($TD=M$ denotes the measurement M, $TD=S$ denotes the simulation S)
IM_{raw}		recorded image sequence in raw data format
L,K	pixels	image resolution in raw data format
IM_{tr}		image sequence transformed into reduced redundancy data format
$IM_{MIN}(t)$		minimum IR value in image t
$IM_{MAX}(t)$		maximum IR value in image t
SP_{tr}		sequence which describes the image as a one-dimensional array
RL		reproduction loss estimate
$RMSE$		root mean square error
IM_{rep}		decompressed image sequence
CR		compression ratio
FS_{raw}	KB	size of file in raw format
FS_{com}	KB	size of compressed file
$AV(t)$		average temperature of image t
IM_{dc}		dynamic changes of temperature with respect to the average image temperature $AV(t)$
$IM_{dc\text{-}sip}$		dynamic changes of single image pixels between adjacent images IM_{dc}
$DC(0\ldots15)$		data chains containing bits of equal order

Appendix B

Abbreviations

NDT	Non-destructive Testing
PT	Pulsed Thermography
SH	Step Heating Thermography
LT	Lock-in Thermography
VT	Vibrothermography
IR	Infrared
FWHM	Full-Width At Half Maximum
TSR	Time Signal Reconstruction
TNDT	Thermal Non-destructive Testing
PC	Personal Computer
NETD	Noise Equivalent Temperature Difference
PDE	Partial Differential Equation
FDM	Finite Difference Method
FEM	Finite Element Method
BEM	Boundary Element Method
EDS	Echo Defect Shape
JPEG	Joint Photographic Experts Group
MPEG	Moving Picture Experts Group
STM	Space/Time Mapping
PVC	Polyvinylchloride
DCDT	Dynamically Changing Data Transformation

Appendix C

Sample "IZFP"

The sketch of the sample with buried grooves in form of letters is illustrated in Figure 3.10. The sample is made of polyvinylchloride (PVC). The sample photographs are shown in Figure C.1 (front side view) and Figure C.2 (back side view).

Figure C.1: PVC sample with buried grooves (front side view).
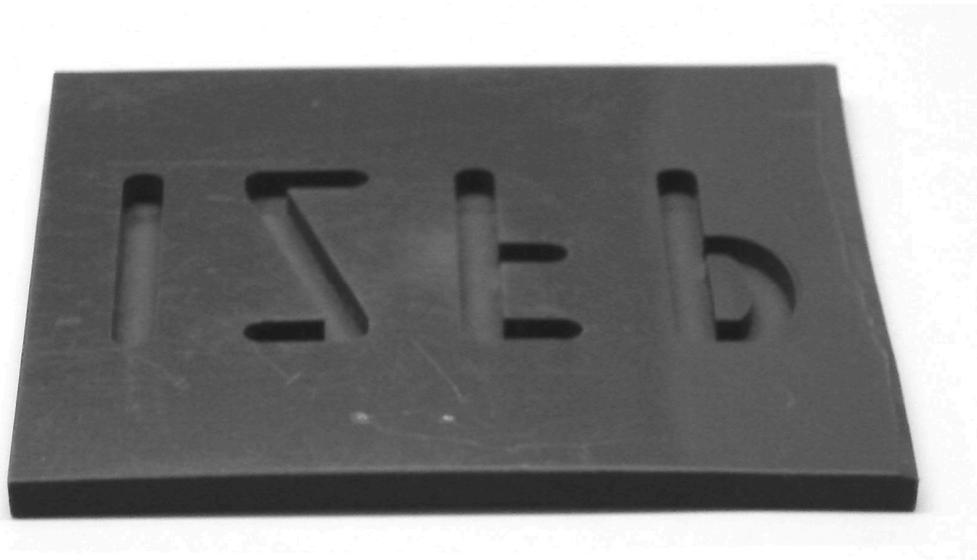
Figure C.2: PVC sample with buried groove (back side view).

Appendix D

Measurement Setup

The measurement setup with arrangement for experimental defect shape reconstruction is shown in Figure D.1.
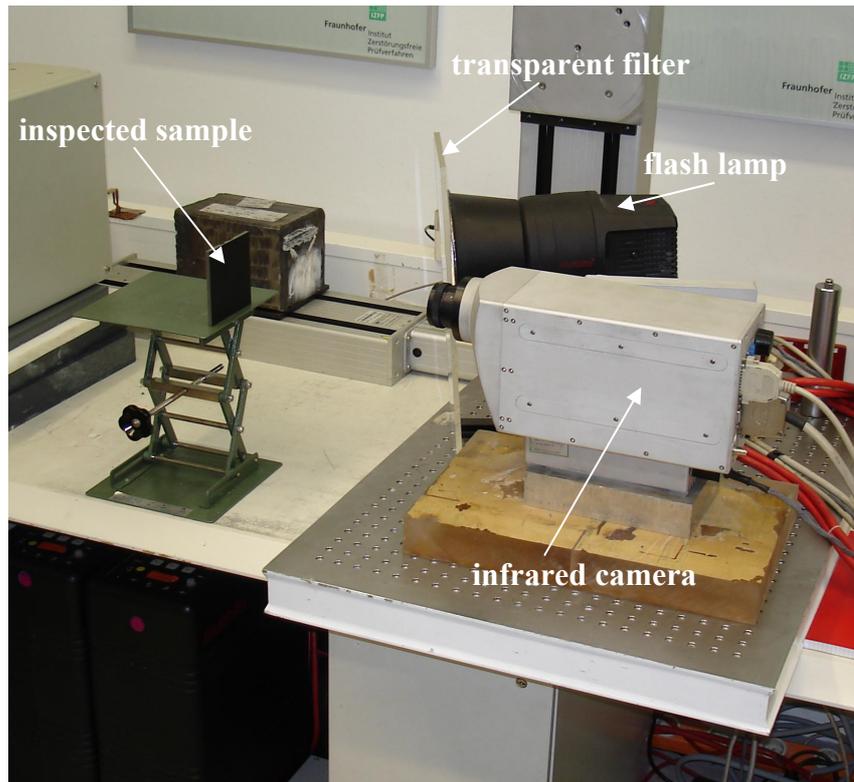
Figure D.1: Measurement setup.

The setup includes a single flash lamp located on the left side with respect to the sample. The surface of the inspected sample is oriented perpendicular to the camera observation angle.

The infrared camera is shown in Figure D.2.
The technical parameters are given in Table D.1

Table D.1: Technical parameters of the infrared camera.

Model:	Infrared CCD Camera
Resolution:	256^2
IR wavelength range:	3-5 μm
Digitalization:	14 bit
Sensitivity (NETD):	< 0.05 °C
Full-size frame rate:	200 frames/s

Figure D.2: Infrared camera.

The flash lamp is shown in Figure D.3. The lamp excitation energy is 4000 Ws.
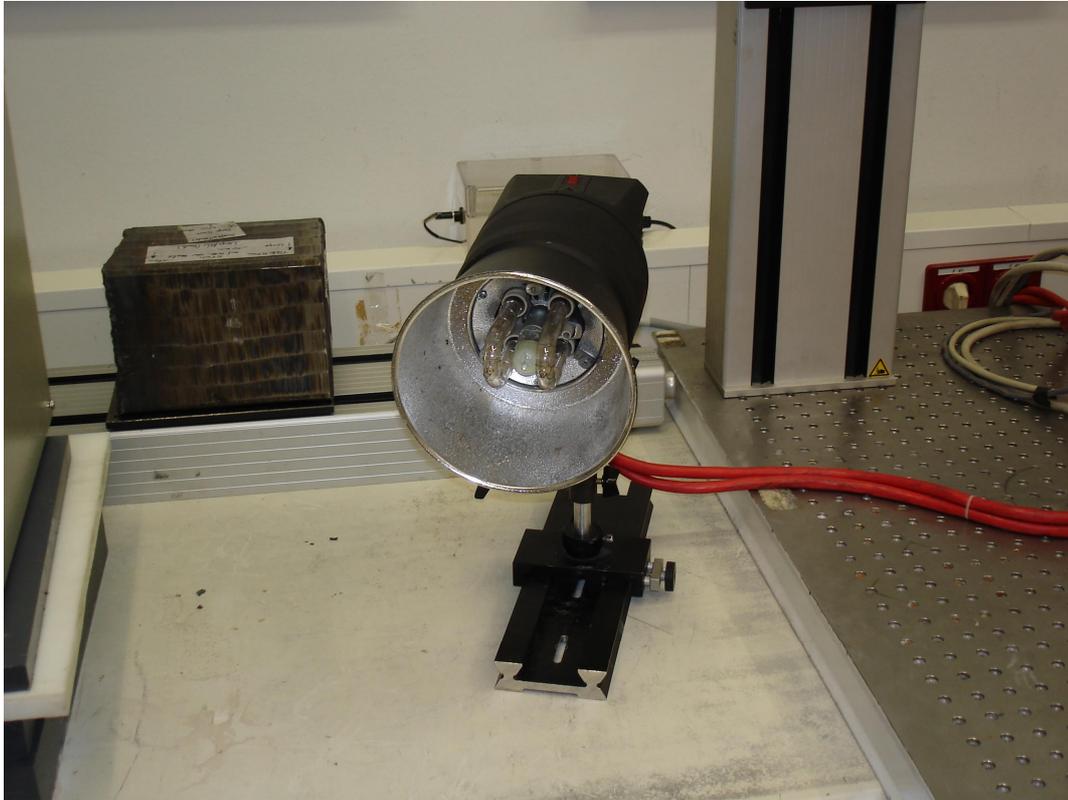
Figure D.3: Flash lamp.

Appendix E

Samples used for experimental defect shape reconstruction

The sketch of the sample used for experimental reconstruction of the defect shape is illustrated in Figure E.1. The photographs of the original and reference samples are shown in Figure E.2 (front side view) and in Figure E.3 (back side view). The samples are made of stainless steel (V2A). The thermal properties of steel are $\lambda=15$ W/mK, $\rho=8000$ kg/m^3, $c=477$ J/kgK.
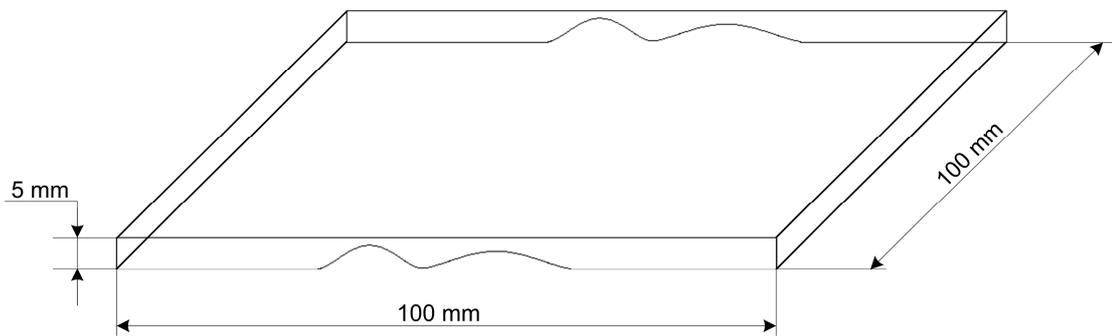
Figure E.1: Sketch of the steel sample with artificial corrosion profile.
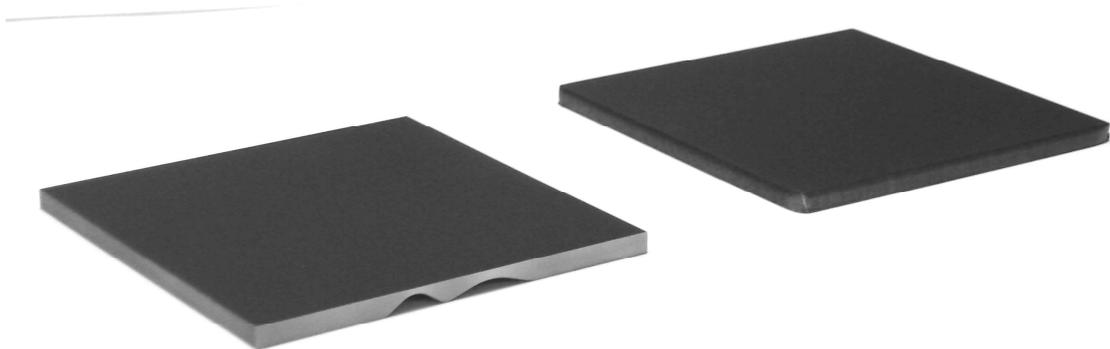
Figure E.2: Corroded and reference sample (front side view).
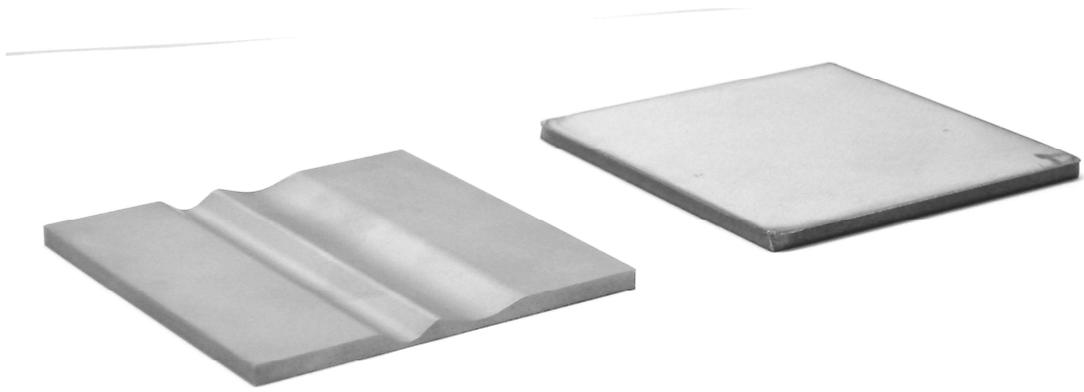
Figure E.3: Corroded and reference sample (back side view).

References

[1] C. Hellier. Handbook of Nondestructive Evaluation. McGraw-Hill, 2001.

[2] P.E. Mix. Introduction to Nondestructive Testing, A Training Guide. John Wiley & Sons, 2005.

[3] D.E. Bray and D. McBride. Nondestructive Testing Techniques. John Wiley & Sons, 1992.

[4] X. Maldague. Theory and Practice of Infrared Technology for Non-Destructive Testing. John Wiley & Sons, 2001.

[5] G. Gaussorgues. Infrared Thermography. Chapman & Hall, London, 1994.

[6] X. Maldague. NDT by Infrared Thermography: Principles with Applications. Topics on NDE, **1**:385-398, 1998.

[7] X. Maldague. Applications of Infrared Thermography in Nondestructive Evaluation. Proceedings of the International Conference on Trends in Optical Nondestructive Testing, 2000.

[8] X. Maldague, F. Galmiche and A. Ziadi. Advances in Pulsed Phase Thermography. Infrared Physics & Technology, **43**:175-181, 2002.

[9] X. Maldague. Introduction to NDT by Active Infrared Thermography. Materials Evaluation, **6**(9):1060-1073, 2002.

[10] K. Bryan and L. Caudill. Reconstruction of an Unknown Boundary Portion from Cauchy Data in N-Dimension. Inverse Problems, **21**(1):239-255, 2005.

[11] X. Han, L.D. Favro and R.L. Thomas. Thermal Wave NDI of Disbonds and Corrosion in Aircraft. Proceedings of the Second Joint NASA/FAA/DOD Conference on Aging Aircraft , Willamsburg , Virginia, 1998.

[12] V. Carl, E. Becker and A. Sperling. Quantitative Wallthickness Measurement with Impuls-Video-Thermography. Proceedings of 7-th European Conference on Non-Destructive Testing, Copenhagen, 1998.

[13] A.R. Hamzah, P. Delpech, M.B. Saintey and D.P. Almond. An Experimental Investigation of Defect Sizing by Transient Thermography. Insight, **38**(3):167-171, 1996.

[14] D.L. Balageas, J.C. Krapez and P. Cielo. Pulsed Photothermal Modeling of Layered Materials. Applied Physics, **59**(2):348-357, 1986.

[15] D.P. Almond and S.K. Lau. Edge Effects and a Method of Defect Sizing by Transient Thermography. Applied Physics, **62**(25):3369-3371, 1993.

[16] R.L. Thomas, L.D. Favro, D.J. Crowther, P.K. Kuo. Inversion of Thermal Wave Infrared Images. Proceedings of Conference "Quantitative Infrared Thermography QIRT 92", France, Paris, 1992.

[17] W. Karpen, M. Jöchen and U. Netzelmann. Numerical Filters as a Tool for Defect Characterization in Pulsed Thermography. Journal de Physique IV, **125**:531-533, 2005.

[18] S.M. Shepard, T. Ahmed, B.A. Rubadeux, D. Wang and J.R. Lhota. Synthetic Processing of Pulsed Thermographic Data for Inspection of Turbine Components. Insight, **43**(9): 587-589, 2001.

[19] S.M. Shepard. Temporal Noise Reduction, Compression and Analysis of Thermographic Image Data Sequences. US Patent (6,516,084), 2003.

[20] H.R. Ringermacher and D.R. Howard. Synthetic Reference Thermal Imaging Method. US Patent (6,367,969), 2002.

[21] B.B. Chaudhry, H. Holmes, S.M. Shepard and T. Ahmed. Thermographic Quality Assurance of Turbine Engine Components. Proceedings of International Joint Power Generation Conference, 2002.

[22] V. Carl, E. Becker and A. Sperling. Thermography Inspection System for Gas Turbine Blades. Proceedings of 7-th European Conference on Non-Destructive Testing, Copenhagen, 1998.

[23] S.M. Shepard, D. Wang, J.R. Lhota, T. Ahmed and B.A. Rubadeux. Parallel Processing and Analysis of Thermographic Data. Review of Progress in Quantitative Non-Destructive Evaluation, **21**:558-563, 2002.

[24] X. Hah, T. Ahmed and L. Wang. Thermal Wave Imaging of Disbonding and Corrosion on Aircraft. Review of Progress in Quantitative Non-Destructive Evaluation, **15**:1747-1753, 1996.

[25] V. Vavilov, E. Grinzato, P. G. Bison and S. Marinetti. Surface Transient Temperature Inversion for Hidden Corrosion Characterisation: Theory and Applications. International Journal of Heat and Mass Transfer, **39**:355-371, 1996.

[26] N. Rajic. Quantitative Examination of Corrosion Damage by Means of Thermal Response Measurements. Report (NASA/TP-1998-208429), 1998.

[27] J. Prati. Detecting Hidden Exfoliation Corrosion in Aircraft Wing Skins Using Thermography. Proceedings of SPIE, **4020**:200-209, 2000.

[28] X. Han, L.D. Favro, T. Ahmed, Z. Ouyang, L. Wang, X. Wang, F. Zhang, P.K. Kuo and R. L. Thomas. Quantitative Thermal Wave Imaging of Corrosion on Aircraft. Review of Progress in Quantitative Non-Destructive Evaluation, **16**:353-356, 1997.

[29] S. Vallerand and X. Maldague. Defect Characterization in Pulsed Thermography: a Statistical Method Compared with Kohonen and Perceptron Neural Networks. NDT&E International, **33**:307-315, 2000.

[30] S.M. Shepard, B.A. Rubadeaux and J.R. Lhota. Method and System for Reference-Free Thermographic Detection of Subsurface Defects Using Compressed Image Data. Patent (WO 01/41421 A2), 2000.

[31] S.M. Shepard, T. Ahmed and B.C. Chaudhry. Resolution Criteria for Subsurface Features in Active Thermography. Review of Progress in Quantitative Non-Destructive Evaluation, **18**:605-610, 1999.

[32] V. Vavilov, X. Maldague, B. Dufort, F. Robitaille and J. Picard .Thermal Non-Destructive Testing of Carbon Epoxy Composites: Detailed Analysis and Data Processing. NDT&E International, **26**(2):85-95, 1993.

[33] D.J. Roth, J.R. Bodis and C. Bishop. Capability of Single-Sided Transient Thermographic Imaging Method for Detection of Flat Bottom Hole Defects in High-Temperature Composite Materials. Review of Progress in Quantitative Non-Destructive Evaluation, **16**:1127-1134, 1997.

[34] S. Quek and D.P. Almond. Defect Detection Capability of Pulsed Transient Thermography. Insight, **47**(4):212-215, 2005.

[35] G. Morel, A. Wyckhuse and X. Maldague. Active Pulsed Infrared Thermography for Concrete Bridge Deck Inspection. Journal of Canadian Institute of Non-Destructive Evaluation, **22**(4):6-12, 2001.

[36] J.M. Milne and W.N. Reynolds. Application of Thermal Pulses and Infrared Thermal Imagers for Observing Subsurface Structures in Metals and Composites. Proceedings of SPIE, **590**:293-302, 1985.

[37] N. Rajic. A Quantitative Approach to Active Thermographic Inspection for Material Loss Evaluation in Metallic Structures. Research in Non-Destructive Evaluation, **12**:119-131, 2000.

[38] C.P. Hobbs and A. Temple. The Inspection of Aerospace Structures Using Transient Thermography. British Journal of Non-Destructive Testing, **35**(4):183-189, 1993.

[39] R.J. Ducar. Pulsed Thermographic Inspection and Application in Commercial Aircraft Repair. Proceedings of SPIE, **3700**:77-83, 1999.

[40] S.K. Lau, D.P. Almond and J.M. Milne. A Quantitative Analysis of Pulsed Video Thermography. NDT&E International, **24**(4):195-202, 1991.

[41] D.P. Almond and W. Peng. Thermal Imaging of Composites. Journal of Microscopy, **20**:163-170, 2001.

[42] S. Marinetti, P.G. Bison, E. Grinzato and G. Manduchi. Automatic Procedure for Thermal NDE of Delaminations in CFRP by Using Neural Networks. Review of Progress in Quantitative Non-Destructive Evaluation, **16**:773-780, 1997.

[43] R.E. Martin, A.L. Gyekenyesi and S.M. Shepard. Interpreting the Results of Pulsed Thermography Data. Materials Evaluation, **61**(5):611-616, 2003.

[44] D.L. Balageas, A.A. Deom and D.M. Boscher. Characterization and Non-Destructive Testing of Carbon-Epoxy Composites by a Pulsed Photothermal Method. Materials Evaluation, **45**(4):466-465, 1987.

[45] R.E. Martin and A.L. Gyekenyesi. Pulsed Thermography of Ceramic Matrix Composites. Proceedings of SPIE, **4704**:82-92, 2003.

[46] U. Netzelmann, G. Walle and H. Zhang. Characterisation of Plasma-Sprayed Coatings Using NDE Techniques. Insight, **39**:887-894, 1997.

[47] U. Netzelmann and G. Walle. High-Speed Thermography of Thin Metallic Coatings. Proceedings of International Conference on Photoacoustic and Photothermal Phenomena, Italy, Rom, 1998.

[48] G. Walle and U. Netzelmann. Application of Pulsed Video Thermography for Materials Characterization. Progress in Natural Science, **6**:83-86, 1996.

[49] S. Shepard, Y. Hou and J. Lhota. Quantitative Characterization of Thermographic Sequence Data. Proceedings of 16-th World Conference on Non-Destructive Testing, Canada, Montreal, 2004.

[50] M.B. Saintey and D.P. Almond. An Artificial Neural Network Interpreter for Transient Thermography Image Data. NDT&E International, **30**(5):291-295, 1997.

[51] S.M. Shepard. Advances in Thermographic NDT. Proceedings of SPIE, **5074**:882-887, 2003.

[52] S.M. Shepard and J.R. Lhota. Spatial-Temporal Signal Processing for Subsurface Thermographic Imaging. Proceedings of SPIE, **5073**:401-405, 2003.

[53] M.B. Saintey and D.P. Almond. Defect Sizing by Transient Thermography II: a Numerical Treatment. Journal of Physics D: Applied Physics, **28**:2539-2546, 1995.

[54] P. Cielo. Pulsed Photothermal Evaluation of Layered Materials. Journal of Applied Physics, **56**(1):230-234, 1984.

[55] D.P. Almond and P.M. Patel. Photothermal Science and Techniques. Chapman & Hall, 1996.

[56] H.I. Ringermacher, D.J. Mayton, D.R. Howard and B.N. Cassenti. Towards a Flat-Bottom Hole Standard for Thermal Imaging. Review of Progress in Quantitative Non-Destructive Evaluation, **17**:425-429, 1998.

[57] V.P. Vavilov and R. Taylor. Theoretical and Practical Aspects of the Thermal Non-Destructive Testing of Bonded Structures. Research Techniques in Non-Destructive Testing, **5**:238-279, 1982.

[58] H.J. Vidberg, J. Jaarinen and D.O. Riska. Inverse Determination of the Thermal Conductivity Profile in Steel from the Thermal Wave Surface Data. Preprint Series in Theoretical Physics, 1985.

[59] J.F. Power. A Survey of Current Issues in Inverse Problem Theory as Applied to Thermal Wave Imaging. AIP (American Institute of Physics) Conference Proceedings, **463**:3-7, 1999.

[60] T.N. Lan, U. Seidel and H.G. Walther. Theory of Microstructural Depth Profiling by Photothermal Measurements. Journal of Applied Physics, **77**:4739-4745, 1995.

[61] EC Project HARDPHOTOTEC (Institute for Advanced Materials, Ispra): "Development of a Photothermal Measuring Technique for the Determination of Hardness Profiles in Steel", Brite-Euram report nr. CT97-5032, 2001.

[62] L.M. Jiji. Heat Transfer Essentials. Begell House, 2002.

[63] G.F. Hewitt, G.L. Shires and T.R. Bott. Process Heat Transfer. CRC Press, 1994.

[64] K. Kurpisz and A.J. Nowak. Inverse Thermal Problems. Computational Mechanics Publications, 1995.

[65] M.N. Ozisik. Finite Difference Methods in Heat Transfer. CRC Press, 1994.

[66]   G.D. Smith. Numerical Solution of Partial Differential Equations: Finite Difference Methods. Oxford University Press, 1985.

[67]   J.N. Reddy and D.K. Gartling. The Finite Element Method in Heat Transfer and Fluid Dynamics. CRC Press, 2000.

[68]   D.V. Hutton. Fundamentals of Finite Element Analysis. McGraw-Hill, 2004.

[69]   E.B. Becker, G.F. Carey and J.T. Oden. Finite Elements, an Introduction. Prentice Hall, 1981.

[70]   C.A. Brebbia, T. Futagami and M. Tanaka. Boundary Elements. Proceedings of the 5-th International Conference, Hiroshima, Japan, 1983.

[71]   A.A. Becker. The Boundary Element Method in Engineering. McCraw-Hill, 1992.

[72]   www.ansys.com

[73]   www.femlab.com

[74]   A. Mandelis, S.B. Peralta and J. Thoen. Photoacoustic Frequency-Domain Depth Profiling of Continuously Inhomogeneous Condensed Phases: Theory and Simulations for the Inverse Problem. Journal of Applied Physics, **70**(3):1761-1770, 1991.

[75]   H.S. Carslaw and J.C. Jaeger. Conduction of Heat in Solids. Oxford University Press, 1959.

[76]   R.C. Gonzalez and R.E. Woods. Digital Image Processing. Prentice Hall, 2002.

[77]   M. Sonka, V. Hlavac and R. Boyle. Image Processing, Analysis, and Machine Vision. PWS Publishing, 1999.

[78]   M. Ghanbari. Standard Codecs: Image Compression to Advanced Video Coding. The Institution of Electrical Engineers, 2003.

[79]   Y.Q. Shi and H. Sun. Image and Video Compression for Multimedia Engineering. CRC Press, 2000.

[80]   S.M. Shepard, J.R. Lhota, B.A. Rubadeux, T. Ahmed and D. Wang. Enhancement and Reconstruction of Thermographic NDT Data. Proceedings of SPIE, **4710**:531-535, 2002.

[81]   D.S. Taubman and M.W. Marcellin. JPEG2000: Image Compression Fundamentals, Standards and Practice. Kluwer Academic Publishers, 2002.

[82] www.ni.com

[83] www.corel.com

[84] www.divx.com

[85] M. Nelson and J. Gailly. The Data Compression Book. M&T Books, 1995.

[86] K. Sayood. Introduction to Data Compression. Academic Press, 2000.

[87] D. Salomon. Data Compression: The Complete Reference. Springer, 1998.

[88] www.winzip.com

[89] www.winrar.com

[90] J. Mackerle. FEM and BEM Parallel Processing: Theory and Applications – a Bibliography. Engineering Computations, **20**:436-484, 2003.

[91] B.H. Topping and A.I. Khan. Parallel Finite Element Computations. Saxe-Coburg Publications, 1996.

Other consulted references

R. Steinberger. Photothermal Surface Crack Detection. PhD Thesis, University of Leoben (Austria), 2002.

C.I. Castanedo. Quantitative Subsurface Defect Evaluation by Pulsed Phase Thermography: Depth Retrieval with the Phase. PhD Thesis, Laval University (Canada), 2005.

Author's publications

S. Lugin and U. Netzelmann. A Defect Shape Reconstruction Algorithm for Pulsed Thermography. NDT&E International, **40**:220-228, 2007.

S. Lugin and U. Netzelmann. Effective Compression Algorithms for Pulsed Thermography. Quantitative Infrared Thermography (QIRT), **3**(2):201-217, 2006.

S. Lugin and U. Netzelmann. Effective Compression Algorithms for Pulsed Thermography. Proceedings of 5-th International Workshop "Advances in Signal Processing for Non-Destructive Evaluation of Materials", Canada, Quebec, 2005.